

Blind Source Separation Methods for Analysis and Fusion of Multimodal Brain Imaging Data

by

Sreenath Pruthvi Kyathanahally

A thesis submitted to the Graduate Faculty of
Auburn University
in partial fulfillment of the
requirements for the Degree of
Master of Science

Auburn, Alabama
August 3, 2013

Keywords: *Simultaneous EEG-fMRI, Dog, ICA, Seed based analysis, Deconvolution*

Copyright 2013 by Sreenath Pruthvi Kyathanahally

Approved by

Gopikrishna Deshpande, Chair, Assistant Professor, Electrical & Computer Engineering
Thomas S Denney, Director, Auburn University MRI Research Center
Jennifer L Robinson, Assistant Professor, Department of Psychology

Abstract

With the advent of functional magnetic resonance imaging (fMRI), several studies have emerged to decipher the functioning of the brain. However, three major issues limit the inferences that one could obtain from the brain using fMRI. First, fMRI time series at each voxel in the brain can be modeled as a convolution of the hemodynamic response function (HRF) and latent neuronal signals representing neural activity. Consequently, it is not a direct measure of neural activity. In the first chapter, we performed blind deconvolution of the HRF to recover latent neuronal signals to demonstrate that important resting state networks (RSNs) in the brain such as the default mode network (DMN) have a neural origin. Second, fMRI is a 4-dimensional multivariate signal which is a complex mixture of unknown independent source signals. In both second and third chapters, we used independent component analysis (ICA) based blind source separation techniques for identifying RSNs in humans and dogs, respectively. Third, fMRI has low temporal resolution which limits our ability to make inferences about fast neuronal processes. Therefore, in the fourth and fifth chapters, we performed multimodal electroencephalography (EEG)-fMRI imaging such that the superior temporal resolution of EEG can be fused with the superior spatial resolution of fMRI so as to obtain high spatio-temporal resolution. Specifically, in the third chapter, we used joint ICA, which assumes a single mixing matrix for both modalities, to investigate decision-making in the brain. In the fourth chapter, we used parallel ICA, which assumes different but correlated

mixing matrices for the two modalities, to demonstrate that the neural basis of the DMN exists in sub-second neural fluctuations, making RSNs more relevant to the time-scale of neural activity. Importantly, unlike previous studies, our fusion ICA approaches do not downsample or sacrifice the native resolution of either modality.

Acknowledgments

I would never have been able to finish my Thesis without the guidance of my committee members and help from my friends.

I would like to express my deepest gratitude to my advisor and mentor, Dr. Gopikrishna Deshpande, who directed me to this research with enormous guidance, support and resources throughout the Master's program. He taught me how to be a researcher and believed in me when I doubted myself. He spent endless hours proofreading my papers and giving me excellent suggestions. I will be always indebted to Dr. Deshpande for encouraging me to present our research papers in conferences which gave me an opportunity to meet researchers all around the world.

I would like to thank Dr. Thomas Denney and Dr. Jennifer Robison who graciously agreed to serve on my thesis committee without making me to plead too severely. I take this opportunity to thank my friends at the AU MRI center, especially Hao Jia, who helped me a lot in research, without him it would have been difficult to finish the projects on time and Karthik, who accompanied me in all the courses and conferences. I would like to express my eternal gratitude to my parents for their everlasting love and support.

Table of Contents

Abstract	ii
Acknowledgments.....	iv
List of Tables	vii
List of Figures	viii
Chapter 1.....	1
Introduction.....	1
1.1 Motivation.....	1
1.2 Imaging Modalities	2
1.3 Simultaneous EEG-fMRI.....	6
1.4 Functional connectivity.....	8
1.5 Bibliography	10
Chapter 2.....	12
Investigating the neural basis of the default mode network using blind hemodynamic deconvolution of resting state fMRI data.....	12
Abstract	12
2.1 Introduction.....	13
2.2 Materials and Methods.....	15
2.3 Results.....	21
2.4 Discussion	27
2.5 Bibiliography	27
Chapter 3.....	32
Anterior-Posterior Dissociation of the Default Mode Network in Dogs	32

Abstract	32
3.1 Introduction.....	33
3.2 Methods.....	35
3.3 Results.....	45
3.4 Discussion	53
3.5 Conclusions.....	57
3.6 Bibiliography	57
Chapter 4	64
A realistic framework for investigating decision-making in the brain with high spatio-temporal resolution using simultaneous EEG/fMRI and joint ICA	64
Abstract	64
4.1 Introduction.....	65
4.2 Materials and Methods.....	69
4.3 Results.....	79
4.4 Discussion	87
4.5 Bibiliography	88
Chapter 5	91
Investigation of the neural basis of the default mode network using parallel independent component analysis of simultaneous EEG/fMRI data	91
Abstract	91
5.1 Introduction.....	92
5.2 Materials And Methods.....	94
5.3 Results.....	105
5.4 Discussion	108
5.5 Conclusion	112
5.6 Bibliography	112

List of Tables

Table 1: Cluster-level statistics of FC maps for all data.....	22
Table 2: Showing the R ² statistic and model p-value for all the EEG Channels	80
Table 3: Correlation and it's corresponding p-value between EEG and fMRI mixing matrices for regular EPI, MB2 and MB8 data	108

List of Figures

Figure 1	3
Figure 2	5
Figure 3	7
Figure 4	18
Figure 5	19
Figure 6	23
Figure 7	24
Figure 8	25
Figure 9	26
Figure 10	36
Figure 11	39
Figure 12	39
Figure 13	42
Figure 14	44
Figure 15	46
Figure 16	48
Figure 17	49
Figure 18	50
Figure 19	51

Figure 20	52
Figure 21	53
Figure 22	70
Figure 23	71
Figure 24	74
Figure 25	76
Figure 26	78
Figure 27	82
Figure 28	83
Figure 29	84
Figure 30	86
Figure 31	98
Figure 32	102
Figure 33	104
Figure 34	105

Figure 35	106
Figure 36	107
Figure 37	107

Chapter 1

Introduction

1.1 Motivation

Brain is the little understood organ in the entire body. Recently with the advent of fMRI several studies have emerged to decipher the functioning of the brain. Information of the brain activity can be found by analyzing the fMRI time series. However there are some limitations associated with fMRI, they are 1) The fMRI time series which is used for analyzing the activity of the brain is the neuronal signal that is convolved with the hemodynamic response function (HRF), which is an indirect way of measuring the neural activity [1], 2) fMRI is a 4-dimensional multivariate signal which is a complex mixture of unknown independent source signals, 3) The fMRI time series have low temporal resolution

In order to address these limitations, different techniques have been carried out in this thesis. The first limitation of fMRI is addressed in the chapter 2 using a blind source hemodynamic deconvolution of resting state data to estimate the neural signals from the BOLD-fMRI. The second limitation is addressed in the chapter 3 using independent component analysis to separate the source signals and the third limitation is addressed in chapter 4 and chapter 5, by acquiring the data using a simultaneous EEG-fMRI, which provides complementary measures of neural electrical activity at high temporal resolution and hemodynamics at high spatial resolution [5] [6] [7] [8] and analyzing it using parallel independent component analysis and joint independent component analysis.

1.2 Imaging Modalities

One of the major challenges in science is to study and understand the human brain. Many invasive and non-invasive brain imaging techniques have been developed to study the brain, but non-invasive imaging has several advantages over invasive techniques, so it has witnessed an explosive development during recent decades. There are many ways to study the brain using different non-invasive imaging modalities but each imaging modality has their own limitations. The noninvasive functional brain mapping techniques include Electroencephalography (EEG), Magnetoencephalography (MEG), Functional Magnetic Resonance Imaging (fMRI), Positron Emission Tomography (PET), Single-Photon Emission Computed Tomography (SPECT), and Near-Infrared Spectroscopy (NIRS). PET, SPECT, NIRS, fMRI neuroimaging techniques work on metabolic or hemodynamic principles, whereas EEG and MEG are based on electrophysiological principles and measures the neuronal currents within the brain directly.

1.2.1 EEG

EEG is one of the noninvasive functional brain mapping techniques which involves the recording of the electrical activity (voltage fluctuations) of the brain versus time by placing the electrodes on the scalp. The recorded electrical activity represents the dendritic potentials from the superficial cortical layers. The dendritic potentials are detected when the constantly exchanging ions from the neurons, to maintain resting potential and to propagate action potential, reaches the electrodes on the scalp. The dendritic potential depends on the synchronicity of neurons, and requires many neurons to sum up their activity to be detected by the electrodes on the scalp. Since EEG is directly measured on the scalp the temporal resolution is high very, but the source

localization of EEG is not good as the CSF, skull and scalp smear out the electric potentials recorded by EEG. So, the recorded signal can only be used to estimate the location of the activity.

Ever since the introduction of first human EEG in 1924 [9], EEG has become popular for detecting Epilepsy, sleep disorders and for other clinical usages.

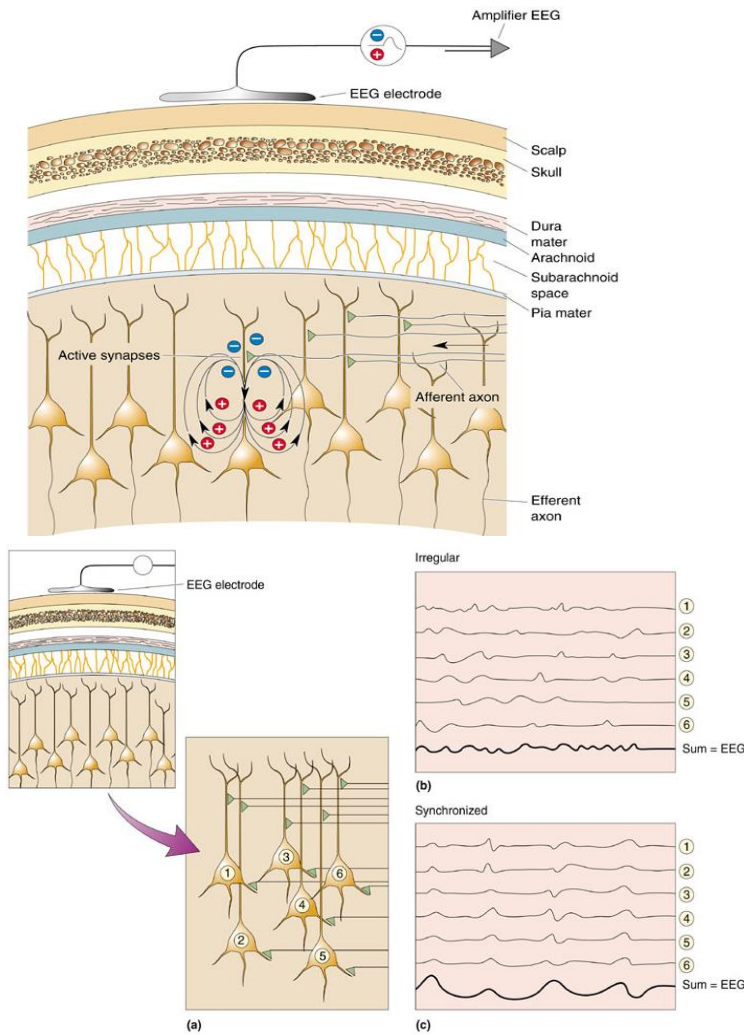


Figure 1: Showing how the electrical signals are generated and propagated (This figure is adapted from cognitrn.psych.indiana.edu/busey/q551/PPTs/week4.ppt

For acquiring the EEG on the scalp, an electrode cap is placed on the scalp of the subject (human) and then a conductive gel (usually saline paste) is put to get good

conduction between scalp and electrode. The electrodes are then connected to amplifiers to amplify the voltage between the electrode and the reference, since the detected signals are usually very small.

1.2.2 MRI

Magnetic Resonance Imaging (MRI) is a noninvasive medical imaging technique which does not use ionizing radiations or radioactive tracers to see the internal structures of the body with the help of high magnetic field and radio wave. The MRI scanner consists of a strong magnet, radio frequency coil and gradient coils. When a person is moved in to the scanner, the randomly spinning hydrogen nuclei inside the body will align in the direction of strong magnetic field and then the three gradient coils are used to select the orientation of the slices in x, y or z direction. Once the gradient coil is chosen, the nuclei at different location will rotate at different speeds since the magnetic field varies spatially along the chosen orientation. Hydrogen nucleus will absorb the energy only when it is in resonance, so when the RF energy is applied at particular frequency (resonant frequency) only the nuclei in the plane that is normal to the orientation of the magnetic field will resonate and thus when the receiver is turned on immediately after the RF pulse, the signal from nuclei lying in the particular plane or slice will be detected, and since none of the hydrogen nuclei located outside the particular plane are excited, it cannot emit the signals and be detected by the receiver. This specific resonant frequency of resonance is called Larmour frequency every tissue has a different Larmour frequency. The Larmour frequency is chosen based on the particular tissue being imaged. In

summary, spatial encoding of each voxel involves the use of strong magnetic field, magnetic field gradient coils and RF pulse in a systematic way.

First the slice is selected using the one of the gradient coils in particular orientation, then the spatial information is encoded along the rows and columns using the other two gradient coils. The MR signal detected at the receiver, written into a data matrix called K-space, is the mixture of RF signals with different amplitudes, frequencies and phases containing spatial information. The center of k-space has low spatial frequency information; this is where most of image information is located. By applying inverse 2D Fourier transform to the k-space the MR image is reconstructed.



Figure 2: MRI Scanner

1.2.3 Functional MRI

MRI can be used to visualize the internal structures of the body, including brain but to visualize the brain activity; fMRI which is a type of MRI is used. fMRI is based on the principle that Cerebral Blood Flow (CBF) and neuronal activation are normally coupled, and increase in metabolic demand due to neuronal activation at certain part of the brain will lead to an increase in flow to that region. This rapid delivery of blood to active neuronal region is called Hemodynamic Response (HDR). Whenever a person is involved

in any task, the brain or neural activity at certain region increases and thus that region demands more energy, which is nothing but demand of more oxygen. The oxygen is carried to neurons by hemoglobin in capillary red blood cells. Thus whenever the neural activity increases the blood flow to that area increases. Since oxygenated hemoglobin is diamagnetic in nature and deoxygenated hemoglobin is paramagnetic in nature, the increase in blood flow at increased neural activity area will be more diamagnetic than the rest of the area. The relative decrease in deoxygenated hemoglobin concentration, which has paramagnetic effect, can be detected by MRI. Thus the difference in the magnetic properties can be associated with the variation of the neural activity in the brain. This type of MR imaging technique where the functional signal corresponding to change in concentration of deoxygenated hemoglobin for the hemodynamic response is considered is known as blood oxygenation level dependent (BOLD) fMRI.

BOLD fMRI is an indirect way of measuring the neuronal activity [1], so there will be always a lag between the neuronal triggering and the hemodynamic response. Thus, fMRI has poor temporal resolution, in seconds but has very high spatial resolution, in millimeter.

1.3 Simultaneous EEG-fMRI

All the modern neuroimaging modalities including EEG and fMRI are based on either electrophysiological or hemodynamic principles. So, no existing neuroimaging modality can have both high spatial and high temporal resolution. Thus, taking the positive aspects of each modalities and combining them is the best solution to study the brain. Combining

imaging modalities will eliminate the negative aspects of each modality when applied separately.

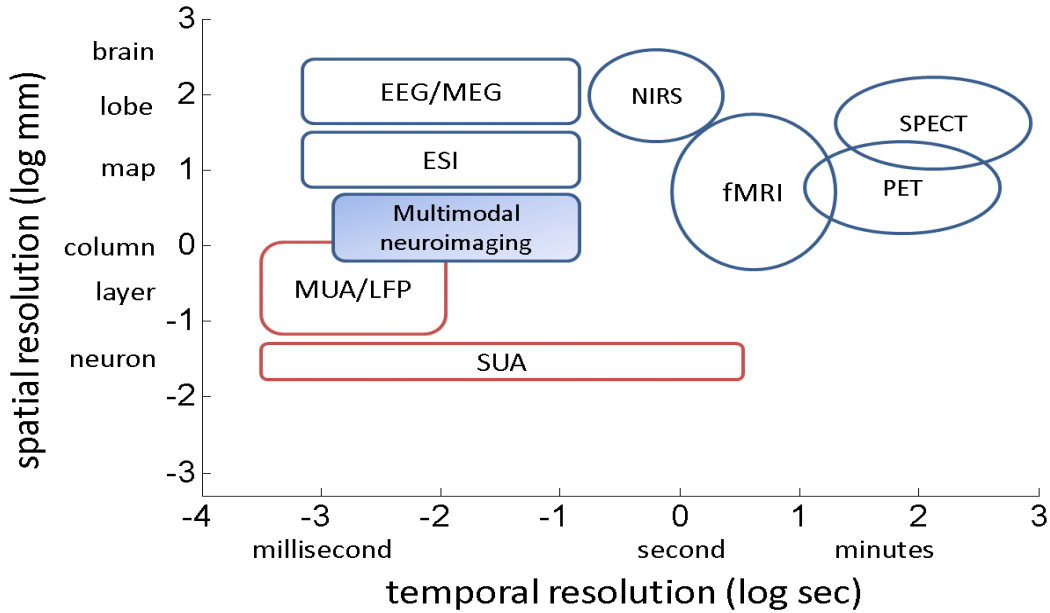


Figure 3: Ranges of spatial and temporal resolution of various noninvasive (in blue) and invasive (in red) imaging/recording techniques. This figure is adapted from (Zhongming Liu, Multimodal Neuroimaging Integrating Functional Magnetic Resonance Imaging and Electroencephalography, 2008)

The above figure shows the ranges of temporal and spatial resolution for all the invasive and non-invasive neuroimaging modalities. Of all the non-invasive neuroimaging techniques, EEG and MEG have the highest temporal resolution and fMRI has the highest spatial resolution. So, combining EEG and fMRI or MEG and fMRI will give both high spatial and high spatial resolution images. Combining MEG and fMRI is not feasible, since MEG has to be recorded only in magnetically shielded rooms. So, the best option is to combine EEG and fMRI.

There are many techniques to combine EEG and fMRI. In this thesis, we apply joint Independent component analysis (jICA) [10, 11] and parallel independent component analysis (pICA) [11] to combine EEG and fMRI. These techniques are discussed in Chapter 4 and Chapter 5.

1.4 Functional connectivity

A large number of anatomically separate brain areas that are temporally correlated and functionally linked and continuously share information to each other are called “functional networks”. Functional connectivity is a method to explore the functional network. Functional connectivity with a particular brain region (Region of interest) can be found by cross correlating the time series of that region with all other voxels in the brain, so that the regions with high temporal correlation with the region of interest (ROI) are displayed and these regions are the functional connections with the ROI. Functional connectivity can be found either by model driven approach or data driven approach. Model driven approach includes seed based correlation analysis and data driven method includes independent component Analysis.

1.4.1 Independent Component Analysis (ICA)

ICA is a type of semi-blind signal separation techniques which assumes the statistical independence of the source signals [12] and decomposes the time series in to statistically independent components that define functional networks. ICA is a data driven method. ICA removes the noise signals, such as physiological or movement-related noise while extracting independent components.

The fMRI signal is assumed to be a linear mixture ($x_1(v), x_2(v), \dots, x_N(v)$), of statistically independent hemodynamic source locations ($s_1(v), s_2(v), \dots, s_N(v)$) such that at a given voxel, it contains the weighted mixture of the sources, $a_{j1}s_1(v) + a_{j2}s_2(v) + \dots + a_{jN}s_N(v)$ and each of which fluctuates according to its weighted hemodynamic time course, for all j . The weights are multiplied by each source's hemodynamic time course. The ideal observed fMRI signal is given by, $x_j(v) = a_{j1}s_1(v) + a_{j2}s_2(v) + \dots + a_{jN}s_N(v)$ If $x = [x_1(v), x_2(v), \dots, x_N(v)]^T$, $s = [s_1(v), s_2(v), \dots, s_N(v)]^T$ and A the mixing matrix with a_{ij} elements, then we can write in vector-matrix notation as $x = As$. x represents the ideal samples of the source signals in the brain at location v . Let us consider that the K discrete time points were acquired with the scanner and these time points are very large compared to actual sources in the brain. The sampled fMRI signal is denoted by $y(v) = y_1(v), y_2(v), \dots, y_N(v)$ where the fMRI is discretely sampled in space. The fMRI data $y(v)$ is pre-whitened to remove any correlations in the data and reduced via Principal Component Analysis (PCA) by removing non-significant components to give out Principal components. These Principal components contain the major proportion of variance. The INFOMAX ICA [13] is then applied to the data to get back the independent components.

1.4.2 Seed Based Correlation Analysis (SCA)

Even though ICA has the advantage of being the data driven method which does not require a priori assumptions, the maps generated with this method are usually more difficult to explain in comparison with those generated with the SCA. SCA is a Model driven method that is a prior knowledge is required on the selected region and about the

experiment. SCA is the correlation measure between one time-series of region of interest called seed and many other time-series (other voxels in the brain), to explore the functional connectivity within the brain. The resultant functional connectivity map will have t-values for each voxel and this map tells how well the other voxels time series correlates with the time series of the seed. Seed based correlation connectivity has become a common method to see which part of the brain exhibit the high level of connectivity with the particular region of interest.

1.5 Bibliography

- [1] N. Logothetis, "What we can do and what we cannot do with fMRI," *Nature*, vol. 453, no. 7197, pp. 869-878, 2008.
- [2] A. Arieli, A. Sterkin, A. Grinvald and A. Aertsen, "Dynamics of ongoing activity: explanation of the large variability in evoked cortical responses," *Science*, vol. 27, no. 273, p. 1868–1871, 1996.
- [3] M. Tsodyks, T. Kenet, A. Grinvald and A. Arieli, "Linking spontaneous activity of single cortical neurons and the underlying functional architecture," *Science*, vol. 3, no. 286, pp. 1943-1946, 1999.
- [4] A. Salek-Haddadi, K. Friston, L. Lemieux and D. Fish, "Studying spontaneous EEG activity with fMRI," *Brain Research*, vol. 43, no. 1, pp. 110-133, 2003.
- [5] S. Debener, M. Ullsperger, M. Siegel and A. Engel, "Single-trial EEGfMRI reveals the dynamics of cognitive function," *Trends Cogn. Sci.*, vol. 10, no. 12, pp. 558-563, 2006.
- [6] J. Hopfinger, W. Khoe and A. Song, "Combining electrophysiology with structural and functional neuroimaging: ERPs, PET, MRI, and fMRI," in *Event Related Potentials. A Methods Handbook*, Cambridge, The MIT Press, 2005, pp. 345-380.
- [7] B. Horwitz and D. Poeppel, "How can EEG/MEG and fMRI/PET data be combined?," *Hum. Brain Mapp.*, vol. 17, no. 1, pp. 1-3, 2002.
- [8] S. Makeig, T. Jung and T. Sejnowski, "Having your voxels and timing them too?," in *Exploratory Analysis and Data Modeling in Functional Neuroimaging edited by F. Sommer and A. Wichert*, Cambridge, The MIT Press, 2002, pp. 195-207.
- [9] L. Haas, "Hans Berger (1873–1941), Richard Caton (1842–1926), and electroencephalography," *Journal of Neurology, Neurosurgery & Psychiatry*, vol. 74, no. 1, p. 9, 2003.
- [10] B. Edwards, V. Calhoun and K. Kiehl, "Joint ICA of ERP and fMRI during error-

- monitoring," *Neuroimage*, vol. 59, no. 2, pp. 1896-1903, 2012.
- [11] V. D. Calhoun, "Fusion ICA Toolbox (FIT)," [Online]. Available: <http://mialab.mrn.org/software/fit/>.
- [12] G. Brown, S. Yamada and T. Sejnowski, "Independent component analysis at the neural cocktail party," *Trends Neurosci.*, vol. 24, no. 1, pp. 54-63, 2001.
- [13] A. Bell and T. Sejnowski, "An information-maximization approach to blind separation and blind deconvolution," *Neural Comput*, vol. 7, no. 6, pp. 1129-1159, 1995.
- [14] S. Ogawa, D. Tank, R. Menon, J. Ellermann, S. Kim, H. Merkle and K. Ugurbil, "Intrinsic signal changes accompanying sensory stimulation: Functional brain mapping with magnetic resonance imaging," *Proceedings of the National Academy of Sciences USA*, vol. 89, no. 13, pp. 5951-5955, 1992.
- [15] S. Ogawa, T. Lee, A. Kay and D. Tank, "Brain magnetic resonance imaging with contrast dependent on blood oxygenation," *Proceedings of the National Academy of Sciences USA*, vol. 87, no. 24, pp. 9868-9872, 1990.
- [16] S. Kim and K. Ugurbil, "Functional magnetic resonance imaging of the human brain," *Journal of Neuroscience Methods*, vol. 74, no. 2, pp. 229-243, 1997.
- [17] P. Fox and M. Raichle, "Focal physiological uncoupling of cerebral blood flow and oxidative metabolism during somatosensory stimulation in human subjects," *Proceedings of the National Academy of Sciences USA*, vol. 83, no. 4, pp. 1140-1144, 1986.

Chapter 2

Investigating the neural basis of the default mode network using blind hemodynamic deconvolution of resting state fMRI data

Abstract

Default mode network (DMN) is one of the most important resting state networks (RSNs) in the brain which has been extensively investigated using functional magnetic resonance imaging (fMRI). However, the neural origin of the DMN is under debate for the following reasons. First, its time scale of the order of 10s of seconds is far removed from the sub-second time scale of neural processes. Second, since fMRI time series at each voxel is the convolution of an underlying neural signal with the hemodynamic response (HRF), there is a debate on whether the DMN is at least in part (or at most fully) a consequence of hemodynamic processes and physiological noise arising due to cardiac pulsation and respiration. In order to investigate this, we performed blind hemodynamic deconvolution of resting state fMRI data that was acquired with different repetition time, spatial resolution and magnetic field strength. Subsequently functional connectivity maps were found using seed based correlation analysis on latent neuronal signals with a posterior cingulate seed in order to identify the DMN. The basic anatomical structure found with deconvolved fMRI data was very similar to that found using fMRI data pre-processed using standard procedure. This provides strong evidence that the DMN has a neural origin and cannot be just a consequence of hemodynamic processes and physiological noise.

2.1 Introduction

Resting State Networks (RSNs) have been studied for more than a decade now and have emerged as one of the most successful approaches in understanding the intrinsic activity of the brain in health and disease. Compared to task based analysis, in resting state fMRI (RS-fMRI), the subjects are not required to perform any task that involves attention; instead they have to just lie still and awake inside the scanner with their eyes closed or open. Specific tasks that involve attention consume less than 5% of the total cerebral metabolism [1], thus showing that the intrinsic activity in the brain is a major source of energy consumption. Many studies have found that spontaneous low frequency fluctuations in anatomically separate regions are correlated, forming different RSNs [2] [3] [4] [5] [6] [7] [8] [9] [10].

Resting state studies are especially useful among clinical population who find it difficult to perform cognitive tasks [11] [12] [13] [14] [15] [16] [17] [18]. Studies have reported disruptions in the RSNs in subjects with neurological or psychiatric diseases [19]. Even though there are several advantages of studying RSNs, there has been a debate whether these RSNs have an unmistakable neural origin or is at least partly (or at most fully) a consequence of hemodynamic processes and/or physiological noise [20] [21] [22] [23] [24]. fMRI time series can be modeled as a convolution of a latent neural signal (which is not measured) and the hemodynamic response function (HRF). First, since the temporal characteristics of the HRF across different anatomical regions can be influenced by the underlying venous structure, it is possible that intrinsic activity across disparate brain regions can be temporally correlated only due to the underlying vascular architecture. Second, the hemodynamic response is affected by physiological fluctuations

arising from cardiac pulsation and respiration [25]. These can introduce temporal correlations into resting state fMRI signals. Also, given the fact that RS-fMRI data is sampled slowly (typically every 1-2 seconds), physiological fluctuations cannot be removed by simple filtering as they can alias into the low frequency band of interest (0.01-0.1 Hz). Third, the period of the fastest variation in RS-fMRI data is 10 s, which is orders of magnitude greater than the sub-second time scale at which most neuronal processes occur. These factors have called the neural basis of RSNs into question even though RSNs, especially the default mode network (DMN), have been shown to be sensitive to various neurological and psychiatric pathologies. Previous studies have found RSNs, including the DMN, even after removing sources of variance in the RS-fMRI signal due to physiological noise using strategies such as RETROICOR [26] and regressing out signals derived from white matter (WM) and cerebrospinal fluid (CSF). However, the networks' neural origin can never be unequivocally established as long as they are derived from hemodynamic signals. Therefore, in this study, we performed blind hemodynamic deconvolution [27] of RS-fMRI data, which was neither band pass filtered nor corrected by some method for removing physiological noise, to recover the underlying latent neuronal signals. The deconvolution is blind because there is no external input in case of RS-fMRI data and consequently, both the HRF and the underlying neuronal latent variables must be simultaneously estimated from the observed fMRI data, making this an ill-posed estimation problem. Since band pass filtering and removing of physiological noise is necessitated by the hemodynamic nature of the RS-fMRI signal, if the HRF itself is removed, then there is no need to perform additional pre-processing. Functional connectivity (FC) maps were found using seed based correlation

analysis (SCA) on both the latent neural signals and RS-fMRI signals obtained by standard pre-processing including bandpass filtering and regressing out of WM and CSF signals. Given that the DMN is one of the RSNs which is robustly seen in the resting state studies [3] and implicated to be sensitive to many brain pathologies [28] [29] [30] [31] [32] [33], we consider only the DMN in this paper, though the results must be applicable to all RSNs. The maps obtained from the latent neural signals and standard RS-fMRI data were compared to see whether the former also showed the temporal correlations between the regions of the DMN that is shown by the latter.

2.2 Materials and Methods

2.2.1 Subjects and Tasks

Subjects with no history of neurological disorders participated in this study, which was approved by the Institutional Review Board at Auburn University. The subjects were instructed to lie supine, stay awake and not think of anything specific inside the scanner with their eyes open or eyes closed. Cushions were placed inside the coil to restrict head movement in the coil. Subjects were also provided with earplugs to avoid any harmful effects from the acoustic noise arising from the scanner.

2.2.2 Data acquisition

3 Tesla

3 T Resting state fMRI data were collected on a 3T Siemens Verio scanner using a

- (1) 32 channel head coil, single-shot gradient-recalled echo planar imaging (EPI) sequence with 29ms TE, 1000ms TR, 90° flip angle, 64 x 64 x 16 acquisition matrix and voxel size of 3.5 x 3.5 x 6.25 mm for fifteen healthy subjects.
- (2) 12 channel head coil, single-shot gradient-recalled echo planar imaging (EPI) sequence with 29ms TE, 1000ms TR, 90° flip angle, 64 x 64 x 16 acquisition matrix and voxel size of 3.5 x 3.5 x 6.75 mm for nine healthy subjects

The data with TR=1000ms were grouped together for analysis (we will refer to this group as 3T1s).

- (3) 12 channel matrix head coil, Multiband EPI (MB-EPI) sequence [34] with 30ms TE, 600ms TR, 55° flip angle, 64 x 64 x 16 acquisition matrix, voxel size of 3.5 x 3.5 x 6.3 mm and multiband factor of 2 for nine healthy subjects. We will refer to this data as 3T.6s

7 Tesla

Resting state fMRI data were collected on a 7T Siemens Magnetom scanner using a 32 channel head coil and

- (1) single-shot gradient-recalled EPI sequence with 41ms TE, 2290ms TR, 70° flip angle, 64 x 64 x 16 acquisition matrix, and 2 x 2 x 3 mm voxel size for four healthy subjects
- (2) single-shot gradient-recalled EPI sequence with 25ms TE, 1000ms TR, 70° flip angle, 64 x 64 x 16 acquisition matrix and voxel size of 3.5 x 3.5 x 6 mm for two healthy subjects
- (3) Multiband EPI sequence with 36ms TE, 2000ms TR, 70° flip angle, 64 x 64 x 16 acquisition matrix and voxel size of 2 x 2 x 3 mm for four healthy subjects

(4) Multiband EPI sequence with 20 ms TE, 1000ms TR, 70° flip angle, 64 x 64 x 16 acquisition matrix and voxel size of 2.2 x 2.2 x 3 mm for twelve healthy subjects

The data with the same repetition time (TR) for the 7 Tesla fMRI data were then grouped together. The data with TR≈2000 ms were grouped together (we will refer to this group as 7T2s) and the data with TR=1000ms were grouped together (we will refer to this group as 7T1s).

2.2.3 Data pre-processing

The 3 T and 7 T fMRI data were preprocessed and analyzed using SPM8 (www.fil.ion.ucl.ac.uk/spm), Data Processing Assistant for Resting-State fMRI ([35] DPARSF, <http://www.restfmri.net>) which is based on SPM toolbox ([36] <http://www.fil.ion.ucl.ac.uk/spm>) and Resting-State fMRI Data Analysis Toolkit ([37] REST, <http://www.restfmri.net>).

The whole data was divided into two categories based on the preprocessing steps and called “rest-raw” and “rest-filtered”. The preprocessing steps for the rest-raw (Figure 4) included slice timing correction, motion correction (realignment), normalization (to MNI template), and detrending. The preprocessing steps for the rest-filtered (Figure 5) included slice timing correction, motion correction (realignment), normalization (to MNI template), detrending, bandpass filtering in the range 0.01-0.1 Hz and removal of nuisance covariates such as white matter and CSF signals. All the data were resampled to 2 x 2 x 2 mm voxels during normalization to MNI template.

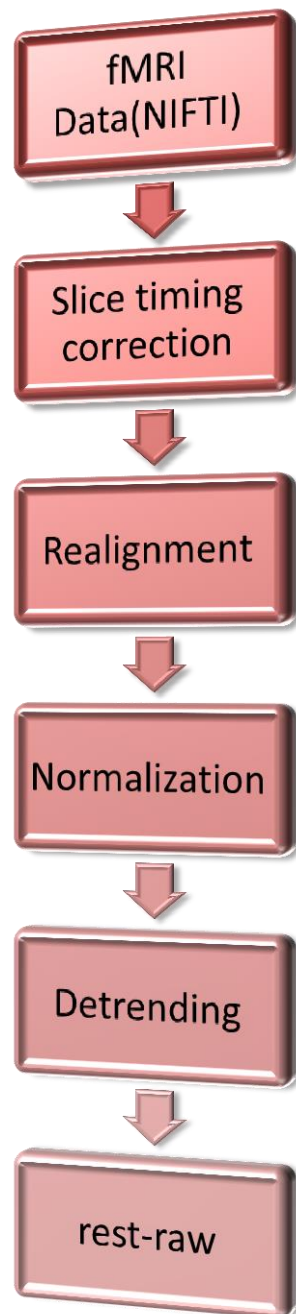


Figure 4: A schematic illustrating fMRI pre-processing for rest-raw data

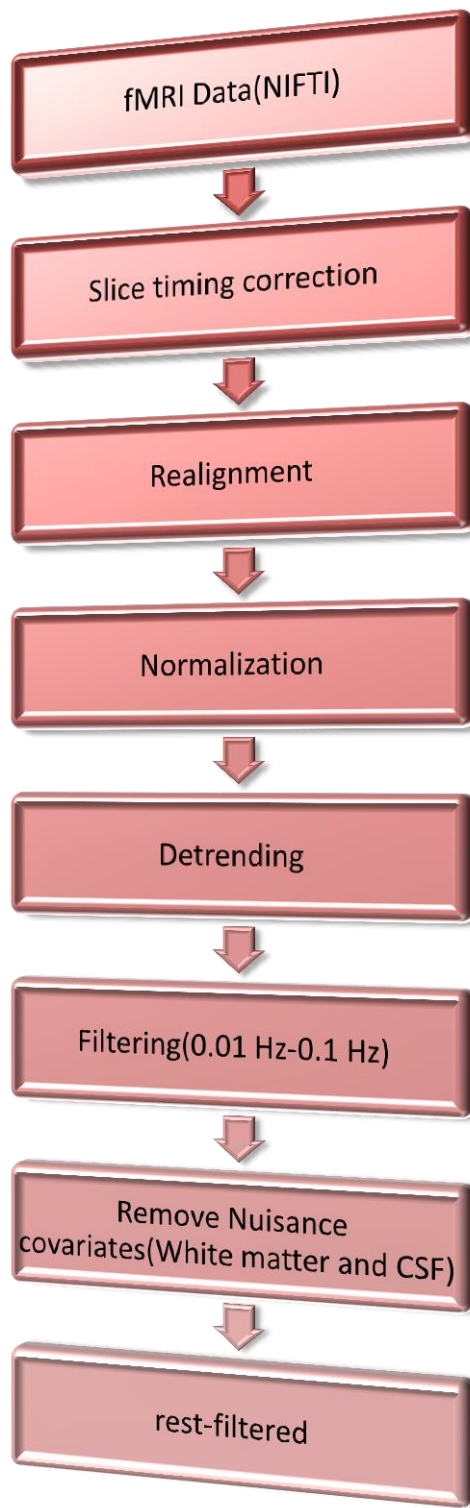


Figure 5: A schematic illustrating fMRI pre-processing for rest-filtered data

2.2.4 Deconvolution for rest-raw data

Blind hemodynamic deconvolution of resting state data was applied to the rest-raw data to remove the HRF from the fMRI data so as to obtain underlying latent neural signals. The observed BOLD fMRI is the result of convolution between the HRF and latent signals representing neural activity. By deconvolving the HRF, we get the neural states but here both the HRF and neural states are unknown and have to be estimated, so it is called “blind” deconvolution. The blind hemodynamic deconvolution of resting state data was performed using the approach proposed by Wu et al [27]. Here they considered the resting fMRI sing as spontaneous event-related data and extracted voxel specific HRFs by individuating the point processes corresponding to signal fluctuations with a given signature and aligning them before applying deconvolution.

2.2.5 Seed based correlation analysis

Seed-based Correlation Analysis (SCA) is one of the methods to get functional connectivity maps wherein Pearson’s correlation is used to determine the similarity between the time series of each voxel in the brain with the times series from a region of interest (ROI), or seed [2]. The resultant functional connectivity map is the map of brain regions that are significantly correlated with the chosen seed/ROI. The correlation values, and the corresponding t-values and p-values, for each voxel in the map tell how well the given voxel time series correlates with the seed time series.

In order to study how the DMN varies across different fMRI data types, a seed at the posterior cingulate cortex (PCC), which is a part of DMN, was chosen at location (-6,-50, 36) mm with 10 mm radius in MNI space [38]. SCA was applied to deconvolved rest-raw

data and rest-filtered data to get FC maps. The correlation (r) values in the FC map were then transformed to z values by Fisher's z transformation [35]. The resultant z value maps were subjected to a one-sample t-test to get the group FC t-map. The group functional connectivity maps were thresholded at $|z|>2.5$ [39] [40] (which corresponds to $p<0.01$) to show only the significant voxels.

2.3 Results

The functional connectivity maps for the rest-raw deconvolved and rest-filtered data of 3T1s, 3T.6s, 7T1s and 7T2s were obtained. The functional connectivity maps obtained from deconvolved rest-raw and rest-filtered data were overlaid on an anatomical image and are shown in the following figures. The rest-raw deconvolved FC map is shown in red and the rest-filtered FC map is shown in green. The overlap between the two is shown in yellow. For all the different fMRI acquisition sequences, the DMN can be seen for both deconvolved data and fMRI data subjected to standard pre-processing. The rest-raw deconvolved and rest-filtered functional connectivity map for 7T2s data with TR= ~2000ms thresholded at $|z|>2.5$ was overlaid on the anatomical image (Figure 6, The number of voxels activated, for 7T2s rest-raw deconvolved data, 7T2s rest-filtered data and the overlap between them is shown in Table 2.1. The rest-raw deconvolved and rest-filtered functional connectivity map 7T1s with TR= 1000ms thresholded at $|z|>2.5$ was overlaid on the anatomical image (Figure 7,). The number of voxels activated, for 7T1s rest-raw deconvolved data, 7T1s rest-filtered data and the overlap between them is shown in Table 1. The rest-raw deconvolved and rest-filtered functional connectivity map for 3T.6s data thresholded at $|z|>2.5$ was overlaid on the anatomical image (Figure

8). The number of voxels activated, for 3T.6s rest-raw deconvolved data, 3T.6s rest-filtered data and the overlap between them is shown in Table 2.1. The rest-raw deconvolved and rest-filtered functional connectivity map for 3T1s data thresholded at $|z|>2.5$ was overlaid on the anatomical image (Figure 9). The number of voxels activated, for 3T1s rest-raw deconvolved data, 3T1s rest-filtered data and the overlap between them is shown in Table 2.1.

Table 1: Cluster-level statistics of FC maps for all data

	No. of significant voxels in 7T2s data	No. of significant voxels in 7T1s data	No. of significant voxels in 3T1s data	No. of significant voxels in 3T.6s data
Rest-raw deconvolved	2667	2170	10352	5982
Rest-filtered	2000	2179	8433	4402
Overlap	1688	1642	6567	3627

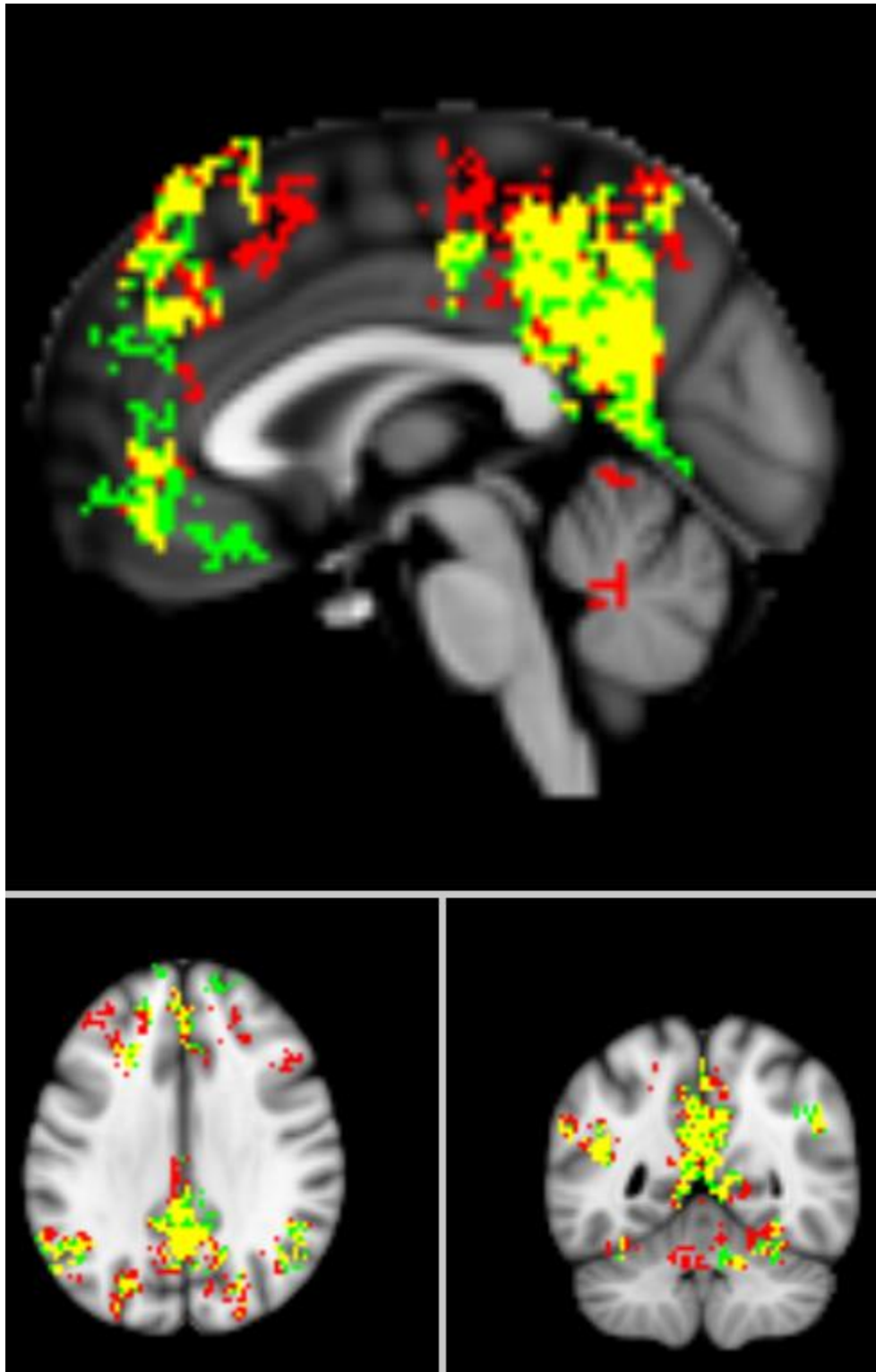


Figure 6: The rest-raw deconvolved and rest-filtered functional connectivity map for 7T2s (TR= ~2000ms) is overlaid on the anatomical image. The rest-raw deconvolved functional connectivity map is shown in RED, the rest-filtered functional connectivity map is shown in GREEN. The common areas between two is shown in YELLOW.

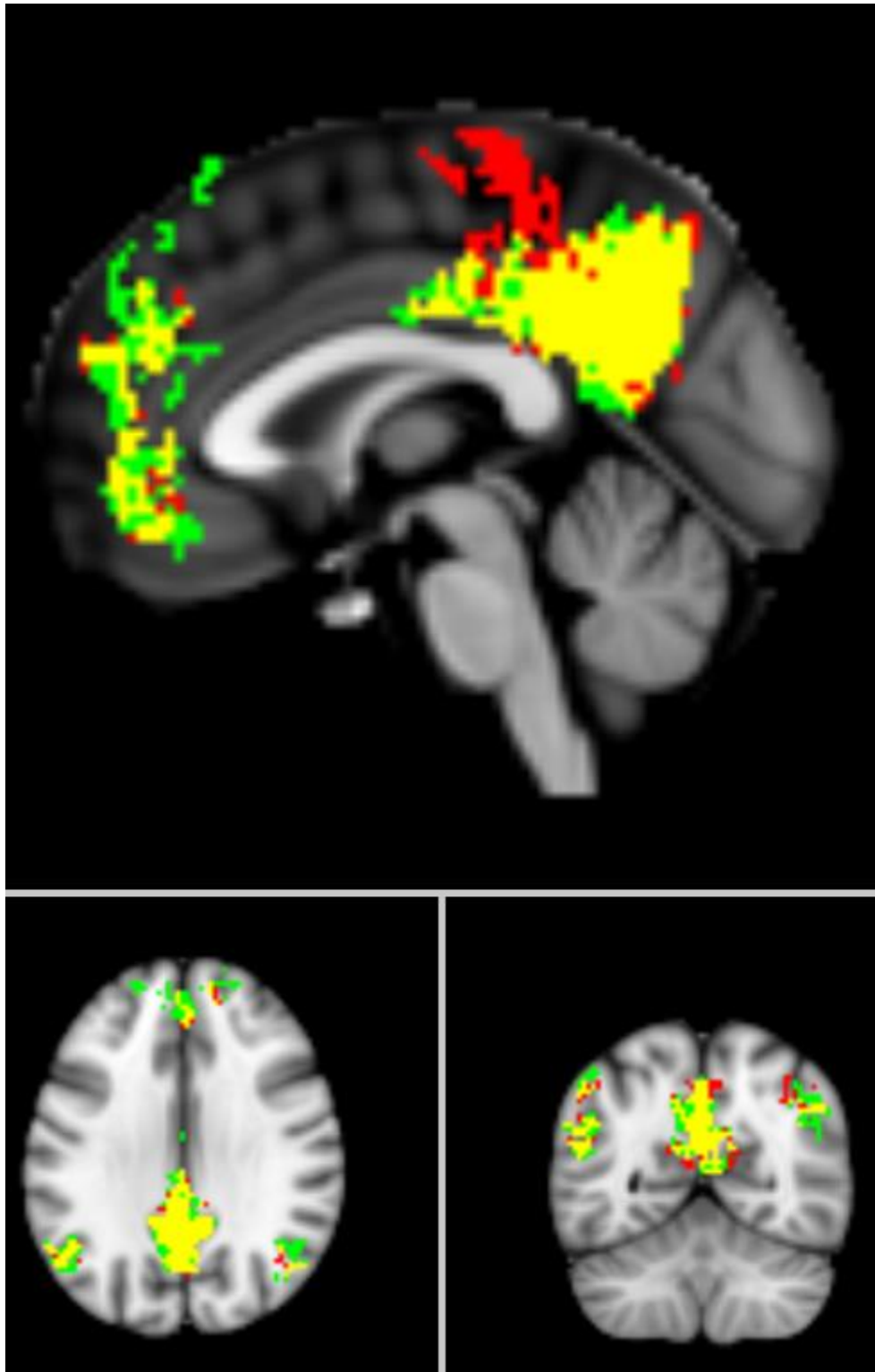


Figure 7: The rest-raw deconvolved and rest-filtered functional connectivity map for rest-filtered 7T1s($TR=1000ms$) is overlaid on the anatomical image. The rest-raw deconvolved functional connectivity map is shown in RED, the rest-filtered functional connectivity map is shown in GREEN. The common areas between two is shown in YELLOW.

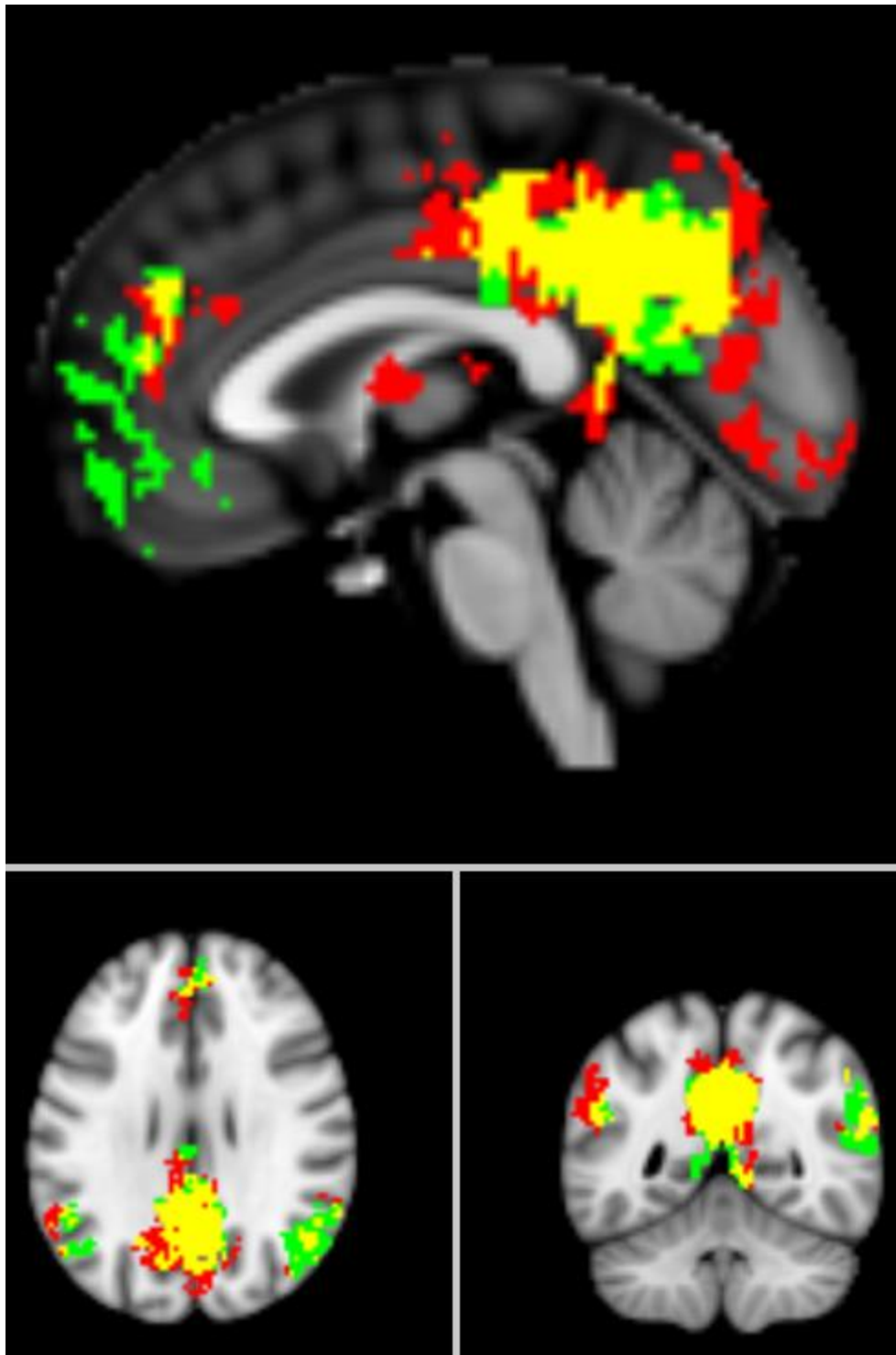


Figure 8: The rest-raw deconvolved and rest-filtered functional connectivity map for 3T1s data (TR=1000ms) is overlaid on the anatomical image. The rest-raw deconvolved functional connectivity map is shown in RED, the rest-filtered functional connectivity map is shown in GREEN. The common areas between two is shown in YELLOW.

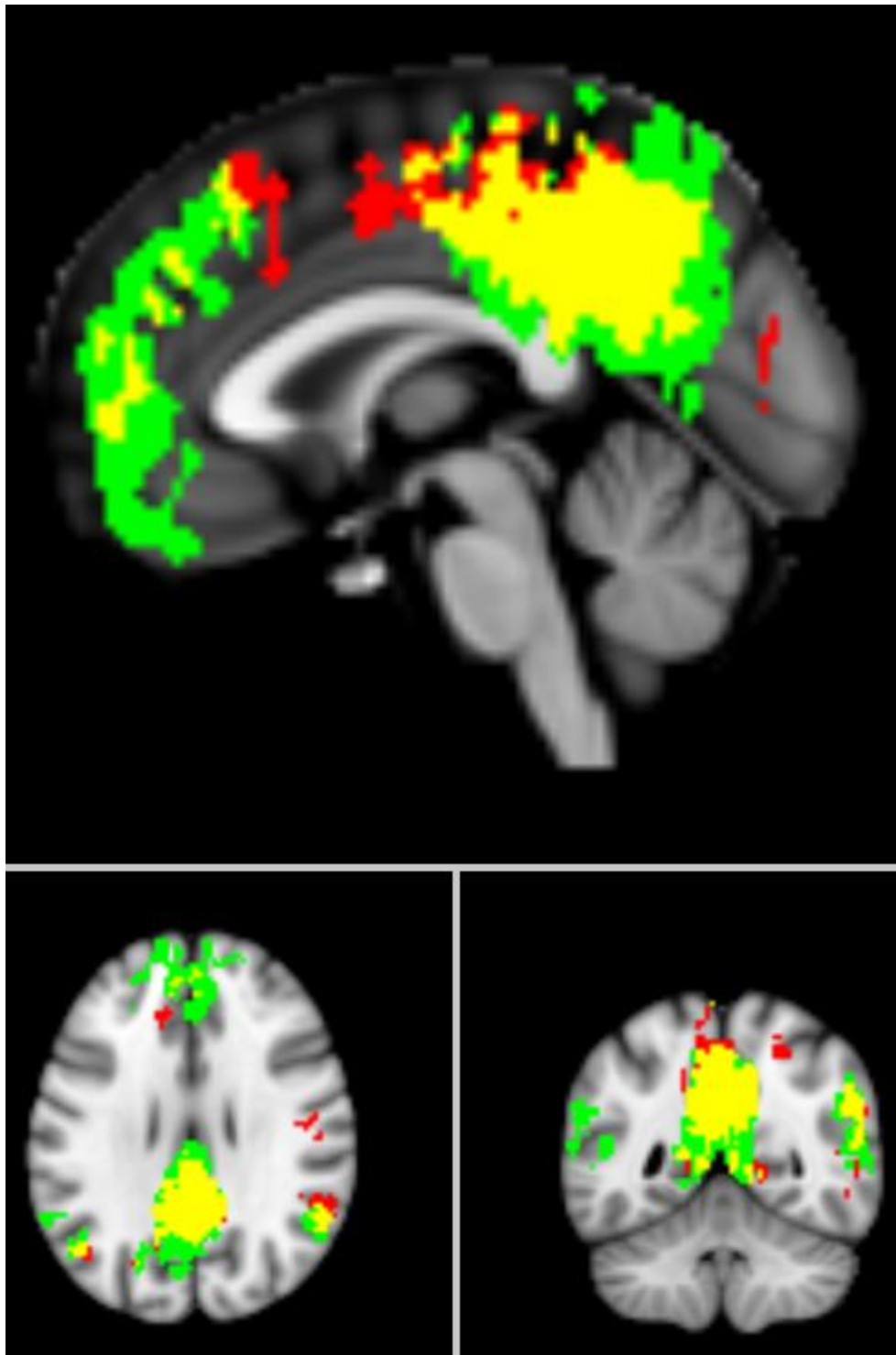


Figure 9: The rest-raw deconvolved and rest-filtered functional connectivity map for 3T.6sdata (TR=600ms) is overlaid on the anatomical image. The rest-raw deconvolved functional connectivity map is shown in RED; the rest-filtered functional connectivity map is shown in GREEN. The common areas between two is shown in YELLOW.

2.4 Discussion

DMN gets activated when the brain is not involved in the external tasks [3] [41] [42] and its connectivity pattern is studied with high interest due to its significance [43] [3] [4] [5]. Many studies have found that the DMN is involved in self-referential processing, and disruption in the connectivity pattern of the DMN may be associated with many neurological brain disorders such as Alzheimer disease [15] and schizophrenia [41] [44]. Therefore, it is very important to investigate whether the DMN has an unequivocal neural origin or is at least in part (or at most fully) a consequence of hemodynamics or physiological noise as some previous studies have suggested [20] [21] [22] [23] [24].

In order to answer the above question, we deconvolved resting state fMRI data that was acquired from 3 Tesla and 7 Tesla scanners with different acquisition sequences and parameters and obtained the DMN using seed-based correlation analysis. We found that the basic anatomical structure of the DMN was evident in functional connectivity maps obtained from both deconvolved rest-raw and rest-filtered data. Since deconvolved rest-raw data essentially represents latent neural signals underlying resting state fMRI fluctuations, we can conclude that the DMN must have an unmistakable neural origin and cannot be result of hemodynamic processes or physiological noise.

2.5 Bibliography

- [1] M. E. Raichle and M. A. Mintun, "BRAIN WORK AND BRAIN IMAGING," *Annual Review of Neuroscience*, vol. 29, pp. 449-476, 2006.
- [2] B. Biswal, F. Yetkin, V. Haughton and J. Hyde, "Functional connectivity in the motor cortex of resting human brain using echo-planar MRI," *Magn. Reson. Med.*, vol. 34, p. 537–541, 1995.

- [3] M. Fox and M. Raichle, "Spontaneous fluctuations in brain activity observed with functional magnetic resonance imaging," *Nat. Rev. Neurosci.*, vol. 8, p. 700–711, 2007.
- [4] M. D. Greicius, B. Krasnow, A. L. Reiss and V. Menon, "Functional connectivity in the resting brain: A network analysis of the default mode hypothesis," *Proceedings of the National Academy of Sciences of the United States of America*, vol. 100, pp. 253-258, 2003.
- [5] D. Gusnard, M. Raichle and M. Raichle, "Searching for a baseline: Functional imaging and the resting human brain," *Nat Rev Neurosci*, vol. 2, p. 685–694, 2001.
- [6] C. Beckmann, M. DeLuca, J. Devlin and S. Smith, "Investigations into resting-state connectivity using independent component analysis," *Philos Trans R Soc Lond B Biol Sci*, vol. 360, pp. 1001-1013, 2005.
- [7] J. Damoiseaux, S. Rombouts, F. Barkhof, P. Scheltens and C. Stam, "Consistent resting-state networks across healthy subjects," *Proc Natl Acad Sci U S A*, vol. 103, pp. 13848-13853, 2006.
- [8] M. Van den Heuvel, R. Mandl and P. H. Hulshoff, "Normalized group clustering of resting-state fMRI data," *PLoS ONE*, vol. 3, no. 4, 2008.
- [9] M. Van den Heuvel, R. Mandl, J. Luigjes and P. H. Hulshoff, "Microstructural Organization of the Cingulum Tract and the level of Default Mode Functional Connectivity," *The Journal of Neuroscience*, vol. 28, no. 43, pp. 10844-10851, 2008.
- [10] D. Cordes, V. Haughton, K. Arfanakis, G. Wendt and P. Turski, "Mapping functionally related regions of brain with functional connectivity," *AJNR Am J Neuroradiol*, vol. 21, no. 9, pp. 1636-1644, 2000.
- [11] D. Auer , "Spontaneous low-frequency blood oxygenation level-dependent fluctuations and functional connectivity analysis of the 'resting' brain," *Magn Reson Imaging*, vol. 26, no. 7, 2008.
- [12] A. Bokde, P. Lopez-Bayo, T. Meindl, S. Pechler, C. Born, F. Faltraco, S. Teipel, H. Moller and H. Hampel, "Functional connectivity of the fusiform gyrus during a face-matching task in subjects with mild cognitive impairment," *Brain*, vol. 129, p. 1113–1124, 2006.
- [13] F. Castellanos, D. Margulies, A. Kelly, L. Uddin, M. Ghaffari, A. Kirsch, D. Shaw, Z. Shehzad, A. Di Martino, B. Biswal, E. Sonuga-Barke, J. Rotrosen, L. Adler and M. Milham, "Cingulate-precuneus interactions: a new locus of dysfunction in adult attention-deficit/hyperactivity disorder," *Biol. Psychiatry*, vol. 63, p. 332–337, 2008.
- [14] M. Greicius, B. Flores, V. Menon, G. Glover, H. Solvason, H. Kenna, A. Reiss and A. Schatzberg, "Resting-state functional connectivity in major depression: abnormally increased contributions from subgenual cingulate cortex and thalamus," *Biol. Psychiatry*, vol. 62, pp. 429-437, 2007.
- [15] M. Greicius, G. Srivastava, A. Reiss and V. Menon, "Default-mode network activity distinguishes Alzheimer's disease from healthy aging: evidence from functional MRI," *Proc. Natl. Acad. Sci. U. S. A*, vol. 101, p. 4637–4642, 2004.
- [16] S. Rombouts and P. Scheltens, "Functional connectivity in elderly controls and AD patients using resting state fMRI: a pilot study," *Curr. Alzheimer Res*, vol. 2, pp.

115-116, 2005.

- [17] L. Tian, T. Jiang, Y. Wang, Y. Zang, Y. He, M. Liang, M. Sui, Q. Cao, S. Hu, M. Peng and Y. Zhuo, "Altered resting-state functional connectivity patterns of anterior cingulate cortex in adolescents with attention deficit hyperactivity disorder," *Neurosci. Lett.*, vol. 400, pp. 39-43, 2006.
- [18] H. Whalley, E. Simonotto, I. Marshall, D. Owens, N. Goddard, E. Johnstone and S. Lawrie, "Functional disconnectivity in subjects at high genetic risk of schizophrenia," *Brain*, vol. 128, pp. 2097-2108, 2005.
- [19] A. Fornito and E. Bullmore, "What can spontaneous fluctuations of the blood oxygenation-level-dependent signal tell us about psychiatric disorders?," *Curr. Opin. Psychiatry*, vol. 23, no. 3, pp. 239-249, 2010.
- [20] R. Birn, K. Murphy and P. Bandettini, "The effect of respiration variations on independent component analysis results of resting state functional connectivity," *Hum Brain Mapp.*, vol. 29, no. 7, pp. 740-750, 2008.
- [21] R. Wise, K. Ide, M. Poulin and I. Tracey, "Resting fluctuations in arterial carbon dioxide induce significant low frequency variations in BOLD signal," *Neuroimage.*, vol. 21, no. 4, pp. 1652-1664, 2004.
- [22] A. Morcom and P. Fletcher, "Does the brain have a baseline? Why we should be resisting a rest," *Neuroimage*, vol. 37, no. 4, pp. 1073-1082, 2007.
- [23] T. Lund, "fcMRI--mapping functional connectivity or correlating cardiac-induced noise?," *Magn Reson Med.*, vol. 46, no. 3, pp. 628-629, 2001.
- [24] J. Maldjian, "Functional connectivity MR imaging: fact or artifact?," *AJNR Am J Neuroradiol.*, vol. 22, no. 2, pp. 239-240, 2001.
- [25] D. Cordes, V. Haughton, K. Arfanakis, J. Carew, P. Turski, C. Moritz, M. Quigley and M. Meyerand, "Frequencies contributing to functional connectivity in the cerebral cortex in "resting-state" data," *AJNR Am J Neuroradiol.*, vol. 22, no. 7, pp. 1326-1333, 2001.
- [26] G. Glover, T. Li and D. Ress, "Image-based method for retrospective correction of physiological motion effects in fMRI: RETROICOR," *Magn Reson Med.*, vol. 44, no. 1, pp. 162-167, 2000.
- [27] G. Wu, W. Liao, S. Stramaglia, J. Ding, H. Chen and D. Marinazzo, "A blind deconvolution approach to recover effective connectivity brain networks from resting state fMRI data," *Med Image Anal.*, vol. 17, no. 3, pp. 365-374, 2013.
- [28] R. Buckner, J. Andrews-Hanna and D. Schacter, "The brain's default network: Anatomy, function, and relevance to disease," *Ann N Y Acad Sci*, vol. 1124, pp. 1-38, 2008.
- [29] Y. Zhou, M. Milham, Y. Lui, L. Miles, J. Reaume, D. Sodickson, R. Grossman and Y. Ge, "Default-mode network disruption in mild traumatic brain injury," *Radiology*, vol. 265, no. 3, pp. 882-892, 2012.
- [30] G. Mingoia, W. G, L. K, R. Maitra, S. Smesny, M. Dietzek, H. Burmeister, J. Reichenbach, R. Schlösser, C. Gaser, H. Sauer and I. Nenadic, "Default mode network activity in schizophrenia studied at resting state using probabilistic ICA," *Schizophr Res.*, vol. 138, no. 2-3, pp. 143-149, 2012.

- [31] V. Bonnelle, R. Leech, K. Kinnunen, T. Ham, C. Beckmann, X. De Boissezon, R. Greenwood and D. Sharp, "Default mode network connectivity predicts sustained attention deficits after traumatic brain injury," *J Neurosci.*, vol. 31, no. 38, pp. 13442-13451, 2011.
- [32] K. Mevel, B. Grassiot, G. Chételat, G. Defer, B. Desgranges and F. Eustache, "The default mode network: cognitive role and pathological disturbances," *Rev Neurol (Paris)*, vol. 166, no. 11, pp. 859-872, 2010.
- [33] J. Shin, V. Kepe, G. Small, M. Phelps and J. Barrio, "Multimodal Imaging of Alzheimer Pathophysiology in the Brain's Default Mode Network," *Int J Alzheimers Dis.*, vol. 2011, no. 2011, 2011.
- [34] D. Feinberg, S. Moeller, S. Smith, E. Auerbach, S. Ramanna, M. Gunther, M. Glasser, K. Miller, K. Ugurbil and E. Yacoub, "Multiplexed echo planar imaging for sub-second whole brain fMRI and fast diffusion imaging," *PLoS One*, vol. 5, no. 12, 2010.
- [35] Y. Chao-Gan and Z. Yu-Feng, "DPARSF: A MATLAB Toolbox for "Pipeline" Data Analysis of Resting-State fMRI," *Front Syst Neurosci*, vol. 4, no. 13, 2010.
- [36] K. Friston, A. Holmes, K. Worsley, J. Poline, C. Frith and J. Frackowiak, "Statistical parametric maps in functional imaging: A general linear approach," *Human Brain Mapping*, vol. 2, no. 4, pp. 189-210, 1995.
- [37] X.-W. Song, Z.-Y. Dong, X.-Y. Long, S.-F. Li, X.-N. Zuo, C.-Z. Zhu, Y. He, C.-G. Yan and Y.-F. Zang, "REST: A Toolkit for Resting-State Functional Magnetic Resonance Imaging Data Processing," *PLoS ONE*, vol. 6, no. 9, 2011.
- [38] J. K. Daniels, A. C. McFarlane, R. L. Bluhm, K. A. Moores, C. R. Clark, M. E. Shaw, P. C. Williamson, M. Densmore and R. A. Lanius, "Switching between executive and default mode networks in posttraumatic stress disorder: alterations in functional connectivity," *J Psychiatry Neurosci.*, vol. 35, no. 4, pp. 258-266, 2010.
- [39] M. McKeown, S. Makeig, G. Brown, T. Jung, S. Kindermann, A. Bell and T. Sejnowski, "Analysis of fMRI data by blind separation into independent spatial components," *Hum Brain Mapp.*, vol. 6, no. 3, pp. 160-188, 1998.
- [40] V. Calhoun, T. Adali, G. Pearson, Z. P. van and J. Pekar, "Independent component analysis of fMRI data in the complex domain," *Magn Reson Med.*, vol. 48, no. 1, pp. 180-192, 2002.
- [41] M. Greicius, "Resting-state functional connectivity in neuropsychiatric disorders," *Curr Opin Neurol.*, vol. 21, pp. 424-430, 2008.
- [42] M. Raichle, A. MacLeod, A. Snyder, W. Powers, D. Gusnard and G. Shulman, "A default mode of brain function," *Proc Natl Acad Sci USA*, vol. 98, pp. 676-682, 2001.
- [43] J. Damoiseaux, C. Beckmann, E. Arigita, F. Barkhof, P. Scheltens, C. Stam, S. Smith and S. Rombouts, "Reduced resting-state brain activity in the "default network" in normal aging," *Cereb Cortex*, vol. 18, no. 8, pp. 1856-1864, 2008.
- [44] E. Bullmore and O. Sporns, "Complex brain networks: graph theoretical analysis of structural and functional systems," *Nat Rev Neurosci.*, vol. 10, no. 3, pp. 186-198, 2009.

- [45] D. Margulies, J. Böttger, X. Long, Y. Lv, C. Kelly, A. Schäfer, D. Goldhahn, A. Abbushi, M. Milham, G. Lohmann and A. Villringer, "Resting developments: a review of fMRI post-processing methodologies for spontaneous brain activity," *MAGMA*, Vols. 5-6, pp. 289-307, 2010.
- [46] B. Yeo, F. Krienen, J. Sepulcre, M. Sabuncu, D. Lashkari, M. Hollinshead, J. Roffman, J. Smoller, L. Zöllei, J. Polimeni, B. Fischl, H. Liu and R. Buckner, "The organization of the human cerebral cortex estimated by intrinsic functional connectivity," *J Neurophysiol.* , vol. 106, no. 3, pp. 1125-1165, 2011.
- [47] K. Kalcher, W. Huf, R. Boubela, P. Filzmoser, L. Pezawas, B. Biswal, S. Kasper, E. Moser and C. Windischberger, "Fully exploratory network independent component analysis of the 1000 functional connectomes database," *Front Hum Neurosci.*, vol. 6, no. 301, 2012.
- [48] M. Dagli, J. Ingeholm and J. Haxby, "Localization of cardiac-induced signal change in fMRI," *Neuroimage.* , vol. 9, no. 4, pp. 407-415, 1999.
- [49] C. Windischberger, H. Langenberger, T. Sycha, E. Tscherenko, G. Fuchsänger-Mayerl, L. Schmetterer and E. Moser, "On the origin of respiratory artifacts in BOLD-EPI of the human brain," *Magn Reson Imaging.* , vol. 20, no. 8, pp. 575-582, 2002.

Chapter 3

Anterior-Posterior Dissociation of the Default Mode Network in Dogs

Abstract

The default mode network (DMN) in humans has been extensively studied using seed-based correlation analysis (SCA) and independent component analysis (ICA). While DMN has been observed in monkeys as well, there are conflicting reports on whether they exist in rodents. Dogs are higher mammals than rodents, but cognitively not as advanced as monkeys and humans. Therefore, they are an interesting species in the evolutionary hierarchy for probing the comparative functions of the DMN across species. In this study, we sought to know whether the DMN, and consequently its functions such as consciousness and self-referential processing, are exclusive to humans/monkeys or do we also observe in animals such as dogs. In order to address this issue, resting state functional MRI data from the brains of lightly sedated dogs and unconstrained & fully awake dogs were acquired and ICA and SCA was performed for identifying the DMN. Since anesthesia can alter resting state networks, confirming our results in awake dogs became essential. Awake dog imaging was accomplished by training the dogs to keep their head still using reinforcement behavioral adaptation techniques. We found that the anterior (such as anterior cingulate and medial frontal) and posterior regions (such as posterior cingulate) of the DMN were dissociated in both awake and anesthetized dogs.

3.1 Introduction

Resting state functional magnetic resonance imaging (fMRI) studies have revealed correlated spontaneous low frequency (< 0.1 Hz) blood oxygenation level dependent (BOLD) fluctuations in anatomically distinct regions called “resting state networks” (RSNs) in humans [1] [2] [3] [4] [5] [6] [7] [8] [9]. Resting state studies have gained importance since then it was introduced in 1995 by Biswal and colleagues [1]. In resting state fMRI (RS-fMRI), the subjects have to just lie still and awake inside the scanner with their eyes closed or open and do not require performing any cognitive task. This paradigm is especially useful among clinical population who cannot perform cognitive tasks and also it unburdens the experimental design [10] [11] [12] [13] [14] [15] [16] [17]. Neurological or psychiatric diseases have been shown to be associated with the alterations in the RSNs [18]. Owing to these advantages, RS-fMRI studies are gaining importance.

Default mode network (DMN), consisting of precuneus, medial frontal, inferior parietal cortical regions and medial temporal lobe [19], is one of the RSNs that has been studied with high interest. DMN is robustly seen in the resting state studies [20] [2] [3] [4]. DMN is active during rest and becomes less active during most external tasks that require attention [2] [21] [22]. DMN is linked to the process of human cognition and self-referential processing [21] [4] [23]. Given the role of the DMN in self-referential processing and consciousness, previous studies have investigated the existence of the DMN in many species. This question is of importance to clearly understand the biological and evolutionary role of the DMN. Resting state networks have been shown to exist in humans, monkeys and rodents [24] [25], but there has been no resting state study in dogs.

In rodents, resting networks have been observed. However, with respect to the DMN, some studies have not found one [25] [26] [27], while others have found either a DMN [28] or a DMN-like network [29]. Dogs are higher mammals than rodents, but cognitively not as advanced as monkeys and humans. Therefore, they are an interesting species in the evolutionary hierarchy for probing the biological and evolutionary role of the DMN. In this study, we sought to know whether DMN and its functions, such as consciousness and self-referential processing, are exclusive in humans/monkey or do we also observe in animals such as dogs. In order to address this issue, resting state functional MRI data from the brains of anesthetized dogs and awake dogs were acquired and analyzed using seed based correlation analysis and data driven Independent Component Analysis (ICA).

Generally, performing fMRI on animals requires them to be anesthetized so that head movement artifacts can be minimized. However, there are studies which show that network connectivity decreases with the increase in anesthesia level [30] [31][32] and these raise questions on the reliability of the networks found in anesthetized animals. Therefore, we performed functional MR imaging using awake, unconstrained and fully conscious dogs as well. This was achieved using behavioral training of dogs using positive reinforcement learning so that they keep their head still while scanning [33] [34] .

Resting state studies carried out using seed based analysis need *a priori* definition of a seed region in the brain which can bias results [2]. On the other hand, ICA_does not need *a priori* information of seed regions [5]; however, they are handicapped by other assumptions such as the number of components in the model [35]. There are also studies

which says that both ICA and seed based method yields the same result [36] [37] [38] [39]. Therefore, we first applied ICA on resting state fMRI data obtained from both anesthetized and awake dogs, and to cross verify those results, we also applied the seed based correlation analysis with a seed placed at posterior cingulate. For determining the consistent and most reproducible independent components across dogs we applied the generalized Ranking and Averaging Independent Component Analysis by Reproducibility (gRAICAR) algorithm [40] which gives the components that are consistent and reproducible. Our results indicate that the anterior and posterior parts of the DMN are dissociated in dogs.

3.2 Methods

All methods and experiments were approved by the Auburn University Institutional Animal Care and Use Committee. The experiment was comprised of 96 runs of anesthetized dog imaging and 74 runs of awake dog imaging. They were collected in six Labrador retriever dogs that were recruited from the Auburn University Canine Detection Research Institute with ages in the range of 12 to 60 months. A human knee coil was used as a head coil for imaging the dog's brain. For anesthetized dog imaging, dogs were sedated and lightly anesthetized with intramuscularly administered xylazine (2.2 mg/kg) and ketamine HCL (11mg/kg,) respectively whereas for awake dog imaging, the dogs were trained by the means of positive reinforcement behavior shaping procedures to go inside the scanner to the required position, insert their heads inside a human knee coil, and remain motionless for the duration required for imaging (Figure 10)

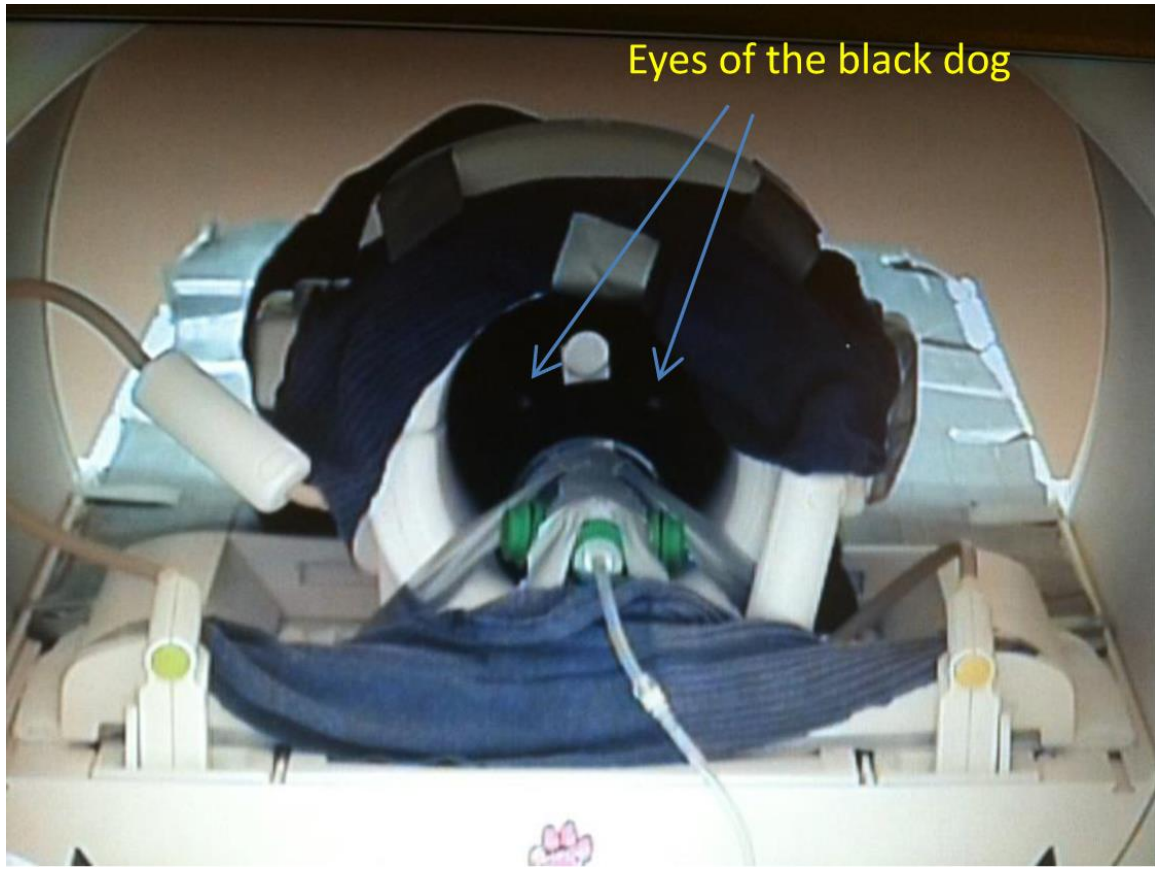


Figure 10: Awake dog positioned inside the scanner and inserted its head inside the human knee coil. This figure is adapted from [34].

3.2.1 Data Acquisition

MR imaging was performed on a Siemens 3 Tesla Verio scanner. Structural images were acquired using magnetization-prepared rapid gradient echo (MPRAGE) [41] three-dimensional T1-weighted sequence (TR=1550 ms, TE=2.64 ms, voxel size: $0.792 \times 0.792 \times 1 \text{ mm}^3$, FA=9°, in-plane matrix 192×192 , number of slices: 104). 200 T_2^* -weighted functional images were acquired using a single-shot gradient-recalled echo-planar imaging [42] (EPI) sequence sensitive to BOLD contrast (repetition time (TR)=1000 ms, echo time (TE)=29 ms, field of view (FOV)= 192×192 mm, flip angle (FA)=90 degree, in-plane resolution 3×3 mm, in-plane matrix of 64×64).

3.2.2 Pre-Processing

The Pre-processing was carried out using SPM, DPARSF, and REST toolboxes and the dog brain mask was created using Brain Suite toolbox. [43, 44, 45, 46].

3.2.3 Slice timing correction

While acquiring the fMRI data, instead of all slices being collected at once at each TR, it is collected at different time instants during the length of TR. In order to correct for this slice acquisition delays between individual slices temporal data interpolation was performed using the `spm_slice_timing.m` function as implemented in SPM8 [43] such that the slices appear to have been collected at the same time.

3.2.4 Realignment

Movement during scanning may affect the quality of the data by causing spurious changes in the signal intensity over the scans and it also causes the brain images to become misaligned. Therefore, we applied volume realignment which is an alignment in spatial domain and is performed by calculating 6 motion parameters (three translations and three rotations) based on a rigid-body model of the head and brain [47] in the least square sense. We set the first image as a reference image and resliced it to make the images in time match voxel-by-voxel. A 4th order B-spline interpolation was used for reslicing.

3.2.5 Spatial Normalization

Spatial normalization is used to convert the brain images of different head sizes acquired from different subjects to a standard template such that analyzing the subjects as a group becomes feasible [48]. Standard templates such as EPI-MNI template for humans and monkeys are derived from hundreds of subjects whereas a recently reported standard template for dogs [49] is derived from less than 10 dogs. Since the dogs brain sizes vary a lot according to the dog breed, we cannot use the existing template which does not capture the entire spectrum of head size variability. Therefore, we adopted a two-step approach for the spatial normalization such that there is a proper co-registration across the dogs' functional images after spatial normalization. A flow chart illustrating steps 1 and 2 of our proposed spatial normalization procedure is shown in Figures 11 and 12, respectively. This two-step approach is based on the simple assumption that the co-registration between the functional and anatomical images from the same session have higher accuracy and co-registration across subjects from the same imaging modality is more reliable. In first step, we chose a high quality anatomical image from one of the anesthetized dog runs (since anesthetized dogs absolutely do not move, their anatomical images are of superior quality compared to those obtained from awake dogs) and then chose a functional image from the same session. This functional image was normalized to the chosen anatomical image (Fig.3.2). In the second step (Fig.3.3), the functional images from the all the other sessions were warped onto the space of the the normalized functional image obtained from the first step.. The normalized images, were then bounded in a bounding box so as to remove the parts outside.

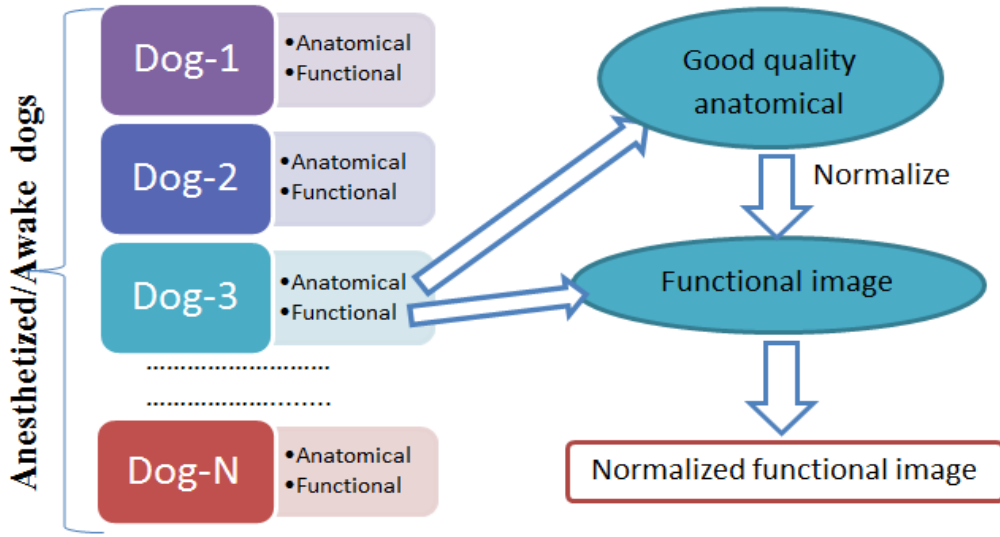


Figure 11: Step 1 of the proposed spatial normalization procedure.

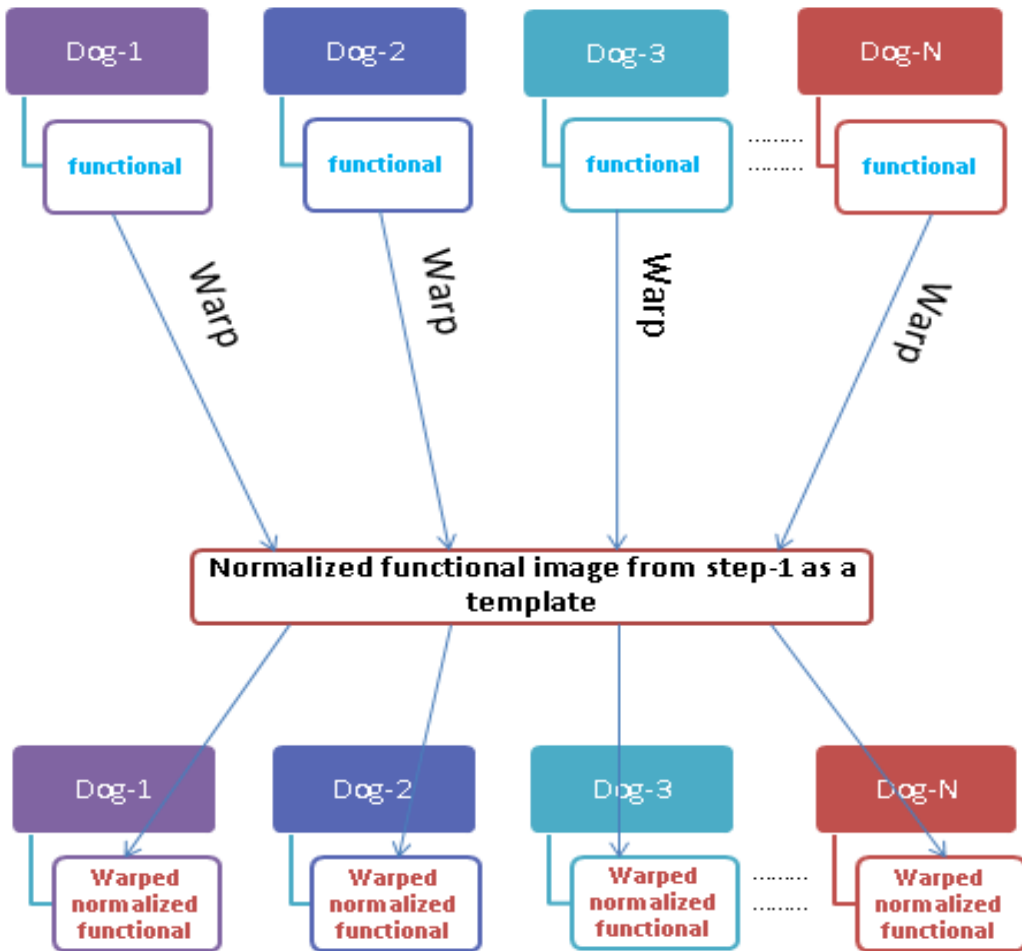


Figure 12: Step 2 of the proposed spatial normalization procedure.

3.2.6 Spatial Smoothing

The bounded normalized functional images were spatially smoothed by removing high-frequency information with a Gaussian filter with 4mm full width half max to increase the signal-to-noise ratio of an image. Smoothing with a Gaussian kernel also transforms the signal distribution in the image and thus helping to meet the statistical assumptions underlying fMRI analysis.

3.2.7 Detrending, Filtering and Brain Mask

Detrending is a mathematical operation which is used to remove the linear trend from the fMRI data. Previous studies using RS-fMRI have shown that low frequency fluctuations (0.01 Hz to 0.1 Hz) display the strongest temporal correlations and are most likely to be free from other physiological and measurement-related artifacts [50]. Therefore, we band pass filtered the fMRI data in the range 0.01 Hz - 0.1 Hz. The above two operations were performed using DPARSF toolbox [44] . A full brain binary mask was then created in Brain Suite [46].

3.2.8 Regress out nuisance covariates

The six head motion parameters and the global mean signal contribute to the variance in resting state fMRI fluctuations which are likely of non-neural origin and are considered as nuisance effects. Therefore, they were regressed out of the fMRI voxel time series.

3.2.9 Independent Component Analysis (ICA)

ICA is a blind source separation technique which assumes statistical independence of the source signals [51]. Spatial ICA was carried out using INFOMAX algorithm [52] as implemented in GIFT toolbox [53] [54] on pre-processed fMRI data. The pre-processing steps included slice-timing correction, realignment, spatial normalization, smoothing, detrending and filtering (Figure 13). Regression of the global mean signal was not performed because physiological noise and other nuisance variables appear as independent components after ICA analysis and can be discarded then. The number of independent components from ICA was estimated using the Minimum Description Length (MDL) criterion for each individual subject. For checking the reproducibility across the subjects for the components estimated from MDL criteria for each subject, we adopted gRAICAR algorithm [40]. The gRAICAR algorithm is a very efficient algorithm which estimates the reproducible components across the subjects. 39 components were found to be reproducible for anesthetized dogs and 42 components were found to be reproducible for awake dogs.

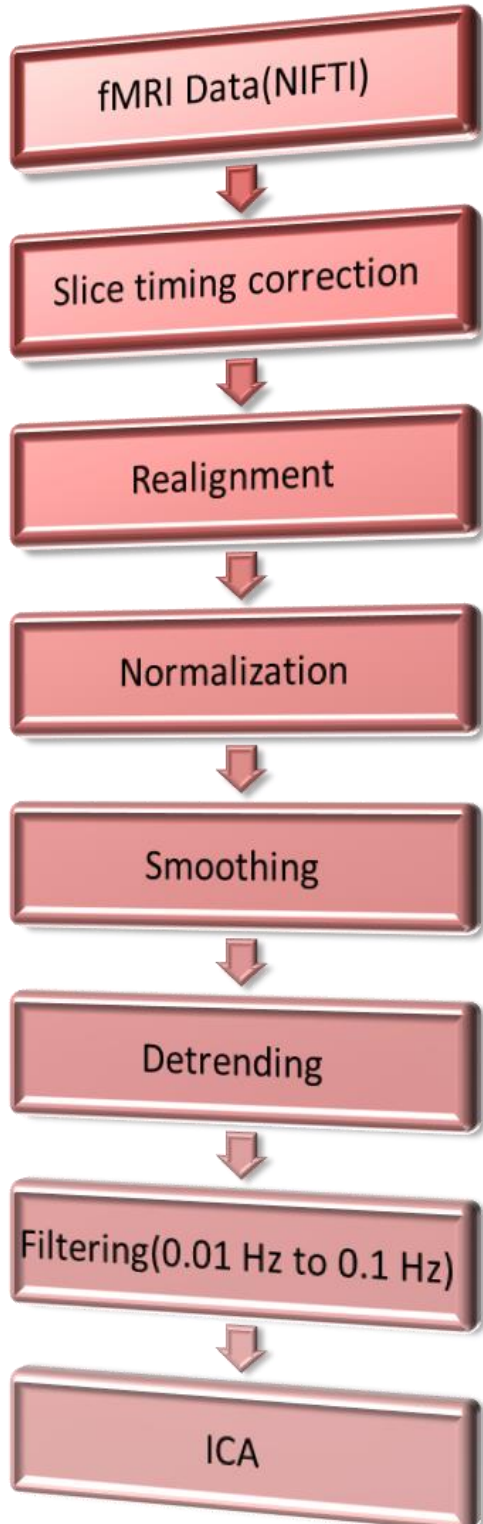


Figure 13: fMRI preprocessing steps before performing ICA

3.2.10 Seed Based Analysis

Even though ICA has the advantage of being a data driven method which does not require *a priori* assumptions, the spatially independent components generated with this method are usually more difficult to explain in comparison with those generated with seed based correlation analysis because experience is required to determine whether a given spatial source is of neuronal origin or an artifact. Seed-based correlation obtained by calculating the Pearson's correlation measure between one time-series from a region of interest called the "seed" and all other voxel time series in the brain in a pairwise fashion. The resultant functional connectivity map will have t-values for each voxel and this map tells us how well the other voxels time series covaries with the time series of the seed. For our analysis, we chose the seed at (0,-41,-10) location with a sphere of 4 mm radius in MNI space for pre-processed fMRI data obtained from anesthetized and awake dogs. The pre-processing steps were slice-timing correction, realignment, normalization, smoothing, detrending, filtering and global mean signal removal (Figure 14). The functional connectivity maps were populated into a sample and a one-sample t-test was performed to get the group level seed-based connectivity map.

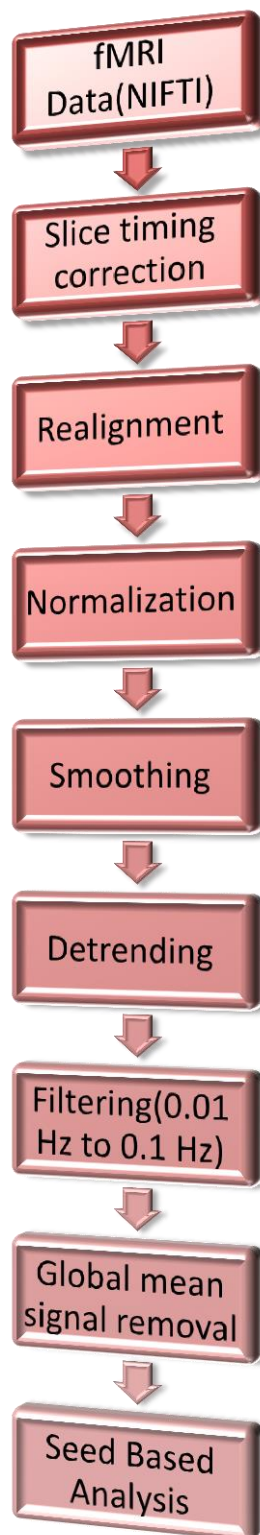


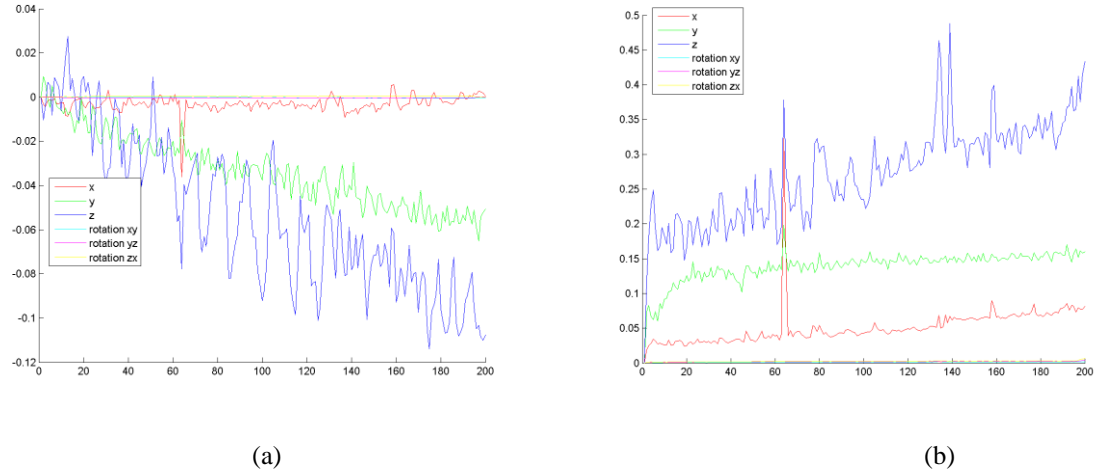
Figure 14: fMRI preprocessing steps before performing seed based correlation analysis

3.3 Results

3.3.1 Realignment

Mean and standard deviation time series of 6 affine parameters for anesthetized dogs and awake dogs were plotted to check whether there is significant head movement in the awake and anesthetized dogs. There was not much head movement in the awake dogs but the motion for anesthetized dogs was significantly smaller as expected and this is evident from the following figures. The Figures 15(a) and 15(b) show mean and standard deviation time series of affine parameters for anesthetized dogs, respectively, while Figures 15(e) and 15(f) show mean and standard deviation time series for awake dogs, respectively.

Figures 15(c) and 15(d) show affine parameters for the worst and best performing dogs, respectively, under anesthesia. Likewise, Figures 15(g) and 15(h) show affine parameters for the worst and best performing awake dogs, respectively.



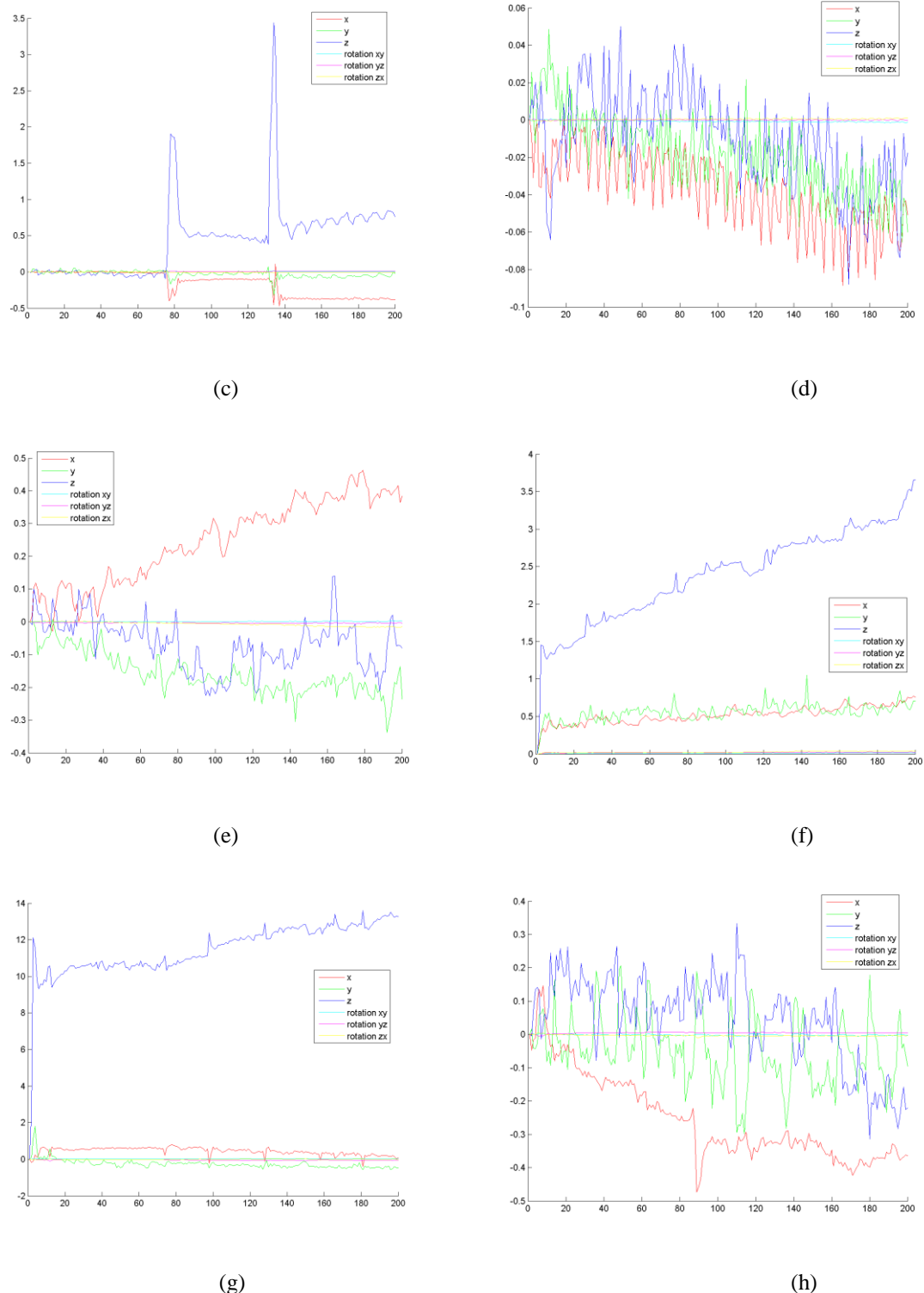
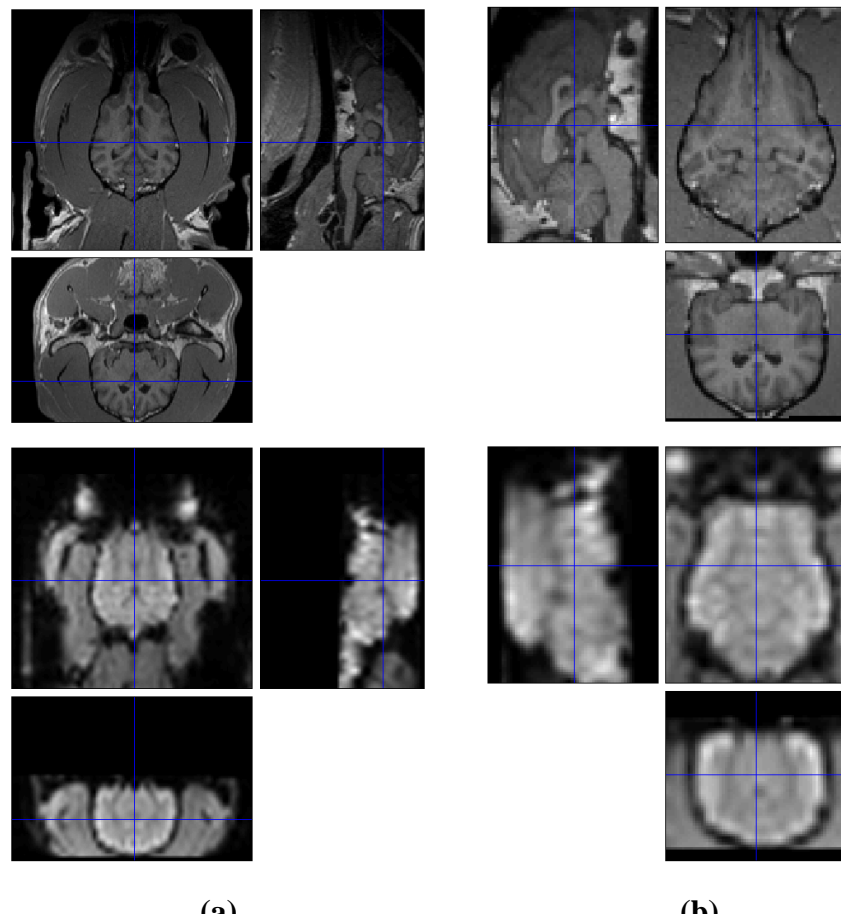


Figure 15: Six motion parameters calculated relative to the first functional slice by realignment procedure. (a) mean time series of 6 affine parameters for anesthetized dogs; (b) standard deviation time series of 6 affine parameters for anesthetized dogs; (c) sample time series of 6 affine parameters for the worst behaved dog at anesthetized state ;(d) sample time series of 6 affine parameters for the best behaved dog at anesthetized state; (e) mean time series of 6 affine parameters for awake dogs;(f) standard deviation time

series of 6 affine parameters for awake dogs;(g) sample time series of 6 affine parameters for the worst behaved dog at awake state;(h) sample time series of 6 affine parameters for the best behaved dog at awake state.

3.3.2 Spatial Normalization

The proposed two step approach for the spatial normalization gave very good co-registration between the dogs' functional images. This is required for carrying out group functional connectivity analysis. Figures 16a and 16b illustrate the first step in the proposed spatial normalization procedure were in a good quality structural image was chosen and then the functional image from the same session as of structural image was normalized to it. Figure 17 illustrates the second step of the proposed spatial normalization procedure. It can be seen that before the second step of normalization, co-registration between the functional images from different dogs was poor (Figure 17a), whereas very good co-registration can be observed after the second step (Figure 17b). Once the spatial normalization was done, a bounding box was imposed to the final structural and functional images, so as to show up only the region of interest (Figure 16b and Figure 17c).



(a)

(b)

Figure 16: Result from the first step of the proposed spatial normalization procedure (a) the functional image is normalized to the anatomical image, both from the same session. (b) The images are bounded so as to show only the brain part.

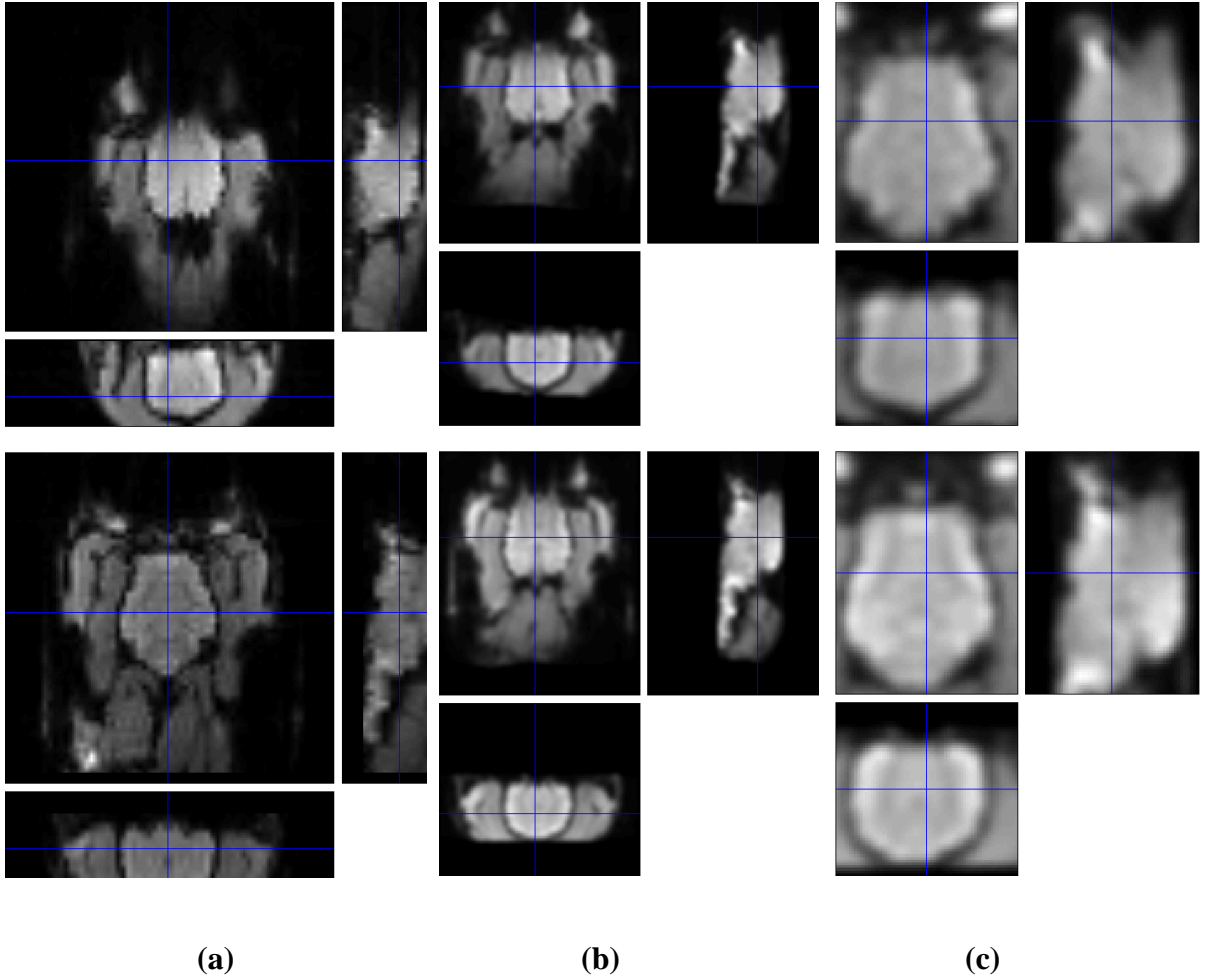


Figure 17: Second step of the proposed spatial normalization procedure (a) Co-registration between the functional image of one dog and functional image of another dog before the 2nd step of spatial normalization (b) Co-registration between the functional image of one dog and functional image of another dog after 2nd step of spatial normalization (c) Co-registration between the bounded functional image of one dog to bounded functional image of another dog after 2nd step of spatial normalization

3.3.3 Independent Component Analysis

Figures 18 and 19 show the independent components thresholded at $|Z|>2.5$ for anesthetized and awake dogs. The color of the activation map indicates the magnitude of the activity, with higher being shown in yellow and lower in red. The results indicate that for both awake and anesthetized dogs, the anterior cingulate/medial prefrontal area and

posterior cingulate, which are parts of DMN and shown as one component in humans, were dissociated and appeared in different components.

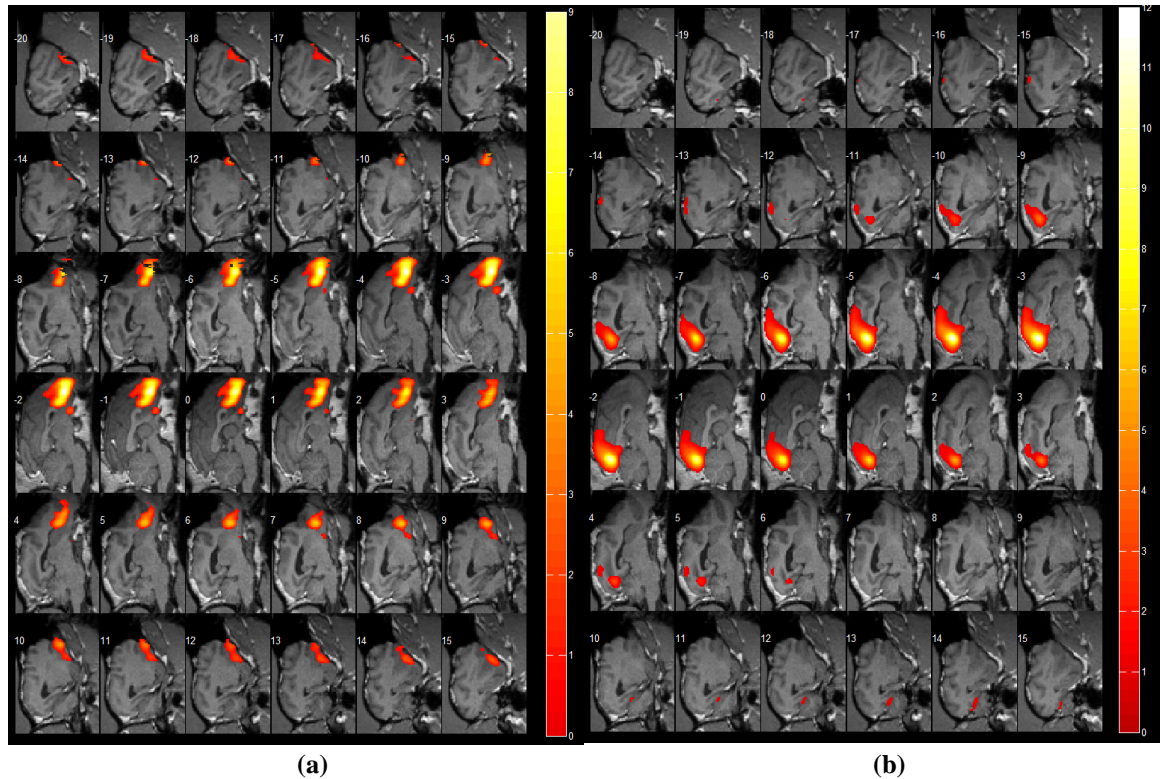


Figure 18: Separate ICA components showing anterior (a) and posterior (b) regions of the DMN for anesthetized dogs ($|z|>2.5$). Note that the anterior (a) and posterior (b) regions were dissociated as they appear in different components

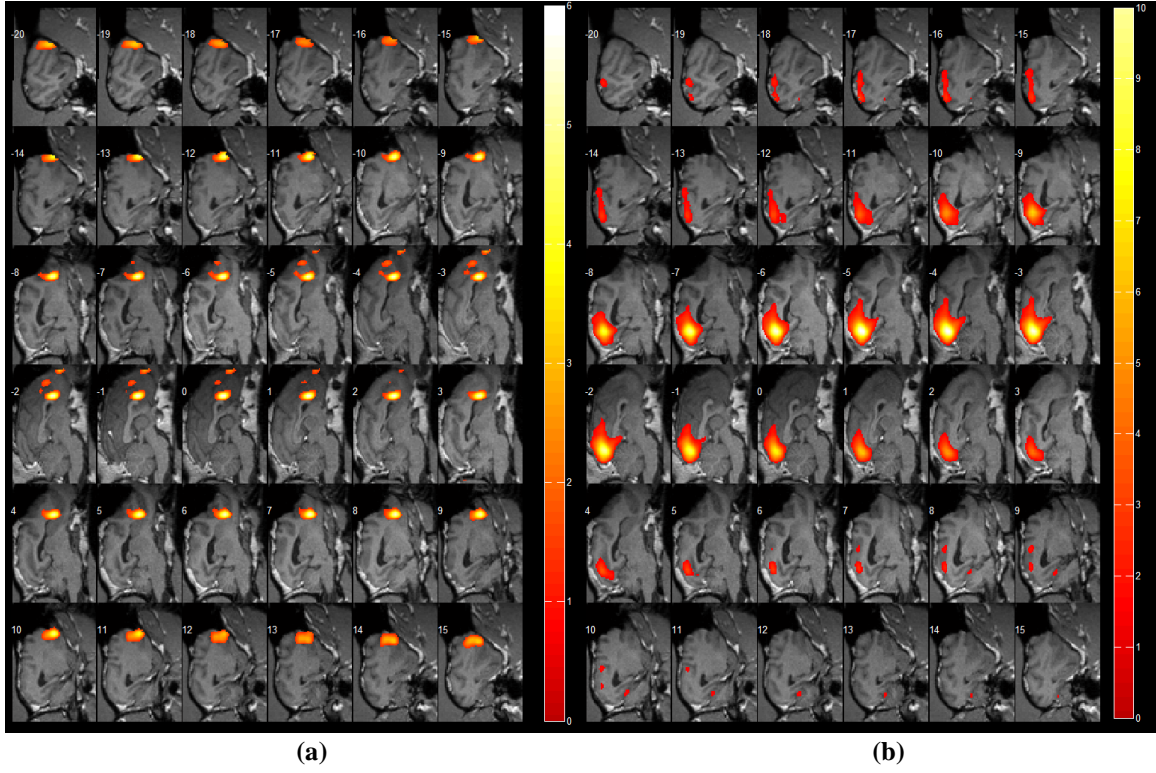


Figure 19: Separate ICA components showing anterior (a) and posterior (b) regions of the DMN for awake dogs ($|z|>2.5$). Note that the anterior (a) and posterior (b) regions were dissociated as they appear in different components

3.3.4 Seed Based Analysis

Figures 20 and 21 show the seed based correlation maps for anesthetized and awake dogs, respectively, with a seed of 4 mm radius in MNI space being placed at (0,-41,-10) location. The color map indicates the t-value and the color of the activation map indicates the magnitude of the activity, with higher being shown in yellow and lower being in red. The within-condition statistical threshold, for anesthetized dog was set at $|t|>4.078$ which corresponds to corrected $P<0.0001$ and the within-condition statistical threshold, for awake dog was set at $/t/>4.11$ which corresponds to corrected $P<0.0001$. The results indicate that for both awake and anesthetized dogs, connectivity was observed only around the seed in posterior parietal areas and there was no connectivity between

posterior cingulate and anterior regions such as medial prefrontal cortex and anterior cingulate.

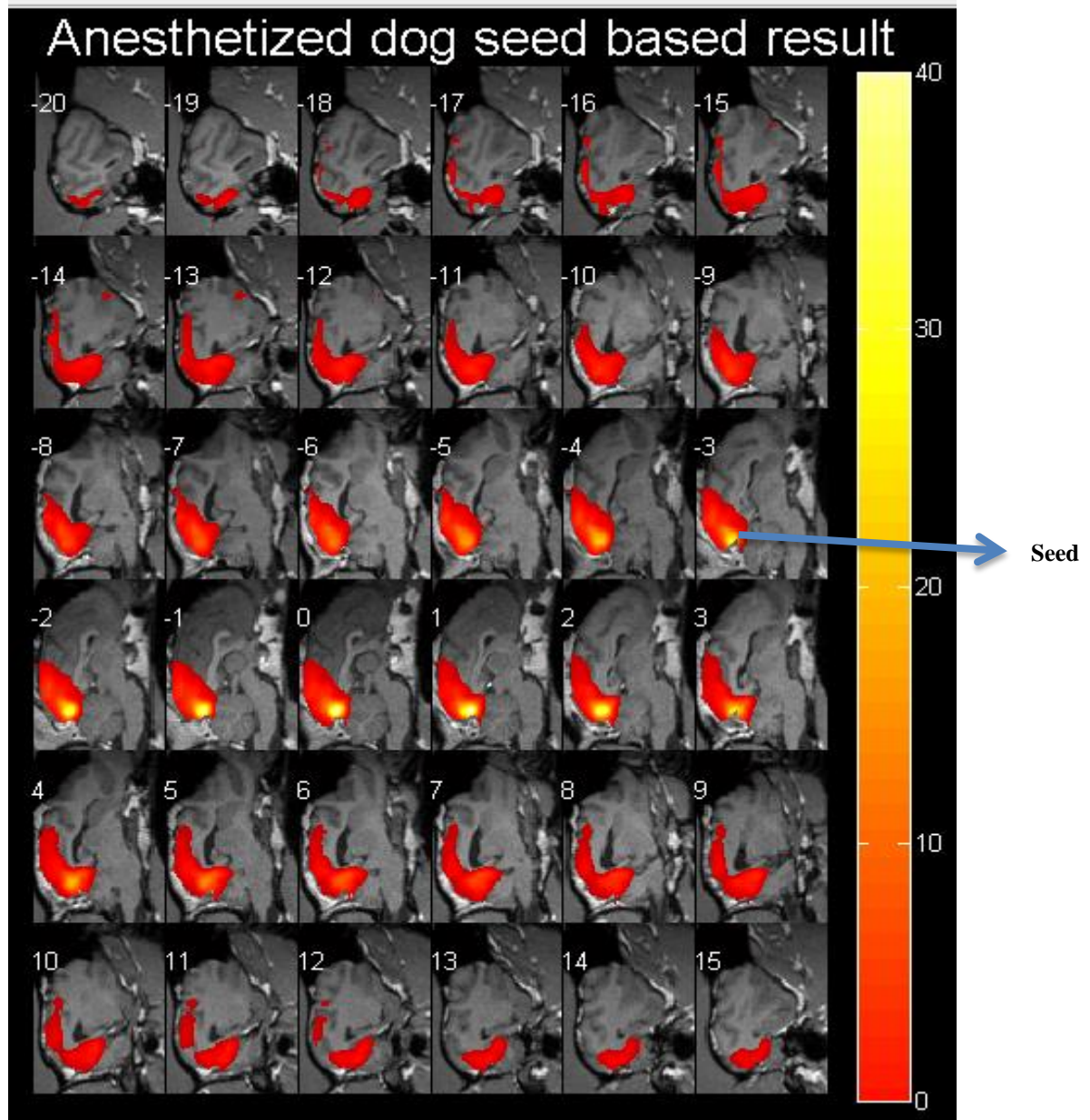


Figure 20: Seed-based connectivity map shows the t-images for the anesthetized dogs. The image was thresholded at corrected- $p<0.0001$ and $|t|>4.078$. The posterior cingulate seed is shown in the figure by an arrow

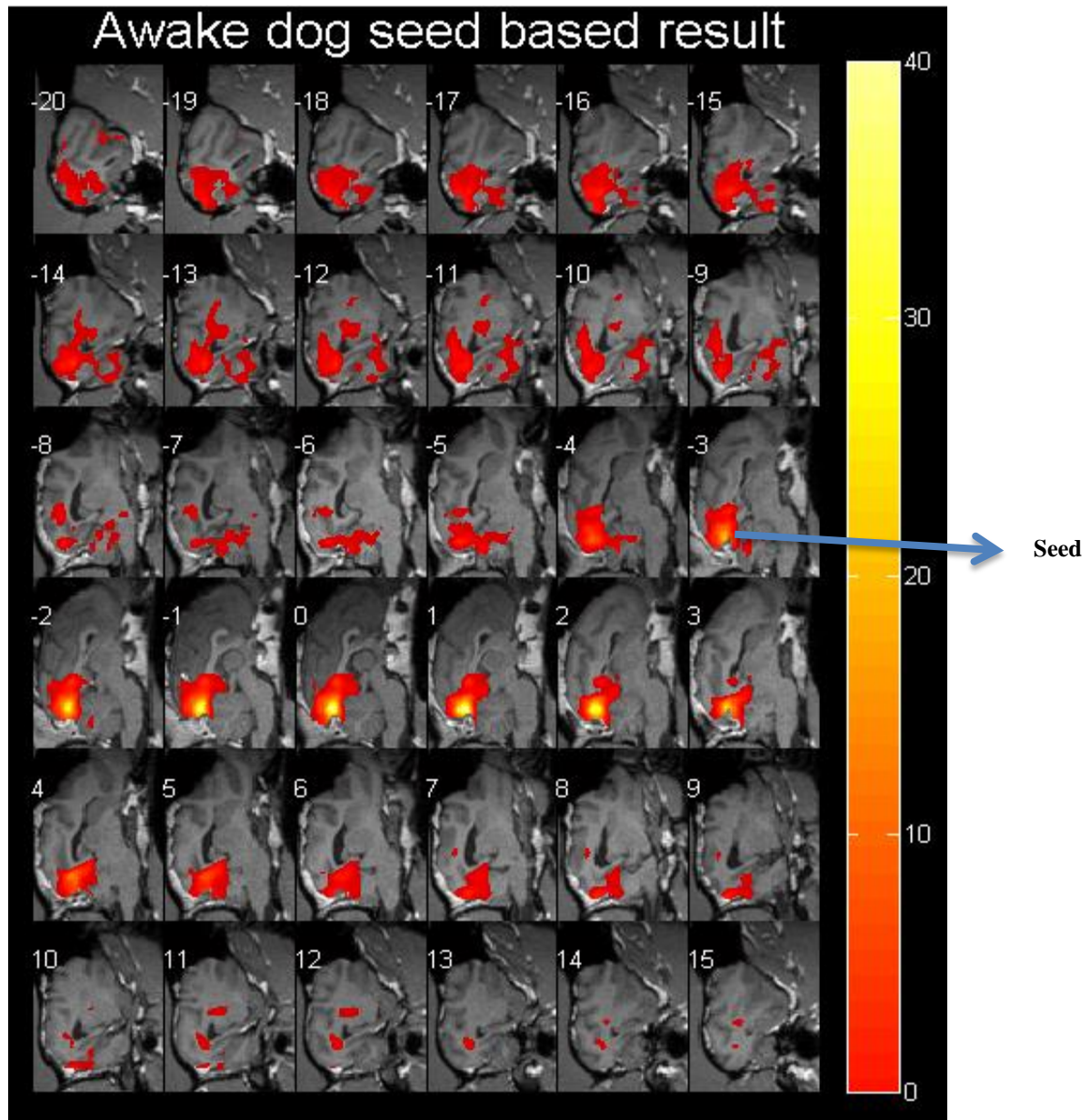


Figure 21: Seed-based connectivity map shows the t-images for the awake dogs. The image was thresholded at corrected- $p<0.0001$ and $|t|>4.11$. The posterior cingulate seed is shown in the figure by an arrow

3.4 Discussion

Connectivity maps from the seed based analysis and ICA for both awake and anesthetized dogs showed that, unlike in humans and monkeys, dogs have localized networks in the anterior and posterior parts. In humans and monkeys, the anterior and

posterior parts would be correlated, forming one distributed network which is known as DMN. On the other hand, in dogs, the anterior and posterior parts of the DMN seem to be dissociated.

In humans, the brain's default mode network is more active in passive settings and during tasks when the brain is not involved in direct attention to the external stimuli. The functions of the DMN can be broadly categorized by two hypotheses, one is "The sentinel hypothesis" [23], where the DMN is thought to be playing the role of monitoring the external environment [4] [55], and the other one is "The internal mentation hypothesis" which says that DMN is involved in internal mentation such as theory of mind, envisioning the future, and autobiographical remembering [23]. The DMN is considered to be made up of many subsystems (brain regions) which have specialized functions. These subsystems converge in to three main hubs in posterior cingulate cortex, anterior cingulate/medial prefrontal cortex and inferior parietal lobule. Each of the subsystems and hubs have their specialized functions. The anterior cingulate cortex is associated with emotional and social processing [56] [57] [58]. The posterior cingulate is involved in self-reflection, recollection and prospection [59] [60]. The posterior cingulate is also implicated in processing of simple emotions [61] [62] [63] [64], but the role of anterior cingulate and posterior cingulate in the emotion processing is different, even though both are activated during the emotion tasks [65]. It has been proposed that the emotional content is stored in the sub regions of the anterior cingulate and when an emotional consequence is demanded, the posterior cingulate provides the code for relevant information from sensory systems to evaluate the emotional content. Therefore the posterior cingulate is associated with retrieval of episodic memories but is not directly

a part of the emotion system [65] [66] [67]. The subsystem consisting of dorsomedial prefrontal cortex has been shown to be involved in self-referential processing [68]. Taken together with reports attributing similar functions to the posterior cingulate and inferior parietal regions [69], it is reasonable to expect that the temporal correlations between these regions serve the purpose of supporting those functions.

It is evident from the above discussion that within the DMN there are at least two different subsystems in the anterior and posterior parts of the brain which interact together to process any information. For example the present or upcoming events are anticipated by the brain in anterior parts such as dorso medial prefrontal cortex with the help of analogies from the previous experience which is stored in the hippocampus and accessed by dorso medial prefrontal cortex through posterior cingulate [70] [55]. Thus, the correlation between the hubs plays an important role and the alteration of these hubs may be associated with brain diseases, loss of consciousness and generally lower level of information processing. For example, a study on epilepsy patients reports that the alteration in the DMN activity is associated with loss of consciousness [71]. In another study it has been shown that children have significantly weaker functional connectivity between the anterior medial prefrontal and posterior cingulate regions of the DMN and children showed lesser DMN activity compared to adults [72] suggesting that anterior-posterior connectivity is critical for supporting higher level cognitive processing in adult humans [73]. The correlation across different brain networks including DMN gets disrupted with the advanced aging and reduced cognitive abilities [74]. These results suggest that anterior-posterior dissociation in the DMN of dogs may suggest lower level of cognitive processing in dogs as compared to humans. Alternatively, it would be

interesting to think of the degree of anterior-posterior association in DMNs across species and across different ages and diseases in humans, as a marker of the level of cognitive processing. Future studies must explore whether calibrating and quantifying the anterior-posterior association in DMNs can be used as a quantitative metric for the level of cognitive processing. Further, previous works in humans [75] have shown that the organization of multiple functional resting networks shifts from a “local” anatomical emphasis in children to a more “distributed” architecture in young adults. Since human development mimics the evolutionary hierarchy, there is reason to believe that dogs represent the part of evolution where DMN is localized, which then becomes more distributed in humans and monkeys.

DMN in humans is directly related to cognitive abilities [36], attention [76] [77], and memory retrieval [23] [55]. It has been shown that the impairments in attention is associated with the disruption in the activation of DMN [78] and the working memory functions depends on the DMN functional connectivity pattern. Further, the involvement of the cingulate regions within the DMN can be used as a working-memory efficiency predictor [79]. In addition to being a predictor of behavioral performance, the DMN in humans has also been shown to be a predictor of individual traits [80] [81] [82] and personality. These human data raise the possibility of using characterization of the DMN in dogs as a predictor of behavioral performance and individual traits. Potentially, this principle can be used to identify dogs with traits suitable for making them useful to humans and also identify the ones that are likely to perform better.

3.5 Conclusions

In this study, we performed functional imaging of anesthetized and awake dogs in order to investigate the default mode network in dog brains. Imaging of awake dogs, achieved through reinforcement-based behavioral adaptation techniques, was performed to rule out anesthesia-related effects. We found that, unlike humans and monkeys, the anterior and posterior regions of the DMN were dissociated in both awake and anesthetized dogs. These results provide insights into the comparative role of the DMN across species. In addition they raise the possibility of using DMN-based characterization for choosing dogs with traits and abilities suitable for training them for tasks in which they are utilized by humans.

Acknowledgments

We thank Yang Zhi from National Institutes of Health for providing gRAICAR code and assisting with its analysis.

3.6 Bibliography

- [1] B. Biswal, F. Yetkin, V. Haughton and J. Hyde, "Functional connectivity in the motor cortex of resting human brain using echo-planar MRI," *Magn. Reson. Med.*, vol. 34, p. 537–541, 1995.
- [2] M. Fox and M. Raichle, "Spontaneous fluctuations in brain activity observed with functional magnetic resonance imaging," *Nat. Rev. Neurosci.*, vol. 8, p. 700–711, 2007.
- [3] M. D. Greicius, B. Krasnow, A. L. Reiss and V. Menon, "Functional connectivity in the resting brain: A network analysis of the default mode hypothesis," *Proceedings of the National Academy of Sciences of the United States of America*, vol. 100, pp. 253-258, 2003.
- [4] D. Gusnard, M. Raichle and M. Raichle, "Searching for a baseline: Functional imaging and the resting human brain," *Nat Rev Neurosci*, vol. 2, p. 685–694, 2001.

- [5] C. Beckmann, M. DeLuca, J. Devlin and S. Smith, "Investigations into resting-state connectivity using independent component analysis," *Philos Trans R Soc Lond B Biol Sci*, vol. 360, pp. 1001-1013, 2005.
- [6] J. Damoiseaux, S. Rombouts, F. Barkhof, P. Scheltens and C. Stam, "Consistent resting-state networks across healthy subjects," *Proc Natl Acad Sci U S A*, vol. 103, pp. 13848-13853, 2006.
- [7] M. Van den Heuvel, R. Mandl and P. H. Hulshoff, "Normalized group clustering of resting-state fMRI data," *PLoS ONE*, vol. 3, no. 4, 2008.
- [8] M. Van den Heuvel, R. Mandl, J. Luigjes and P. H. Hulshoff, "Microstructural Organization of the Cingulum Tract and the level of Default Mode Functional Connectivity," *The Journal of Neuroscience*, vol. 28, no. 43, pp. 10844-10851, 2008.
- [9] D. Cordes, V. Haughton, K. Arfanakis, G. Wendt and P. Turski, "Mapping functionally related regions of brain with functional connectivity," *AJNR Am J Neuroradiol*, vol. 21, no. 9, pp. 1636-1644, 2000.
- [10] D. Auer , "Spontaneous low-frequency blood oxygenation level-dependent fluctuations and functional connectivity analysis of the 'resting' brain," *Magn Reson Imaging*, vol. 26, no. 7, 2008.
- [11] A. Bokde, P. Lopez-Bayo, T. Meindl, S. Pechler, C. Born, F. Faltraco, S. Teipel, H. Moller and H. Hampel, "Functional connectivity of the fusiform gyrus during a face-matching task in subjects with mild cognitive impairment," *Brain*, vol. 129, p. 1113–1124, 2006.
- [12] F. Castellanos, D. Margulies, A. Kelly, L. Uddin, M. Ghaffari, A. Kirsch, D. Shaw, Z. Shehzad, A. Di Martino, B. Biswal, E. Sonuga-Barke, J. Rotrosen, L. Adler and M. Milham, "Cingulate-precuneus interactions: a new locus of dysfunction in adult attention-deficit/hyperactivity disorder," *Biol. Psychiatry*, vol. 63, p. 332–337, 2008.
- [13] M. Greicius, B. Flores, V. Menon, G. Glover, H. Solvason, H. Kenna, A. Reiss and A. Schatzberg, "Resting-state functional connectivity in major depression: abnormally increased contributions from subgenual cingulate cortex and thalamus," *Biol. Psychiatry*, vol. 62, pp. 429-437, 2007.
- [14] M. Greicius, G. Srivastava, A. Reiss and V. Menon, "Default-mode network activity distinguishes Alzheimer's disease from healthy aging: evidence from functional MRI," *Proc. Natl. Acad. Sci. U. S. A*, vol. 101, p. 4637–4642, 2004.
- [15] S. Rombouts and P. Scheltens, "Functional connectivity in elderly controls and AD patients using resting state fMRI: a pilot study," *Curr. Alzheimer Res*, vol. 2, pp. 115-116, 2005.
- [16] L. Tian, T. Jiang, Y. Wang, Y. Zang, Y. He, M. Liang, M. Sui, Q. Cao, S. Hu, M. Peng and Y. Zhuo, "Altered resting-state functional connectivity patterns of anterior cingulate cortex in adolescents with attention deficit hyperactivity disorder," *Neurosci. Lett.*, vol. 400, pp. 39-43, 2006.
- [17] H. Whalley, E. Simonotto, I. Marshall, D. Owens, N. Goddard, E. Johnstone and S. Lawrie, "Functional disconnectivity in subjects at high genetic risk of schizophrenia," *Brain*, vol. 128, pp. 2097-2108, 2005.
- [18] A. Fornito and E. Bullmore, "What can spontaneous fluctuations of the blood

- oxygenation-level-dependent signal tell us about psychiatric disorders?," *Curr.Opin. Psychiatry*, vol. 23, no. 3, pp. 239-249, 2010.
- [19] M. Van den Heuvel and H. Hulshoff Pol, "Exploring the brain network: a review on resting-state fMRI functional connectivity," *Eur Neuropsychopharmacol.*, vol. 20, pp. 519-534, 2010.
- [20] J. Damoiseaux, C. Beckmann, E. Arigita, F. Barkhof, P. Scheltens, C. Stam, S. Smith and S. Rombouts, "Reduced resting-state brain activity in the “default network” in normal aging," *Cereb Cortex*, vol. 18, no. 8, pp. 1856-1864, 2008.
- [21] M. Greicius, "Resting-state functional connectivity in neuropsychiatric disorders," *Curr Opin Neurol.*, vol. 21, pp. 424-430, 2008.
- [22] M. Raichle, A. MacLeod, A. Snyder, W. Powers, D. Gusnard and G. Shulman, "A default mode of brain function," *Proc Natl Acad Sci USA*, vol. 98, pp. 676-682, 2001.
- [23] R. Buckner, J. Andrews-Hanna and D. Schacter, "The brain's default network: Anatomy, function, and relevance to disease," *Ann N Y Acad Sci*, vol. 1124, pp. 1-38, 2008.
- [24] D. Mantini, A. Gerits, K. Nelissen, J. Durand, O. Joly, L. Simone, H. Sawamura, C. Wardak, G. Orban, R. Buckner and V. W, "Default mode of brain function in monkeys," *J Neurosci.*, vol. 31, no. 36, pp. 12954-12962, 2011.
- [25] L. Becerra, G. Pendse, P.-C. Chang, J. Bishop and D. Borsook, "Robust Reproducible Resting State Networks in the Awake Rodent Brain," *PLoS ONE*, vol. 6, no. 10, 2011.
- [26] N. Zhang, P. Rane, W. Huang, Z. Liang, D. Kennedy, J. Frazier and J. King, "Mapping resting-state brain networks in conscious animals," *J Neurosci Methods.*, vol. 189, no. 2, pp. 186-196, 2010.
- [27] Z. Liang, J. King and N. Zhang, "Uncovering intrinsic connectional architecture of functional networks in awake rat brain," *J Neurosci.*, vol. 31, no. 10, pp. 3776-3783, 2011.
- [28] H. Lu, Q. Zou, H. Gu, M. Raichle, E. Steina and Y. Yanga, "Rat brains also have a default mode network," *PNAS of USA*, vol. 109, no. 10, p. 3979–3984, 2011.
- [29] J. Upadhyay, S. Baker, P. Chandran, L. Miller, Y. Lee, G. Marek, U. Sakoglu, C.-L. Chin and F. Luo, "Default-Mode-Like Network Activation in Awake Rodents," *PLOS ONE*, vol. 6, no. 11, 2011.
- [30] H. Lu, Y. Zuo, H. Gu, J. Waltz, W. Zhan, C. Scholl, W. Rea, Y. Yang and E. Stein, "Synchronized delta oscillations correlate with the resting-state functional MRI signal," *Proc Natl Acad Sci U S A.*, vol. 104, no. 46, pp. 18265-18269, 2007.
- [31] K. Wang, M. van Meer, K. van der Marel, A. van der Toorn, L. Xu, Y. Liu, M. Viergever, T. Jiang and R. Dijkhuizen, "Temporal scaling properties and spatial synchronization of spontaneous blood oxygenation level-dependent (BOLD) signal fluctuations in rat sensorimotor network at different levels of isoflurane anesthesia," *NMR Biomed*, vol. 24, no. 1, pp. 61-67, 2011.
- [32] M. Greicius, V. Kiviniemi, O. Tervonen, V. Vainionpää, S. Alahuhta, A. Reiss and V. Menon, "Persistent default-mode network connectivity during light sedation,"

Hum Brain Mapp., vol. 29, no. 7, pp. 839-847, 2008.

- [33] G. Berns, A. Brooks and M. Spivak, "Functional MRI in awake unrestrained dogs," *PLoS One*, vol. 7, no. 5, 2012.
- [34] H. Jia, O. Pustovyy, P. Waggoner, R. Beyers, J. Schumacher, C. Wildey, J. Barrett, E. Morrison, N. Salibi, T. Denney, V. Vodyamoy and G. Deshpande, "Functional MRI of the Olfactory System in Conscious Dogs," *PLoS ONE*, p. Under review, 2013.
- [35] D. M. Cole, S. M. Smith and C. F. Beckmann, "Advances and Pitfalls in the Analysis and Interpretation of Resting-State FMRI Data," *Front Syst Neurosci*, vol. 4, no. 8, 2010.
- [36] W. Seeley, V. Menon, A. Schatzberg, J. Keller, G. Glover, H. Kenna, A. Reiss and M. Greicius, "Dissociable Intrinsic Connectivity Networks for Salience Processing and Executive Control," *J Neurosci.*, vol. 27, no. 9, pp. 2349-2356, 2007.
- [37] R. Bluhm, E. Osuch, R. Lanius, K. Boksman, R. Neufeld, J. Théberge and P. Williamson, "Default mode network connectivity: effects of age, sex, and analytic approach," *Neuroreport.*, vol. 19, no. 8, pp. 887-891, 2008.
- [38] X. Long, X. Zuo, V. Kiviniemi, Y. Yang, Q. Zou, C. Zhu, T. Jiang, H. Yang, Q. Gong, L. Wang, K. Li, S. Xie and Y. Zang, "Default mode network as revealed with multiple methods for resting-state functional MRI analysis," *J Neurosci Methods.*, vol. 171, no. 2, pp. 349-355, 2008.
- [39] L. Ma, B. Wang, X. Chen and J. Xiong, "Detecting functional connectivity in the resting brain: a comparison between ICA and CCA," *Magn Reson Imaging.*, vol. 25, no. 1, pp. 47-56, 2007.
- [40] Z. Yang, X. Zuo, P. Wang, Z. Li, S. LaConte, P. Bandettini and X. Hu, "Generalized RAICAR: discover homogeneous subject (sub)groups by reproducibility of their intrinsic connectivity networks," *Nuroimage*, vol. 63, no. 1, pp. 403-414, 2012.
- [41] M. Brant-Zawadzki, G. Gillan and W. Nitz, "MP RAGE: a three-dimensional,T1-weighted, gradient-echo sequence—initial experience in the brain," *Radiology*, vol. 182, p. 769–775, 1992.
- [42] K. Butts, S. J. Riederer, R. L. Ehman, R. M. Thompson and C. R. Jack, "Interleaved echo planar imaging on a standard MRI system," *Magnetic Resonance in Medicine*, vol. 31, no. 1, p. 67–72, 1994.
- [43] K. Friston, A. Holmes, K. Worsley, J. Poline, C. Frith and J. Frackowiak, "Statistical parametric maps in functional imaging: A general linear approach," *Human Brain Mapping*, vol. 2, no. 4, pp. 189-210, 1995.
- [44] Y. Chao-Gan and Z. Yu-Feng, "DPARSF: A MATLAB Toolbox for "Pipeline" Data Analysis of Resting-State fMRI," *Front Syst Neurosci*, vol. 4, no. 13, 2010.
- [45] X.-W. Song, Z.-Y. Dong, X.-Y. Long, S.-F. Li, X.-N. Zuo, C.-Z. Zhu, Y. He, C.-G. Yan and Y.-F. Zang, "REST: A Toolkit for Resting-State Functional Magnetic Resonance Imaging Data Processing," *PLoS ONE*, vol. 6, no. 9, 2011.
- [46] D. W. Shattuck and R. M. Leahy, "BrainSuite: An automated cortical surface identification tool," *Medical Image Analysis*, vol. 6, no. 2, pp. 129-142, 2002.
- [47] K. J. Friston, S. Williams, R. Howard, R. S. Frackowiak and R. Turner, "Movement-related effects in fMRI time-series," *Magnetic Resonance in Medicine*, vol. 35, no. 3,

- pp. 346-355, 1996.
- [48] J. Ashburner and K. Friston, "Nonlinear spatial normalization using basis functions," *Human Brain Mapping*, vol. 7, no. 4, pp. 254-266, 1999.
 - [49] R. Datta, J. Lee, J. Duda, B. Avants, C. Vite, B. Tseng, J. Gee, G. Aguirre and G. Aguirre, "A digital atlas of the dog brain," *PLoS One*, vol. 7, no. 12, p. e52140, 2012.
 - [50] N. Logothetis, J. Pauls, M. Augath, T. Trinath and A. Oeltermann, "Neurophysiological investigation of the basis of the fMRI signal," *Nature*, vol. 412, no. 6843, pp. 150-157, 2001.
 - [51] G. Brown, S. Yamada and T. Sejnowski, "Independent component analysis at the neural cocktail party," *Trends Neurosci.*, vol. 24, no. 1, pp. 54-63, 2001.
 - [52] A. Bell and T. Sejnowski, "An information-maximization approach to blind separation and blind deconvolution," *Neural Comput*, vol. 7, no. 6, pp. 1129-1159, 1995.
 - [53] V. Calhoun, T. Adali, G. Pearson and J. Pekar, "A method for making group inferences from functional MRI data using independent component analysis," *Hum Brain Mapp*, vol. 14, no. 3, pp. 140-151, 2001.
 - [54] V. Calhoun, K. Kiehl and G. Pearson, "Modulation of temporally coherent brain networks estimated using ICA at rest and during cognitive tasks," *Hum Brain Mapp*, vol. 29, no. 7, pp. 828-838, 2008.
 - [55] D. W. T. Gilbert, "Prospection: experiencing the future," *Science*, vol. 317, no. 5843, pp. 1351-1354., 2007.
 - [56] T. Wager, K. Phan, I. Liberzon and S. Taylor, "Valence, gender, and lateralization of functional brain anatomy in emotion: a meta-analysis of findings from neuroimaging," *Neuroimage*, vol. 19, no. 3, pp. 513-531, 2003.
 - [57] K. Phan, T. Wager, S. Taylor and I. Liberzon, "Functional neuroanatomy of emotion: a meta-analysis of emotion activation studies in PET and fMRI," *Neuroimage*, vol. 16, no. 2, pp. 331-348, 2002.
 - [58] J. Mitchell, T. Heatherton and C. Macrae, "Distinct neural systems subserve person and object knowledge," *Proc Natl Acad Sci U S A.*, vol. 99, no. 23, pp. 15238-15243, 2002.
 - [59] S. Johnson, L. Baxter, L. Wilder, J. Pipe, J. Heiserman and G. Prigatano, "Neural correlates of self-reflection," *Brain*, vol. 125, no. Pt 8, pp. 1808-1814, 2002.
 - [60] R. Buckner and D. Carroll, "Self-projection and the brain," *Trends Cogn Sci.* , vol. 11, no. 2, pp. 49-57, 2007.
 - [61] E. Neafsey, R. Terreberry, K. Hurley, K. Ruit and R. Frysztak, "Anterior cingulate cortex in rodents: connections, visceral control functions, and implications for emotion," in *Neurobiology of Cingulate Cortex and Limbic Thalamus*, Birkhäuser Boston, 1993, pp. 207-223.
 - [62] M. George, T. Ketter, P. Parekh, P. Herscovitch and R. Post, "Gender differences in regional cerebral blood flow during transient self-induced sadness or happiness," *Biol Psychiatry.* , vol. 40, no. 9, pp. 859-871, 1996.
 - [63] M. George, T. Ketter, P. Parekh, B. Horwitz, P. Herscovitch and R. Post, "Brain

- activity during transient sadness and happiness in healthy women," *Am J Psychiatry*, , vol. 152, no. 3, pp. 341-351, 1995.
- [64] H. Mayberg, M. Liotti, S. Brannan, S. McGinnis, R. Mahurin, P. Jerabek, J. Silva, J. Tekell, C. Martin, J. Lancaster and P. Fox, "Reciprocal limbic-cortical function and negative mood: converging PET findings in depression and normal sadness," *Am J Psychiatry*., vol. 156, no. 5, pp. 675-682, 1999.
- [65] B. Vogt, L. Vogt and S. Laureys, "Cytology and functionally correlated circuits of human posterior cingulate areas," *Neuroimage*, vol. 29, no. 2, pp. 452-466, 2006.
- [66] H. Lou, B. Luber, M. Crupain, J. Keenan, M. Nowak, T. Kjaer, H. Sackeim and S. Lisanby, "Parietal cortex and representation of the mental Self.," *Proc Natl Acad Sci U S A* , vol. 101, no. 17, pp. 6827-6832, 2004.
- [67] B. Lundstrom, M. Ingvar and K. Petersson, "The role of precuneus and left inferior frontal cortex during source memory episodic retrieval.," *Neuroimage*, vol. 27, no. 4, pp. 824-834, 2005.
- [68] G. Northoff, A. Heinzel, M. de Greck, F. Bermpohl, H. Dobrowolny and J. Panksepp, "Self-referential processing in our brain--a meta-analysis of imaging studies on the self.," *Neuroimage*, vol. 31, no. 1, pp. 440-457, 2006.
- [69] B. Harrison, J. Pujol, M. López-Solà, R. Hernández-Ribas, J. Deus, H. Ortiz, C. Soriano-Mas, M. Yücel, C. Pantelis and N. Cardoner, "Consistency and functional specialization in the default mode brain network.," *Proc Natl Acad Sci U S A*, vol. 105, no. 28, pp. 9781-9786, 2008 Jul 15.
- [70] G. Deshpande, P. Santhanam and X. Hu, "Instantaneous and causal connectivity in resting state brain networks derived from functional MRI data.," *Neuroimage*., vol. 54, no. 2, pp. 1043-1052, 2011 Jan 15.
- [71] N. Danielson, J. Guo and H. Blumenfeld, "The default mode network and altered consciousness in epilepsy," *Behav Neurol*., vol. 24, no. 1, pp. 55-65, 2011.
- [72] K. Supekar, L. Uddin, K. Prater, H. Amin, M. Greicius and V. Menon, "Development of functional and structural connectivity within the default mode network in young children.," *Neuroimage*., vol. 52, no. 1, pp. 290-301, 2010.
- [73] P. Fransson, B. Skiöld, S. Horsch, A. Nordell, M. Blennow, H. Lagercrantz and U. Aden, "Resting-state networks in the infant brain," *Proc Natl Acad Sci U S A*., vol. 104, no. 39, pp. 15531-15536, 2007 Sep 25.
- [74] J. Andrews-Hanna, A. Snyder, J. Vincent, C. Lustig, D. Head, M. Raichle and R. Buckner, "Disruption of large-scale brain systems in advanced aging," *Neuron*, vol. 56, no. 5, pp. 924-935, 2007 Dec 6.
- [75] D. Fair, A. Cohen, J. Power, N. Dosenbach, J. Church, F. Miezin, B. Schlaggar and S. Petersen, "Functional brain networks develop from a "local to distributed" organization," *PLoS Comput Biol*., vol. 5, no. 5, 2009.
- [76] M. Hampson, N. Driesen, P. Skudlarski, J. Gore and R. Constable, "Brain connectivity related to working memory performance," *J Neurosci*., vol. 26, no. 51, pp. 13338-13343, 2006 Dec 203.
- [77] R. Leech, S. Kamourieh, C. Beckmann and D. Sharp, "Fractionating the default mode network: distinct contributions of the ventral and dorsal posterior cingulate

- cortex to cognitive control.," *J Neurosci.*, vol. 31, no. 9, pp. 3217-3124, 2011 Mar 2.
- [78] V. Bonnelle, R. Leech, K. Kinnunen, T. Ham, C. Beckmann, X. De Boissezon, R. Greenwood and D. Sharp, "Default mode network connectivity predicts sustained attention deficits after traumatic brain injury," *J Neurosci.*, vol. 31, no. 38, pp. 13442-13451, 2011.
- [79] F. Esposito, A. Aragri, V. Latorre, T. Popolizio, T. Scarabino, S. Cirillo, E. Marciano, G. Tedeschi and F. Di Salle, "Does the default-mode functional connectivity of the brain correlate with working-memory performances?," *Arch Ital Biol.*, vol. 147, no. 1-2, pp. 11-20, 2009.
- [80] X. Lei, Z. Zhao and H. Chen, "Extraversion is encoded by scale-free dynamics of default mode network," *Neuroimage*. , vol. 74, pp. 52-57, 2013.
- [81] G. Knyazev, "Extraversion and anterior vs. posterior DMN activity during self-referential thoughts," *Front Hum Neurosci.*, vol. 6, no. 348, 2012.
- [82] L. Wei, X. Duan, Y. Yang, W. Liao, Q. Gao, J. Ding, Z. Zhang, W. Zeng, Y. Li, G. Lu and H. Chen, "The synchronization of spontaneous BOLD activity predicts extraversion and neuroticism," *Brain Res.* , vol. 1419, pp. 68-75, 2011.

Chapter 4

A realistic framework for investigating decision-making in the brain with high spatio-temporal resolution using simultaneous EEG/fMRI and joint ICA

Abstract

Many decisions involve making intertemporal choices between immediate and future prospects. Such comparisons are ubiquitous across many decision domains ranging from health, social, financial, and environmental contexts. The basic temporal decision making paradigm has been associated with real-world problematic behaviors, but it does not adequately model real-world situations wherein there are immediate and delayed costs (as well as rewards); and the rewards and costs of future outcomes are probabilistic rather than certain. Extensive electroencephalography (EEG) literature exists on event-related potentials (ERPs) associated with reward and decision making. However, due to poor spatial localization, existing results can mostly capture only cortical sources. In contrast, the functional magnetic resonance imaging (fMRI) studies of intertemporal choice are silent on the important aspect of fast temporal dynamics of decision making, but they can spatially localize deeper structures. In this study, we investigate the spatio-temporal dynamics of neural substrates of intertemporal decision making by acquiring simultaneous EEG/fMRI along with a novel decision making paradigm that relies on rewards and costs with varying probabilities. Unlike previous approaches, we propose joint independent component analysis such that the native resolution of either modality is not sacrificed to match the other. We show that the joint independent components derived from EEG/fMRI data obtained from the proposed task can be modeled as a linear

combination of corresponding joint components obtained from simpler decision making tasks separately involving delay discounting, uncertainty, reward and cost, demonstrating that the neural substrates engaged by the proposed task encompasses those underlying disparate simpler tasks. Overall, our approach provides a realistic and novel framework for investigating the neural substrates of decision making with high spatio-temporal resolution.

4.1 Introduction

Many decisions involve making intertemporal choices between immediate and future prospects. Such comparisons are ubiquitous across many decision domains ranging from health [1] social [2] financial [3], and environmental [4] contexts. Often, the immediate option might be gratifying (e.g., consumption of alcohol or a high-caloric dessert), but can lead to detrimental long-term consequences (e.g., health-related problems, addiction, obesity, death, etc.) if selected too often. Individuals must exhibit cognitive control over immediate needs, wants, or impulses to attain positive long-term benefits or avoid the potential for long-term costs [5]. Research supports that some individuals might have a greater propensity for risky or impulsive behavior over others [6], and poor performance on behavioral measures of self-control or impulsivity (e.g., laboratory tasks) are associated with real-world behavior problems (e.g., drug/alcohol use and poor diet [7, 8, 9]). Understanding *how* and *when* people control or succumb to immediate impulses is necessary for designing treatments for long-term health through improved decision making, particularly when immediately gratifying options have long-term potential for dire consequences.

Despite the plethora of evidence that future prospects are discounted, the basic mechanisms underlying intertemporal choice remain poorly understood and under-examined [5, 6, 7]. In part, this is because the constructs associated with self-control and decision making have developed across different fields of psychology and neuroscience (i.e., cognitive, social, clinical), relying on different conceptual and operational definitions of this construct (i.e., impulsivity, risk-taking, self-control, delay discounting etc.) and methods (e.g., self-reports, behavioral tasks, etc.). The lack of integration leads to disconnect in understanding the basic mechanisms. Furthermore, although the basic temporal decision making paradigm has been associated with real-world problematic behaviors, it does not adequately model real-world situations wherein there are immediate and delayed costs (as well as rewards); and the rewards and costs of future outcomes are probabilistic rather than certain. Accounting for some of these complexities will allow for a better understanding of the mechanisms and processes involved in temporal decision making.

Time plays a critical factor in decision making [10]. Almost all individuals prefer an immediate to delayed reward when the latter is far in the future (e.g., 10 years [11]). Longer time spans may appear uncertain, which might underscore the general preference for the immediate option. Perception of time has been recently applied to intertemporal choice [12, 13]. However, most research examining temporal decision making assumes that the prospects feature two time periods (now and future) that are certain – despite that people might not consider future rewards as guaranteed. Indeed, future rewards and costs in the real world are most likely probabilistic (e.g., many alcoholics do not develop cirrhosis). Comparable to temporal decision making, modeling probability of reward

(instead of time) yields similar choice patterns (albeit, inversed for deciding between certain and probabilistic choices) and similar functions are used to describe the choice data [11]. The similarity between temporal and probability discounting speaks to a potential underlying mechanism common to both tasks. Yet, most research treats these concepts as distinct and tends to examine time and probability separately –even though many concede there is overlap [14, 15]. Furthermore, temporal discounting is more commonly associated with impulsivity (noted in the recently edited volume *Impulsivity: The behavioral and neurological science of discounting* [16]), whereas probabilistic outcomes are usually associated with one's propensity to engage in risk (e.g. [6, 17]). Moreover, there is a gap in the literatures addressing how time and probability might interface with one another and in examining the commonalities and dissociations between the two constructs.

Another potential issue with traditional measures of temporal decision making is the overemphasis on rewards or gains, with a few exceptions where prospects are framed as losses [3].The decision to drink may not be weighed against the long-term rewards connected to abstinence (e.g., physical health), but rather the long-term costs associated with problematic use (e.g., work and social impairments, cirrhosis of the liver). The difference between modeling costs versus rewards is not trivial, as costs are discounted less over time than are rewards [18]. However, most everyday decisions involve positive and negative attributes within a given option. Consequently, depicting real-world decision making in the lab requires a paradigm that better captures the complexity of choice parameters encountered in real-world situations.

We developed a new paradigm which is more ecologically valid and realistic in elucidating the empirical links between the cognitive processes underlying intertemporal choice and decision making.

In the new Paradigm, we propose that the basic temporal decision task may not entirely characterize the real-world decisions it purports to model. We expanded the basic task by varying several parameters such as: a) Including the probabilistic factor associated with future prospects, b) Varying whether the immediate option is a cost and/or reward, and c) Seeing whether the delayed option is a cost and/or reward. These parameters can be examined separately or in combination such that it allows for the effects of each parameter on discounting to be examined across tasks, as well as whether the interaction between each parameter carries added effects.

The neural bases of intertemporal decision making have been investigated using both electroencephalography (EEG) and functional magnetic resonance imaging (fMRI). EEG and fMRI reflect complementary correlates of neural activity. EEG measures the electrical correlates of neural activity, providing a more direct measure with a temporal resolution on the scale of 5-10 milliseconds, making them ideal for capturing the fast neural processes underlying decision-making. Extensive EEG literature exists on event-related potentials (ERPs) associated with reward and decision making [19] [20] [21]. However, measuring electrical currents on the surface of the scalp is associated with poor spatial localization, and hence, existing results can mostly capture only cortical sources such as the anterior cingulate and not deep structures such as the ventral striatum. In contrast, fMRI measures the hemodynamic response secondary to neuronal activity with superior spatial resolution but poor temporal resolution (typically on the order of

seconds). Therefore, fMRI studies of intertemporal choice [14] are silent on the important aspect of fast temporal dynamics of decision making – though they can spatially localize deeper structures. As such, combining EEG and fMRI data provides complementary measures of neural electrical activity at high temporal resolution and hemodynamics at high spatial resolution. Two main approaches are employed for integration of simultaneously recorded EEG and fMRI: 1) using fMRI activations as priors for EEG source localization and 2) examination of co-variations of the BOLD signal with different EEG signatures [22]. These approaches either sacrifice the spatial resolution of fMRI or temporal resolution of EEG. In contrast, in this study we adopt joint independent component analysis (jICA) [23] which preserves the temporal resolution of EEG and spatial resolution of fMRI. This is the *first* EEG/fMRI study to explore the neural substrates of intertemporal choice with high spatio-temporal resolution. Using the high spatio-temporal resolution provided by simultaneous EEG/fMRI data and jICA, we tested the hypothesis that the neural substrates underlying our proposed realistic paradigm encompass the neural substrates of decision making involving delay discounting, uncertainty, reward and cost. In order to do so, we tested whether jICA components derived from EEG/fMRI data obtained from the proposed task can be modeled as a linear combination of corresponding jICA components obtained from simpler decision making tasks separately involving delay discounting, uncertainty, reward and cost.

4.2 Materials and Methods

4.2.1 Subjects

6 healthy subjects (1 female, 5 male), 23 ± 2.4 years of age) with no history of neurological disorders participated in this simultaneous EEG-fMRI study. Cushions were placed inside the coil to absorb the pressure from the EEG electrodes on the head and to restrict head movement in the coil.

4.2.2 Tasks and Parameters

The entire study for each subject contained a single session of simultaneous EEG-fMRI recording for the different decision tasks described below.

(1) *Temporal Task - Reward.* This was a standard delay discounting task wherein the subjects had to choose between an immediate reward (e.g., \$20 to \$80) and a fixed delay reward (e.g., \$100) at several time intervals (e.g., 1 month, 6 months, 1 year, 5 years, and 10 years, as illustrated in Figure 22).



Figure 22: Standard Task

(2) *Temporal Task - Cost.* Similar to *Temporal Task-Reward* except that costs were used. The subjects had to choose between an immediate cost (e.g., -\$20 to -\$80) and a fixed delay cost (e.g., -\$100) at several time intervals.

(3) *Temporal Task - Mixed Reward and Cost.* The subjects had to choose a smaller immediate reward with a larger delayed cost or a smaller immediate cost with a larger delayed reward. For example, Option 1: Gain \$20 now and lose \$100 in 1 year, and

Option 2: Lose \$40 now and gain \$100 in one year. Trials were based on crossing reward and cost combinations with immediate and future time periods.

(4) Uncertainty Task - Reward only. This version is similar to the temporal task, however, probabilities (depicted as a pie graph) were used instead of time such that different probabilities (e.g., .1, .3, .5, .7, and .9) were used with a fixed amount (e.g., \$100) and compared to varying immediate amounts (e.g., \$20, \$40, \$60, and \$80).

(5) Uncertainty Task - Cost only. This task was identical to the previous task, however, monetary amounts were presented as a loss (e.g. -\$100).

(6) Uncertainty Task - Mixed Reward and Cost. Similar to the temporal version above (task-3), participants chose between two options that had a reward and a cost at different probability intervals: E.g., Option 1: gain \$20 now and 50 % chance of losing \$100, and Option 2: Lose \$40 now and 50% chance of gaining \$100. Trials were based on crossing reward and cost combinations with varying probabilities (e.g., .1, .3, .5, .7, and .9).

(7) Temporal Task with Uncertainty - Mixed Reward and Costs. The subjects had to choose a smaller immediate reward with a larger delayed cost or a smaller immediate cost with a larger delayed reward and future prospects were associated with varying probabilities of receipt. For example, Option 1: Gain \$20 now with a 50 % chance of losing \$100 in 1 year, and Option 2: Lose \$40 now and 50% chance of gaining \$100 in 1 year (See figure 23 for example).



Figure 23: Temporal-Uncertainty Mixed Reward and Costs decision Task Trial

(8) *Control Task*: Choose the larger amount between two certain immediate outcomes.

For all tasks, the trials were presented in a random order, but participants completed tasks in a block. Random presentation of trials can lead to consistent responses [24].

4.2.3 fMRI data acquisition

MRI data were collected on a 3T Siemens Verio scanner using a 12-channel matrix head coil. Functional images were acquired using a multiband gradient echo-planar imaging sequence [25] with 30ms TE, 600ms TR, 55° flip angle and $64 \times 64 \times 16$ acquisition matrix. T1-weighted structural images were acquired issuing a 3D anatomic MPRAGE sequence of 176 sagittal slices of 1mm thickness with 2.52ms TE, 1900ms TR, 9° flip angle and 256 x 256 x 176 acquisition matrix.

4.2.4 EEG Data Acquisition

MR-compatible 64 channel EEG amplifiers (Brain Products, GmbH, Germany) and an MR-compatible EEG cap (BrainCap MR, Falk Minow Services, Herrsching-Breitbrunn, Germany) with 63; 10-20 system distributed scalp electrodes and an ECG electrode were used for simultaneous EEG acquisitions. For simultaneous EEG-fMRI recordings, the EEG data acquisition clock was synchronized with the MRI scanner clock using Brain Product's SyncBox, resulting in exactly 10,000 data points per TR interval. EEG data were digitized with a sampling frequency of 5kHz and 0.5 μ Vresolution, within a DC-250Hz frequency range and with reference to FCz. Impedance at all recording electrodes was less than 20 k Ω .

4.2.5 fMRI data pre-processing

The functional MRI data obtained from each of the subject was realigned by taking the first image as the reference for all other scans using the least squares approach and a 6 parameter (rigid body) spatial transformation to do motion correction. Then the images were resliced and normalized to EPI MNI template and spatially smoothed with a Gaussian filter with 6mm FWHM using SPM toolbox [26]. A flowchart illustrating fMRI preprocessing steps is shown in Figure 24. After standard pre-processing of fMRI, activation t-maps (first level analysis) at the individual subject level were obtained for each task by contrasting the given task against the control task using SPM8 software.

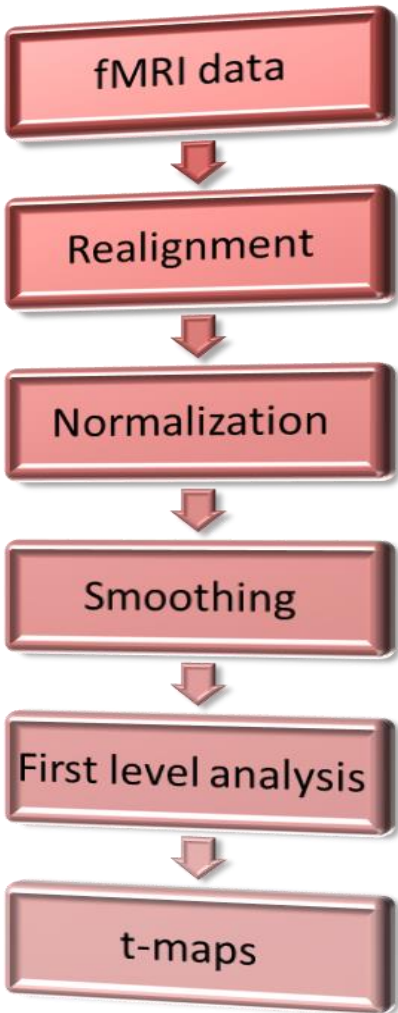


Figure 24: fMRI Pre-Processing and 1st level Analysis

4.2.6 EEG data pre-processing

Prior to data analysis, the recorded EEG data from EPI and MB-EPI sequences were preprocessed by Brain Vision Analyzer 2.0 software (Brain Products) to reduce artifacts derived from the simultaneous EEG–fMRI environment. First, MRI scanning artifacts were reduced by the averaged artifact subtraction (AAS) method [27]. An artifact template was created by segmenting and averaging the data according to the onset of each volume within a sliding window consisting of 41 consecutive volumes, and subtracted

from the raw EEG data. Secondly, cardioballistic artifacts were removed by using the “moving template subtraction” approach, in which R peaks were detected in the low-pass-filtered ECG signal and used to construct a delayed average artifact template over 21 consecutive heartbeat events in a sliding-window approach, which was subtracted from the original EEG signal. With MRI gradient and BCG artifact removed, EEG data were further processed by ocular artifact reduction (via ICA). The resulting EEG data were then low-pass filtered with the cutoff set at 40 Hz (24 dB/oct) and high-pass filtered with the cutoff set at 0.1Hz (24 dB/oct), downsampled to 250 Hz, and re-referenced to mean TP9 and TP10 electrodes. For deriving response-related ERPs, 800 ms epochs were obtained from the pre-processed EEG data, extending 200 prior to and 600ms following the choice event. For baseline correction, the mean voltage associated with each electrode during the 200-ms interval preceding the event was subtracted from each sample of that electrode. For each subject, electrode and task, the ERP obtained from the control task was subtracted from the ERP obtained from the given task. The resulting ERP from each electrode was then concatenated before inputting into the jICA algorithm. A flowchart illustrating EEG preprocessing steps is shown in Figure 25.

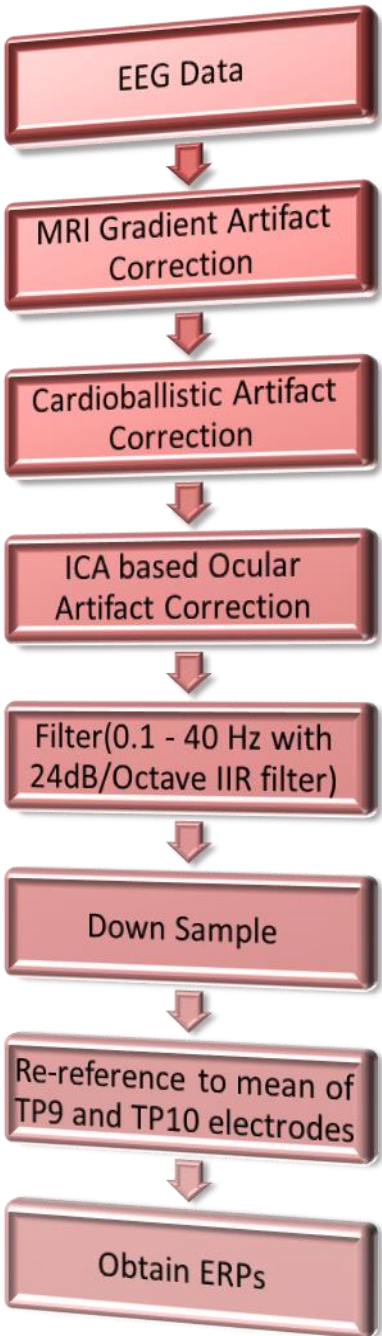


Figure 25: EEG Pre-Processing and 1st level Analysis

4.2.7 Joint Independent Component Analysis (jICA)

jICA is a second level analysis algorithm which assumes spatial/temporal independence of the fMRI/ERP sources, respectively. It also assumes that the ERPs and

BOLD fMRI responses are generated by similar neuronal sources and hence the mixing of ERP and fMRI sources can be represented by a single matrix. Joint ICA algorithm maximizes the spatial independence of the fMRI data and the temporal independence of the ERP data and identifies the linked components that show the common inter-subject co-variation [28, 29].

When ICA is applied separately to EEG and fMRI, we assume the acquired signals to be $X_E = A_E S_E$ and $X_F = A_F S_F$ respectively, where A_E and A_F are the mixing matrices for EEG and fMRI respectively, and S_E and S_F are statistically independent non-Gaussian source time series and locations respectively. The jICA algorithm assumes a single mixing matrix A for both the modalities. Consequently, the acquired signals can be represented as

$$[X_E \ X_F] = A * [S_E \ S_F]$$

Where, S_E and S_F represent the EEG and fMRI source signals respectively. The t-maps obtained from first level fMRI analysis, along with the concatenated ERPs from all electrodes obtained from first level EEG analysis, for all tasks (except the control task), were input in an ordered way (subjects-by-voxels and subjects-by-time points for fMRI & EEG, respectively) into the Fusion ICA toolbox [23, 30] to obtain joint ICA components. A flowchart illustrating joint ICA analysis is shown in Figure 26.

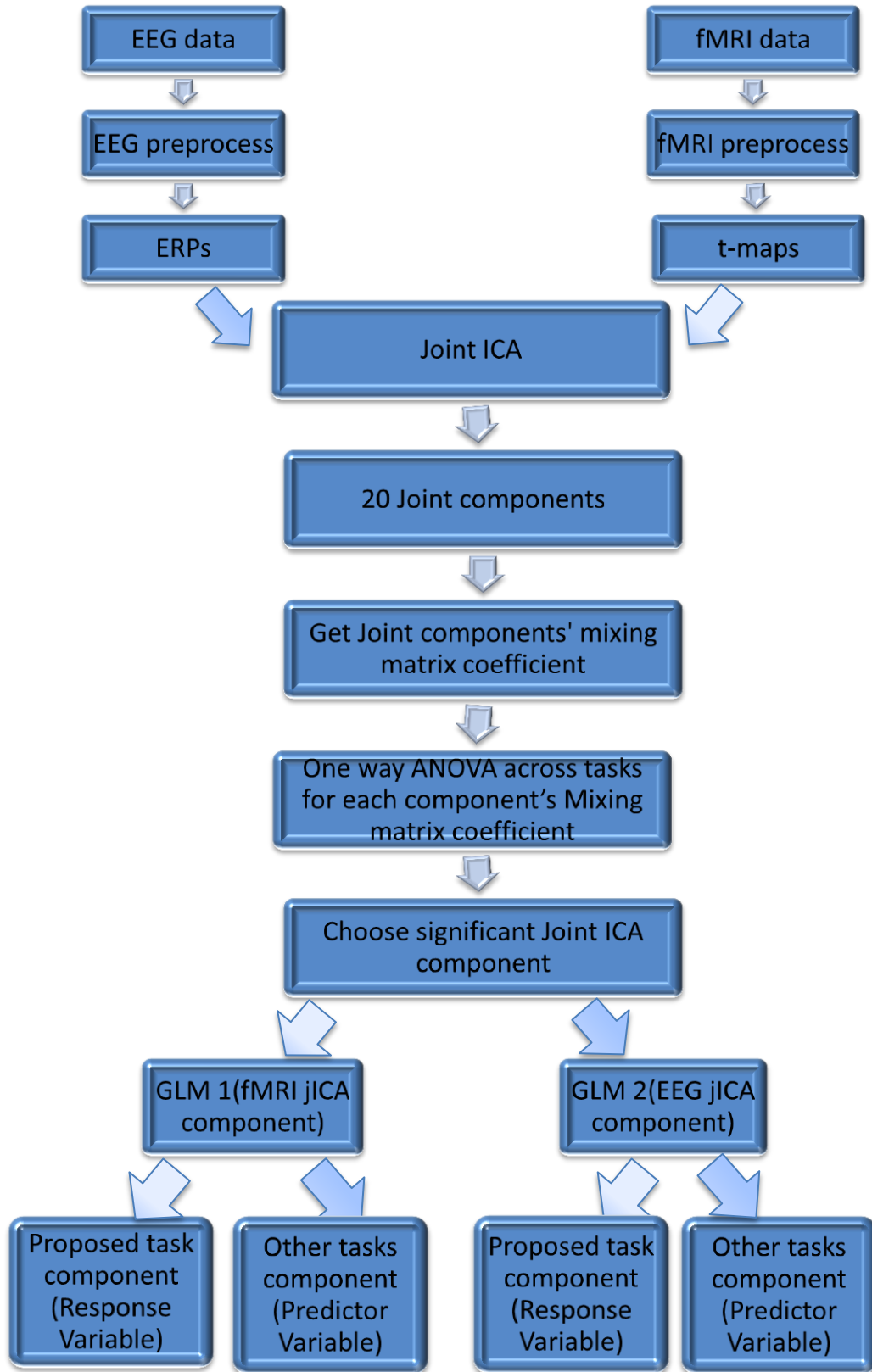


Figure 26: Joint ICA Schematic

Based on previous reports on the number of independent components in fMRI [31], we chose 20 as the number of jICA components. In order to find the joint component which significantly differed across the tasks, we performed one way-ANOVA across tasks for each of the 20 jICA components. The jICA component which most significantly differed across tasks was selected and input to two general linear models: one involving the fMRI jICA component and another one involving the EEG jICA component. For both models, the jICA component obtained from the proposed task (Temporal Task with Uncertainty - Mixed Reward and Costs) was used as the response variable and those obtained from all other tasks (except the control task, as it was subtracted out from the t-maps and ERPs of other tasks) were used as the predictor variables.

4.3 Results

In this section we refer to “Temporal Task with Uncertainty - Mixed Reward and Costs” as DDPROBMIX and all other tasks except the control task as OTHER TASKS. For the jICA component which was most significantly different between tasks (p-value=0.0043), we found that the mixing coefficients for DDPROBMIX were an exact linear combination of the mixing coefficients for OTHER TASKS. We also found that both EEG and fMRI jICA components for DDPROBMIX can be predicted from corresponding EEG and fMRI jICA components obtained from the simpler OTHER TASKS using a general linear model (GLM). For the fMRI GLM, the R^2 statistic and model p-value was found to be 0.3803 and 0 respectively. Figure.27 shows the fMRI jICA component for DDPROBMIX as well as that predicted by a linear combination of

fMRI jICA components from OTHER TASKS and the overlap between the two. For the EEG GLM, the R^2 statistic and model p-value for all the electrodes are shown in Table.2. Figure.28 shows the EEG jICA component for DDPROBMIX as well as that predicted by a linear combination of EEG jICA components from OTHER TASKS for all electrodes. The means across electrodes for the EEG jICA component obtained from DDPROBMIX and that for the component predicted from the EEG jICA components from OTHER TASKS using the EEG GLM is shown in Figure 29. The correlation between them was significant ($R= 0.6430$, $p=7.727\times 10^{-25}$). Figure 30 shows the snapshots from the video created by FIT toolbox for the EEG and fMRI jICA components for DDPROBMIX. This essentially demonstrates the high spatio-temporal resolution with which the dynamic of brain activity can be determined immediately preceding and following decision making.

Table 2: Showing the R2 statistic and model p-value for all the EEG Channels

Channel number	EEG Channel name	p-value	R^2 statistic
1	Fp1	8.04×10^{-19}	0.392292627
2	Fp2	3.65×10^{-11}	0.265451827
3	F3	6.04×10^{-14}	0.314700166
4	F4	3.56×10^{-6}	0.165389983
5	C3	3.97×10^{-24}	0.466071063
6	C4	5.80×10^{-13}	0.297768555
7	P3	7.30×10^{-5}	0.135708218
8	P4	6.65×10^{-7}	0.181145934
9	O1	2.78×10^{-11}	0.26763998
10	O2	7.10×10^{-18}	0.378023825
11	F7	8.97×10^{-14}	0.31178069
12	F8	0.000617639	0.113471504
13	T7	4.91×10^{-7}	0.183954138
14	T8	4.91×10^{-7}	0.183954138
15	P7	3.11×10^{-7}	0.188147423
16	P8	1.46×10^{-24}	0.471693758

17	Fz	9.47×10^{-9}	0.21917687
18	Cz	7.87×10^{-17}	0.361851077
19	Pz	0.259845785	0.038593311
20	Oz	2.74×10^{-15}	0.337113253
21	FC1	1.04×10^{-10}	0.257035755
22	FC2	2.73×10^{-7}	0.189332023
23	CP1	1.50×10^{-9}	0.234933785
24	CP2	1.62×10^{-7}	0.194073253
25	FC5	8.82×10^{-15}	0.32874687
26	FC6	1.17×10^{-8}	0.217324418
27	CP5	7.89×10^{-10}	0.24030568
28	CP6	0.000164621	0.127382183
29	TP9	1.08×10^{-5}	0.154699903
30	TP10	4.13×10^{-14}	0.317500575
31	POz	0.117322243	0.050610997
32	F1	1.91×10^{-9}	0.232862933
33	F2	4.07×10^{-8}	0.206414723
34	C1	2.03×10^{-17}	0.371025458
35	C2	8.35×10^{-10}	0.23983399
36	P1	1.01×10^{-5}	0.155377163
37	P2	0.001394193	0.104643112
38	AF3	3.86×10^{-16}	0.350909055
39	AF4	4.70×10^{-10}	0.244620149
40	FC3	3.01×10^{-14}	0.319835729
41	FC4	5.10×10^{-7}	0.18359034
42	CP3	3.75×10^{-15}	0.334890329
43	CP4	5.62×10^{-8}	0.203563535
44	PO3	1.66×10^{-6}	0.172592666
45	PO4	5.11×10^{-14}	0.315939482
46	F5	7.59×10^{-14}	0.313019036
47	F6	6.52×10^{-6}	0.15958191
48	C5	2.53×10^{-20}	0.414208043
49	C6	1.68×10^{-6}	0.172492049
50	P5	0.00048934	0.115957402
51	P6	2.13×10^{-19}	0.400821811
52	AF7	5.01×10^{-21}	0.424188501
53	AF8	9.28×10^{-7}	0.178051944
54	FT7	7.38×10^{-12}	0.278125751
55	FT8	6.10×10^{-6}	0.160234663

56	TP7	0.000812489	0.110522569
57	TP8	3.77×10^{-12}	0.283370076
58	PO7	0.000246049	0.123205356
59	PO8	8.19×10^{-34}	0.577572875
60	FT9	6.48×10^{-11}	0.260832682
61	FT10	1.79×10^{-08}	0.21362748
62	Fpz	7.14×10^{-15}	0.330271532
63	CPz	5.72×10^{-11}	0.261836218
64	FCz	6.41×10^{-13}	0.297007046

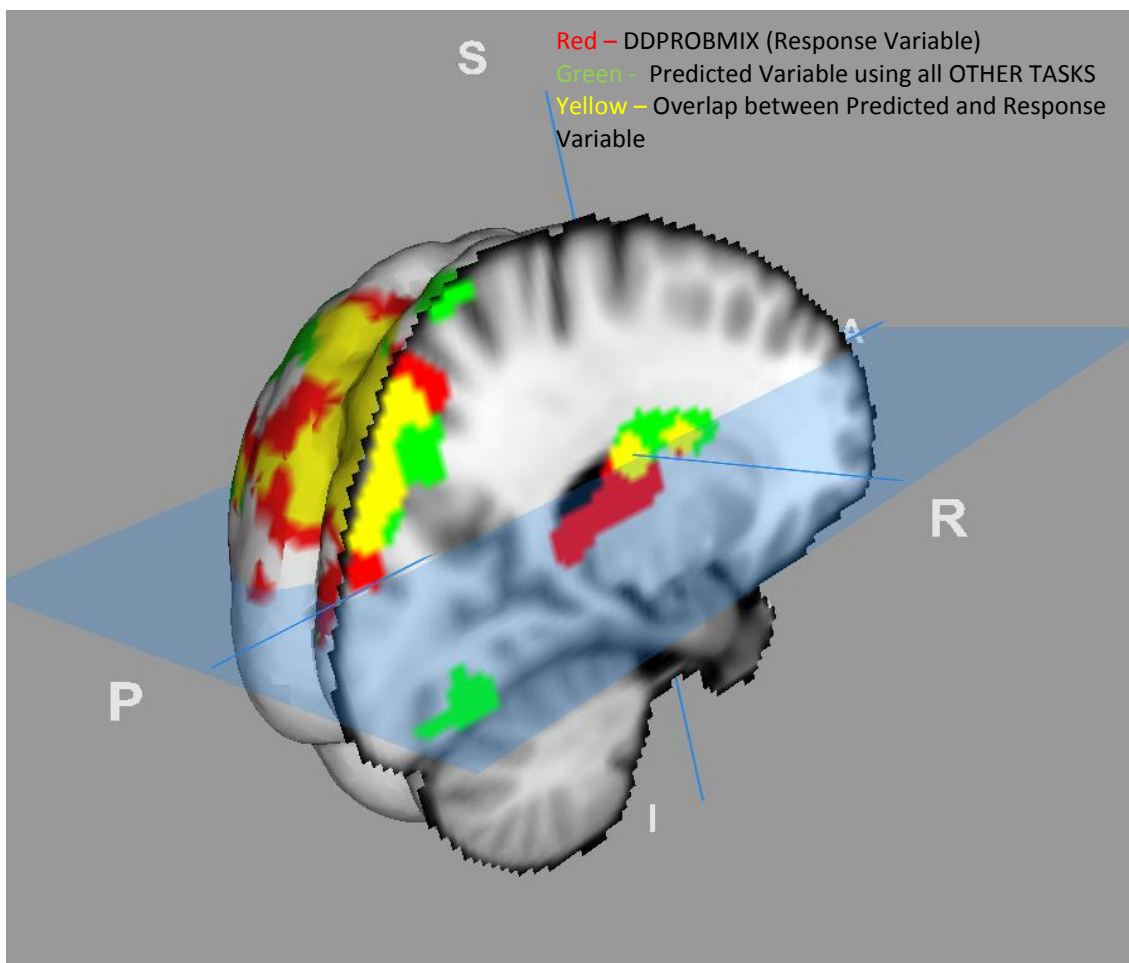


Figure 27: fMRI DDPROBMIX jICA Component (in Red) and fMRI predicted component using jICA components from OTHER TASKS (in Green). The Overlap between the two (Predicted component using OTHER TASKS and DDPROBMIX) is shown in Yellow

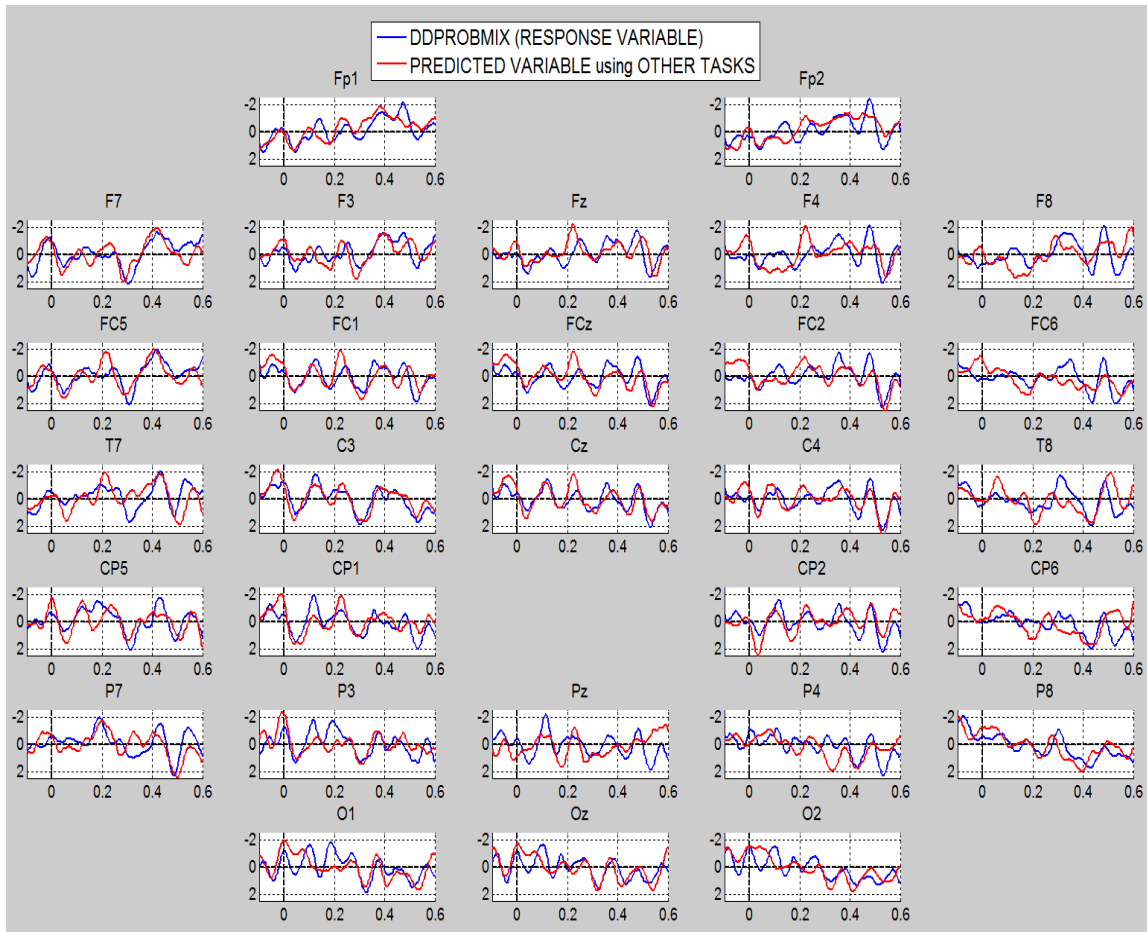


Figure 28: EEG DDPROMIX jICA Component (in Blue) and the predicted EEG component using jICA components from OTHER TASKS (in Red).

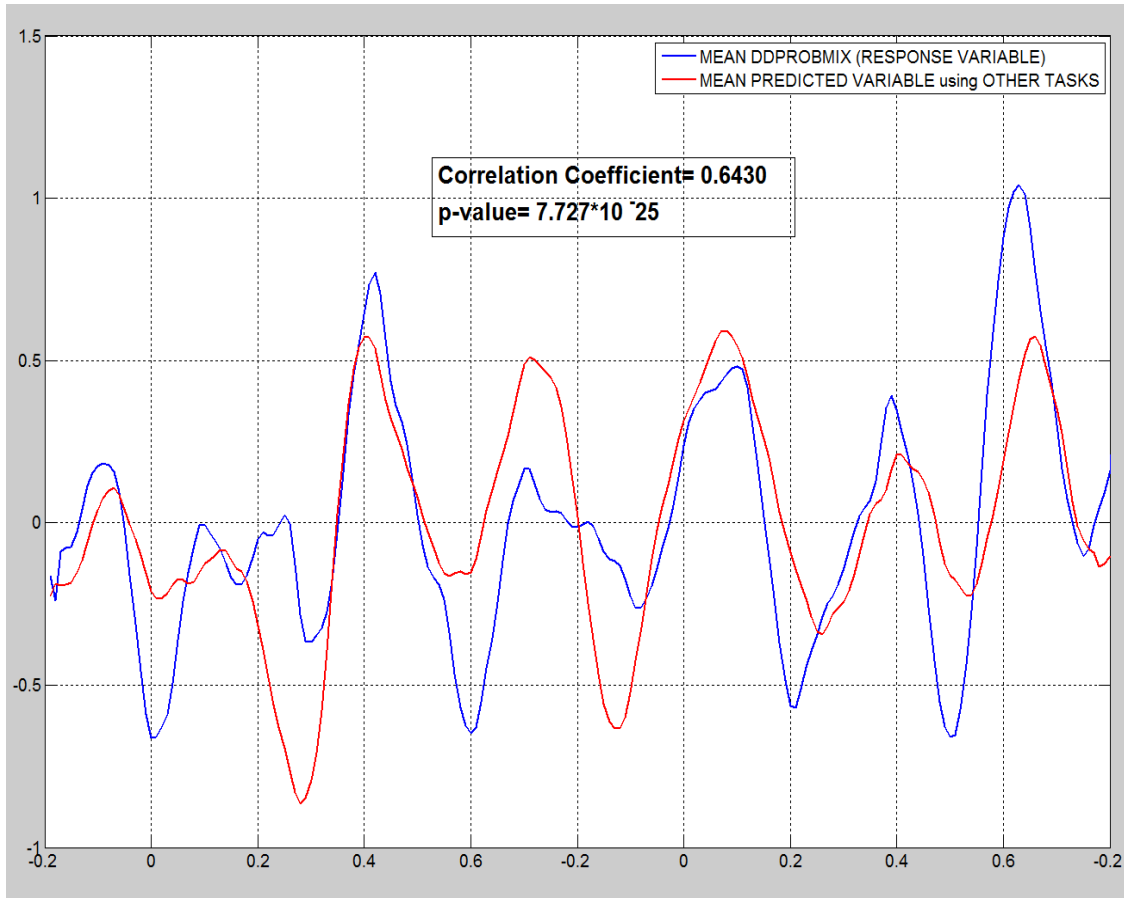
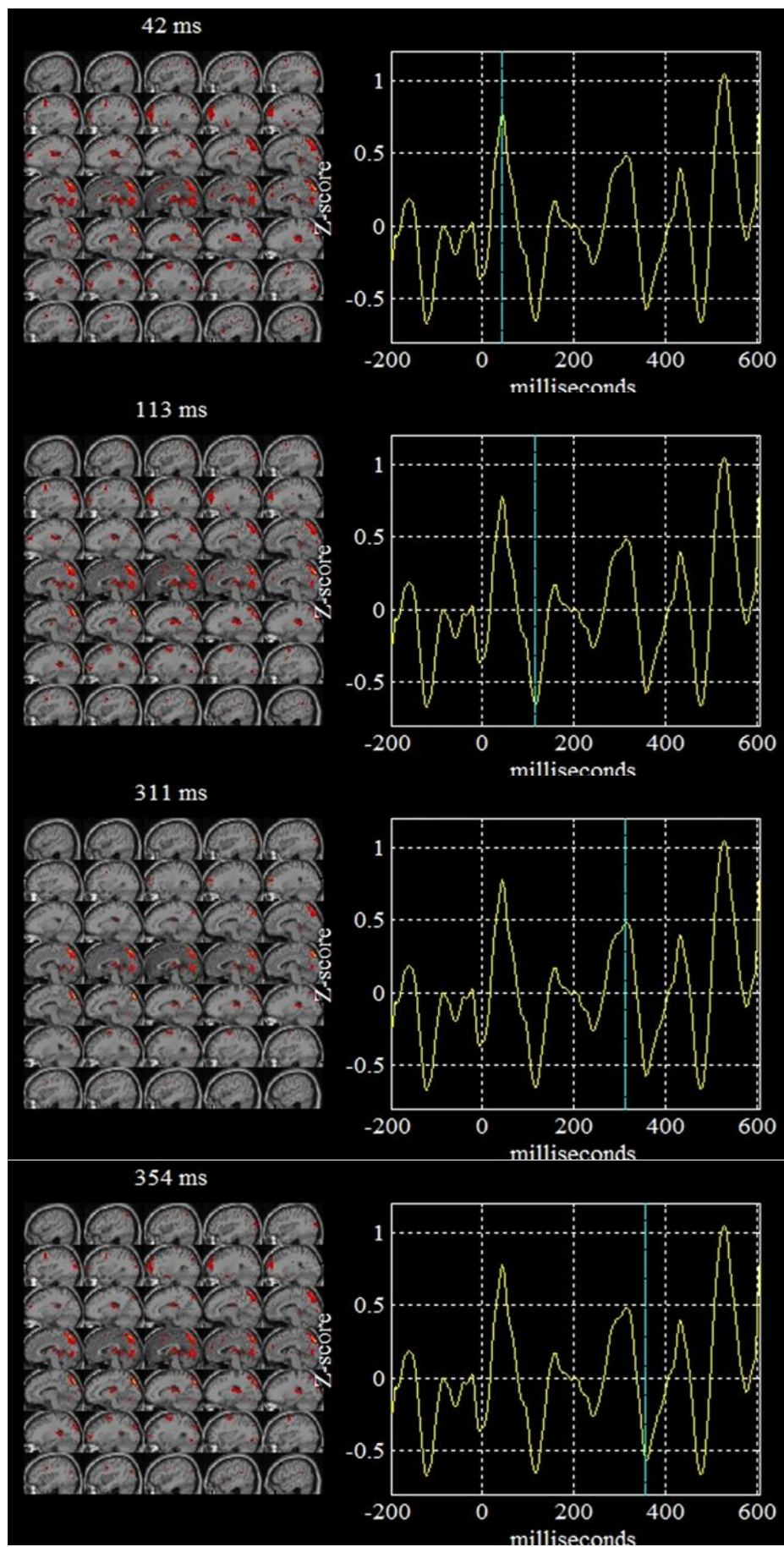


Figure 29: The means across electrodes for the EEG jICA component obtained from DDPROBMIX (Blue) and that for the component predicted from the EEG jICA components from OTHER TASKS



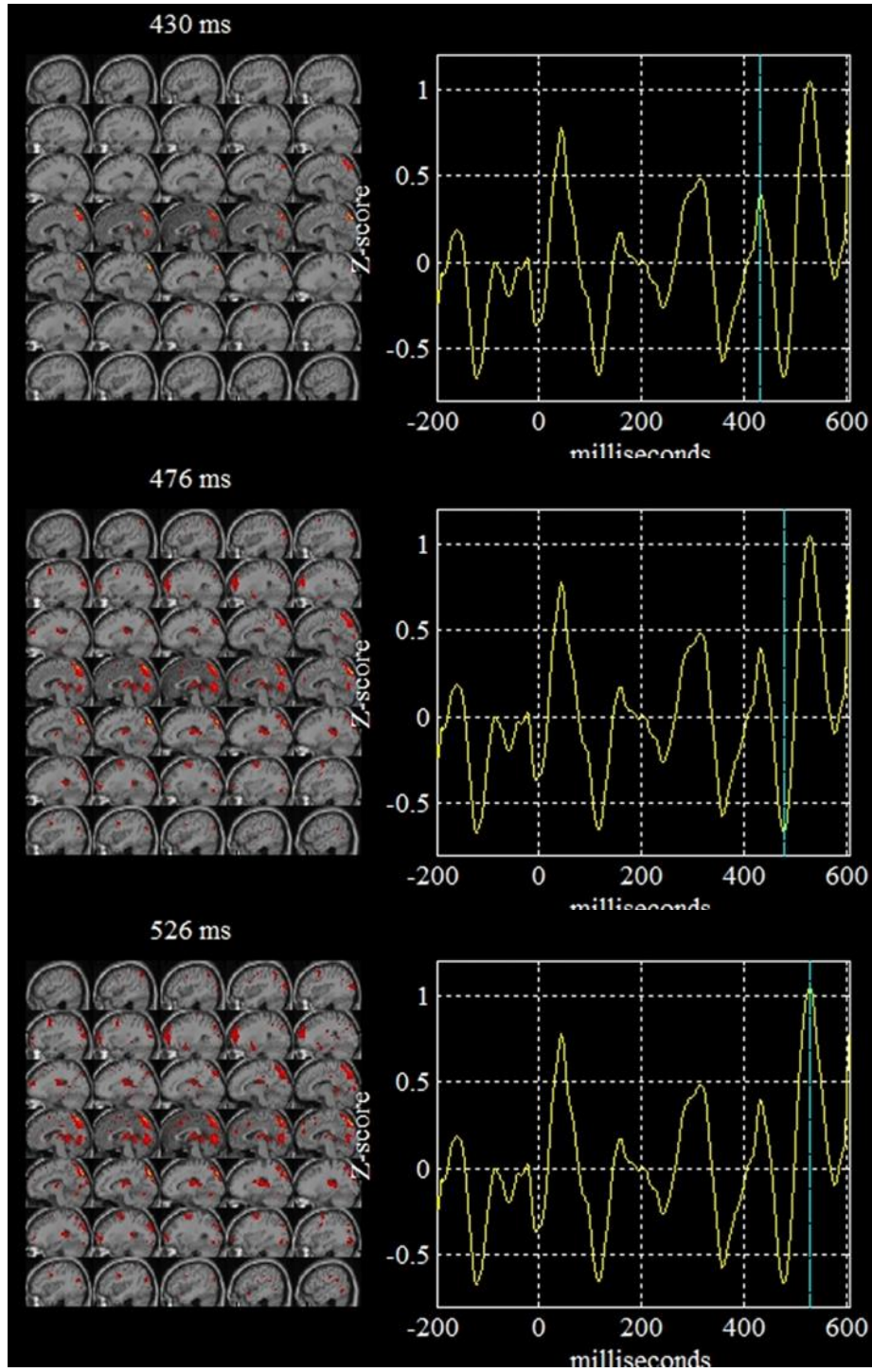


Figure 30: Snapshots from the video created by FIT toolbox for the EEG and fMRI jICA components for DDPROBMIX

4.4 Discussion

The above work supports the feasibility of changing task parameters in temporal decision tasks, taking into consideration the cost-reward trade-offs (across varying probabilities) more typical of real-world decision making. These data indicate that the additional complexity introduced by our task distinguishes itself from the control task in salient ways. As our task more closely models real-world decision making, these differences may more accurately depict the underlying neural processing of temporal decision-making that occurs naturally. We believe that this work provides a strong foundation for further developing and validating temporal decision tasks. Additionally, the development of increased complexity in intertemporal choice tasks provides a mechanism to establish behavioral effects and allows researchers to capture underlying attentional and neurological processes in self-control and decision making, as well as providing parameters that will allow us to more accurately model individual-level algorithms underlying choice behavior.

The proposed task activated the reward and decision making circuits, most notably ventral striatum, Caudate, insula, medial/lateral parietal cortex. Also, the temporal dynamics revealed multiple activations of this circuit, showing reward-related positivity and negativity, both prior to and after the decision making point. More areas in the proposed task were activated as compared to standard tasks reported before [14, 32]. Additionally, the fMRI activation maps (not shown here) had some spatial similarities with the jICA fMRI component that was most significantly different from the control task (shown in Figure.27), though the former does not provide the fast temporal dynamics information that the latter does. Also, the jICA component of the proposed task was most significantly different from the other tasks including the control task ($p\text{-value}=0.0411$).

This study provides a framework for investigating decision-making in the brain with high spatio-temporal resolution. Specifically, it validates the superiority of the proposed temporal decision task, allowing us to more accurately model real world decision-making.

4.5 Bibliography

- [1] G. Chapman, "Time discounting of health outcomes. In George Loewenstein, Daniel Read, & Roy Baumeister," in *Time and Decision: Economic & Psychology Perspectives on Intertemporal Choice*, New York, Russell Sage Foundation, 2003, pp. 395-418.
- [2] B. Jones and H. Rachlin, "Social discounting," *Psychological Science*, vol. 17, no. 4, pp. 283-286, 2006.
- [3] G. Loewenstein and R. Thaler, "Intertemporal choice," *Journal of Economic Perspectives*, vol. 3, no. 4, pp. 181-193, 1989.
- [4] R. Carson and B. Tran, "Discounting behavior and environmental decisions," *Journal of Neuroscience, Psychology, and Economics*, vol. 2, no. 2, pp. 112-130, 2009.
- [5] R. F. Baumeister, K. Vohs and D. Tice, "The strength model of self-control," *Current Directions in Psychological Science*, vol. 16, no. 6, pp. 351-355, 2007.
- [6] E. Weber and E. Johnson, "Mindful judgment and decision making," *Annual Review of Psychology*, vol. 60, pp. 53-85, 2009.
- [7] C. Davis, K. Patte, C. Curtis and C. Reid, "Immediate pleasures and future consequences. A neuropsychological study of binge eating and obesity," *Appetite*, vol. 54, no. 1, pp. 208-213, 2010.
- [8] G. Dom, P. D'haene, W. Hilstijn and B. Sabbe, "Impulsivity in abstinent early- and late-onset alcoholics: differences in self-report measures and a discounting task," *Addiction*, vol. 101, pp. 50-59, 2006.
- [9] K. N. Kirby and N. M. Petry, "Heroin and cocaine abusers have higher discount rates for delay rewards than alcoholics and non-drug-using controls," *Addiction*, vol. 99, pp. 461-471, 2004.
- [10] D. Read, "Intertemporal choice," in *Blackwell handbook of judgment and decision making*, D. J. Koehler and N. Harvey, Eds., Malden, MA: Wiley-Blackwell, 2007, pp. 424-443.
- [11] L. Green and J. Myerson, "A discounting framework for choice with delay and probabilistic rewards," *Psychological Bulletin*, vol. 130, pp. 769-792, 2004.
- [12] K. K. Kim and G. Zauberman, "Perception of anticipatory time in temporal

- discounting," *Journal of Neuroscience, Psychology, and Economics*, vol. 2, pp. 91 - 101, 2009.
- [13] G. Zauberman, B. K. Kim, S. A. Malkoc and J. R. Bettman, "Discounting time and time discounting: Subjective time perception and intertemporal preferences," *Journal of Marketing Research*, vol. 46, pp. 543-556, 2009.
 - [14] B. J. Weber and S. A. Huettel, "The neural substrates of probabilistic and intertemporal decision making," *Brain Research*, vol. 1234, pp. 104-115, 2008.
 - [15] S. J. Estle, I. Green, J. Myerson and D. D. Holt, "Differential effects of amount and temporal and probability discounting of gains and losses," *Memory & Cognition*, vol. 34, pp. 914-928, 2006.
 - [16] G. J. Madden and W. K. Bickel, "Impulsivity: The Behavioral and Neurological Science of Discounting," *American Psychological Association*, 2010.
 - [17] A. Tversky and D. Kahneman, "The framing of decisions and the psychology of choice," *Science*, vol. 211, pp. 453-458, 1981.
 - [18] J. Murphy, R. Vuchinich and C. Simpson, "Delayed reward and cost discounting," *Psychological Record*, vol. 51, p. 571–588, 2001.
 - [19] C. AS and C. Holroyd, "High temporal discounters overvalue immediate rewards rather than undervalue future rewards: An event-related brain potential study," *Cogn Affect Behav Neurosci*, vol. 13, no. 1, pp. 36-45, 2012.
 - [20] M. Blackburn, L. Mason, M. Hoeksma, E. Zandstra and W. El-Deredy, "Delay discounting as emotional processing: An electrophysiological study," *Cogn Emot*, vol. 26, no. 8, pp. 1459-1474, 2012.
 - [21] M. M. Walsh and J. R. Anderson, "Learning from experience: Event-related potential correlates of reward processing, neural adaptation, and behavioral choice," *Neuroscience and Biobehavioral Reviews*, vol. 36, p. 1870–1884, 2012.
 - [22] M. Rosa, J. Daunizeau and K. Friston, "EEG-fMRI integration: a critical review of biophysical modeling and data analysis approaches," *J Integr Neurosci*, vol. 9, no. 4, pp. 453-476, 2010.
 - [23] B. Edwards, V. Calhoun and K. Kiehl, "Joint ICA of ERP and fMRI during error-monitoring," *Neuroimage*, vol. 59, no. 2, pp. 1896-1903, 2012.
 - [24] A. M. Franco-Watkins, T. C. Rickard and H. Pashler, "Taxing executive processes does not necessarily increase impulsive decision making," *Experimental Psychology*, vol. 57, pp. 193-201, 2010.
 - [25] D. Feinberg, S. Moeller, S. Smith, E. Auerbach, S. Ramanna, M. Glasser, K. L. Miller, K. Ugurbil and E. Yacoub, "Multiplexed echo planar imaging for sub-second whole brain fMRI and fast diffusion imaging," *PLoS One*, vol. 5, no. 12, 2010.
 - [26] K. Friston, A. Holmes, K. Worsley, J. Poline, C. Frith and J. Frackowiak, "Statistical parametric maps in functional imaging: A general linear approach," *Human Brain Mapping*, vol. 2, no. 4, pp. 189-210, 1995.
 - [27] P. Allen, O. Josephs and R. Turner, "A method for removing imaging artifact from continuous EEG recorded during functional MRI," *Neuroimage*, vol. 12, no. 2, pp. 230-239, 2000.
 - [28] V. Calhoun, T. Adali, G. Pearson and K. Kiehl, "Neuronal chronometry of target

- detection: Fusion of hemodynamic and event-related potential data," *NeuroImage*, vol. 30, p. 544–553, 2006.
- [29] V. Calhoun, J. Liu and T. Adali, "A review of group ICA for fMRI data and ICA for joint inference of imaging, genetic, and ERP data," *NeuroImage*, vol. 45, pp. 163-172, 2009.
- [30] V. D. Calhoun, "Fusion ICA Toolbox (FIT)," [Online]. Available: <http://mialab.mrn.org/software/fit/>.
- [31] C. Rosazza, L. Minati, F. Ghielmetti, M. Mandelli and M. Bruzzone, "Functional Connectivity during Resting-State Functional MR Imaging: Study of the Correspondence between Independent Component Analysis and Region-of-Interest-Based Methods," *AJNR Am J Neuroradiol.*, vol. 33, no. 1, pp. 180-187, 2012.
- [32] M. Wittman, K. Lovero, S. D. Lane and M. P. Paulus, "Now or later? Striatum and insula activation to immediate versus delayed rewards," *Journal of Neuroscience, Psychology, and Economics*, vol. 3, pp. 15-26, 2010.
- [33] I. Yanovotzky, "Sensation seeking and alcohol use by college students: Examining multiple pathways to effects," *Journal of Health Communication*, vol. 11, pp. 269-280, 2006.
- [34] M. L. Cooper, M. R. Frone, M. Russell and P. Mudat, "Drinking to regulate positive and negative emotions: A motivation model of alcohol use," *Journal of Personality and Social Psychology*, vol. 69, pp. 990-1005, 1995.

Chapter 5

Investigation of the neural basis of the default mode network using parallel independent component analysis of simultaneous EEG/fMRI data

Abstract

Electroencephalography (EEG) has high temporal and low spatial resolution, but the opposite is true for fMRI. Therefore, combining EEG and fMRI data provides complementary measures of neural electrical activity at high temporal resolution and hemodynamics at high spatial resolution. Previous work using simultaneous EEG/fMRI has shown that the slow temporal dynamics of resting state networks (RSNs) obtained from fMRI are correlated with smoothed and down sampled versions of various EEG features such as microstates and band-limited power and power envelopes. On the other hand, EEG microstates have been shown to be scale-free, and there is speculation that corresponding resting state fluctuations may exist not only in the low frequency, but also high frequency, which would make resting fluctuations obtained from fMRI more meaningful to typically occurring fast neuronal processes. In this study, we test this critical hypothesis using an integrated framework involving simultaneous EEG/fMRI acquisition, fast fMRI sampling (TR=600ms and TR=200ms) using multiband EPI (MB EPI), and EEG/fMRI fusion using parallel independent component analysis (pICA) which does not require the down sampling of EEG to fMRI temporal resolution. Our results demonstrate that with faster sampling, high frequency electrical correlates of the default mode network indicating its operation at sub-second time scale can be observed, thus providing it a sounder neurophysiological basis.

5.1 Introduction

Functional magnetic resonance imaging (fMRI) reveals spontaneous, large-amplitude, low-frequency (< 0.1 Hz) fluctuations of a large number of anatomically separate brain areas that are temporally correlated and functionally linked to each other at rest and these brain areas are called “resting state networks” (RSNs) [1] [2] [3] [4] [5] [6] [7] [8] [9]. It has been observed that task related response accounts for less than 5% of cerebral metabolism, whereas most of cerebral metabolism corresponds to resting state activity [10]. Multiple studies in the previous decade have shown that the alterations in resting state brain connectivity can be associated with neurological or psychiatric diseases [11]. Therefore, RSNs have become very popular method for assessing brain function in patient populations because it is possible to perform fMRI without stimulation which is helpful for such subjects who can have difficulties while performing tasks [12]

Even though blood oxygenation level dependent (BOLD) fMRI has been used to detect spatially consistent RSNs across subjects it is still unclear if the correlated resting state activity has a neuronal origin or it is due to low frequency physiological or scanner related artifacts [13] [14]. BOLD fMRI is an indirect measure of neural activity [15] and it is unclear whether correlated resting state activity observed from very slow fluctuations of the order of 10s of seconds are related to the neuronal dynamics which occur in the millisecond scale. Even if they RSNs were to be related to fast neuronal activity the underlying physiological mechanisms establishing such link are unknown.

Contrary to fMRI, electroencephalogram (EEG) is a direct measure of the electrical activity in the brain measured at its scalp. It is the sum of all the synchronous activity of all the neurons in the area below the electrode on the scalp [16] [17] [18]. There has been

some evidence showing that spontaneous resting state EEG activity fluctuates coherently and they are macroscopically organized across the brain [19]. Though EEG has very high temporal resolution for measuring the resting state neuronal activity, its spatial resolution is very poor and hence limits our ability to make physiologically meaningful inferences about the neural basis of RSNs observed from fMRI.

In order to noninvasively understand the neural basis of RSNs observed from fMRI in humans, we need to combine EEG and fMRI signals such that we get both high spatial and temporal resolution of the underlying neuronal activity [20] [21] [22] [23]. There have been several studies related to simultaneous EEG and fMRI signals which shows that the EEG power envelope at specific frequency bands correlates with RSNs [24] [25] [26] [27] [28]. However, EEG is made up of wide frequency spectrum [29] [30], thus the correlation between neuronal activity only at specific frequency to the BOLD RSNs does not make sense [31] and it has been shown that the time course of RSNs can be associated to EEG activity at more than one frequency band [32]. There are two fundamental issues regarding the approaches described above. First, the EEG power envelope corresponding to various EEG frequency bands still represents a low frequency amplitude modulated signal. Second, in order to match the temporal resolution of EEG to that of fMRI, these studies downsampled EEG data to that of fMRI temporal resolutions. These two factors make it impossible to assess whether the correlations between EEG power envelope and BOLD RSNs have a neural basis in millisecond-scale fast neuronal dynamics. However, they do point to the fact that RSNs have an electrical basis and cannot be purely based on BOLD-based physiological artifacts.

Recently, EEG microstates have been shown to be scale-free and have been proposed as potential electrophysiological correlates of spontaneous BOLD activity [33] [34]. There is a speculation that corresponding resting state fluctuations may exist not only in the low frequency, but also high frequency, which would make resting fluctuations obtained from fMRI more meaningful to typically occurring fast neuronal processes. However, the hypothesis that BOLD RSNs have a neuronal basis related to high frequency electrical activity has never been directly tested. Therefore, in this study, we tested this critical hypothesis for the Default mode network (DMN), which is most commonly found RSN [35] [2] [3] [4]. We used parallel Independent Component Analysis (pICA) of simultaneously acquired EEG-fMRI data during resting state for fusing data from both modalities without sacrificing the native resolutions of either modality. In addition, we acquired whole brain fMRI data with TRs as short as 200 ms using multiband EPI sequence [36] to test the hypothesis that faster sampling would enable us to better detect the high frequency electrical correlates of the DMN. ICA is one of the multivariate methods which considers both spatial and temporal characteristics to identify RSNs and does not require any a priori seed region [37] [5]. Here we applied ICA separately to EEG and fMRI data, to get statistically independent time courses (tICA) and statistically independent spatial maps (sICA), respectively. pICA is a second level analysis which uses first level results to recover maps from fMRI and time courses from EGG and match these components across the modalities to achieve the multimodal integration for simultaneous resting state data.

5.2 Materials And Methods

5.2.1 Subjects and Tasks

Six adult subjects with no history of neurological or cardiological disorders participated in this simultaneous EEG-fMRI resting state study. The study was approved by the Institutional Review Board at Auburn University and informed consent was obtained prior to the study. The entire study for each subject contained a single session of simultaneous EEG-fMRI recording for resting state Eyes open (EO) and Eyes close (EC) conditions. The subjects were instructed to lie supine, stay awake and not to think of anything in particular inside the scanner with their eyes open or eyes closed. We investigated both EO and EC conditions since the spontaneous EEG activity during these two conditions has been reported to be different [38] [39] , though fMRI-based RSNs have been reported to be quite similar across both conditions in many studies [3] [40] [41] [42] while a few others show differences between BOLD RSNs across the two conditions [43] [44] [45] [46] [47] . Cushions were placed inside the coil to absorb the pressure from the EEG electrodes on the head and to restrict head movement in the coil. Subjects were also provided with earplugs to avoid any harmful effect from the fMRI acoustic noise.

5.2.2 fMRI data acquisition

Resting state fMRI data (one run each, of eyes open and eyes closed) were collected on a 3T Siemens Verio scanner using a 12-channel matrix head coil using (1) single-shot gradient-recalled EPI sequence with 29ms TE, 1000ms TR, 90° flip angle, 64 x 64 x 16 acquisition matrix for six healthy subjects (4 male and 2 female)

- (2) MB-EPI sequence with multiband factor of 8 (MB8) [36] with 30ms TE, 600ms TR, 55° flip angle, 64 x 64 x 16 acquisition matrix for six healthy subjects (3 male and 3 female) and
- (3) MB-EPI sequence with multiband factor of 2 (MB8) [36] with 40 ms TE, 200ms TR, 50° flip angle, 64 x 64 x 16 acquisition matrix for six healthy subjects (3 male and 3 female)

5.2.3 EEG Data Acquisition

For simultaneous EEG-fMRI acquisition, we used MR-compatible 64 channel EEG amplifiers (Brain Products, GmBH, Germany), MR-compatible EEG cap (BrainCap MR, Falk Minow Services, Herrsching–Breitbrunn, Germany) with 63 10-20 system distributed scalp electrodes and ECG electrode. We got 10,000 data points per TR by synchronizing the EEG data acquisition clock to the MRI scanner clock using Brain Products' SyncBox. EEG data were then digitized with a sampling frequency of 5 kHz, 0.5 μ V resolution, with reference to FCz and within a DC-250Hz frequency range. For all the EEG recordings, impedance at electrodes was less than 20 k Ω .

5.2.4 fMRI data pre-processing

Slice timing correction was applied to the EPI and MB-EPI functional MRI data to interpolate the slices so that they all appear to have been collected at the same time for the interleaved sequences. The functional MRI data obtained from each subject was then realigned by taking the first image as the reference for all other scans for motion correction. The images were then resliced and normalized to EPI MNI template and

spatially smoothed with a Gaussian filter with 6mm FWHM using SPM toolbox ([48] <http://www.fil.ion.ucl.ac.uk/spm>). The fMRI signal time courses at each voxel were then detrended followed by removal of white matter and cerebrospinal fluid (CSF) signal using Data Processing Assistant for Resting-State fMRI ([49] DPARSF, <http://www.restfmri.net>) which is based on SPM and Resting-State fMRI Data Analysis Toolkit ([50] REST, <http://www.restfmri.net>).

5.2.5 EEG data pre-processing

Brain Vision Analyzer 2.0 software (Brain Products) was used to perform preprocessing of simultaneously EEG data to reduce MRI gradient artifact, cardioballistic artifact, and ocular artifact arising from the simultaneous EEG–fMRI environment.

- i) For reducing MRI scanning artifacts, we used an artifact template created by averaged artifact subtraction (AAS) method [51] in which the EEG data was segmented and averaged according to the onset of each volume within a sliding window consisting of 41 consecutive volumes, and subtracted from the raw EEG data.
- ii) For reducing cardioballistic artifacts, we used an artifact template created by moving template subtraction approach [52] in which R peaks were detected in the low-pass-filtered ECG signal and used to construct a delayed average artifact template over 21 consecutive heartbeat events in a sliding-window approach, which was subtracted from the original EEG signal.
- iii) The Ocular artifact was removed by applying ICA [53] [54].

The resulting EEG data from the above three steps were then downsampled to 250 Hz, and then re-referenced to FCz. Figure 31 shows the flowchart illustrating the EEG preprocessing steps.

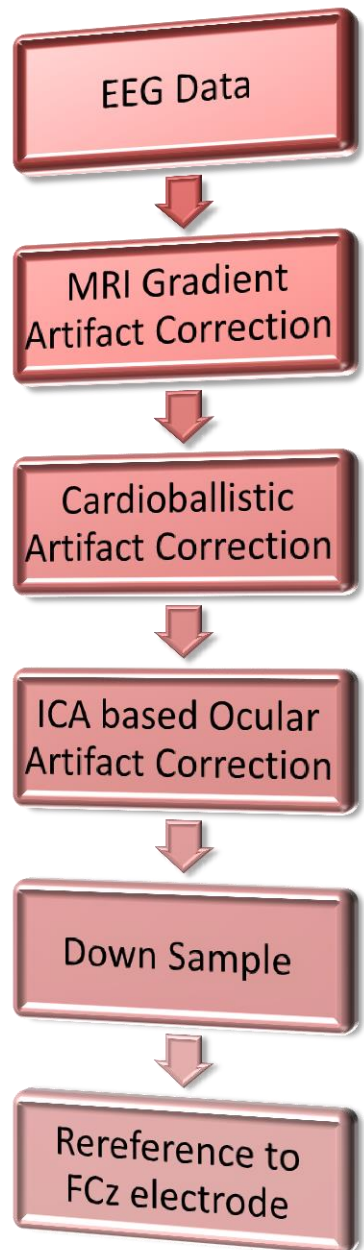


Figure 31: EEG Preprocessing carried out before 1st level EEG

5.2.6 Group spatial ICA of fMRI data (sICA)

The fMRI signal was assumed to be a linear mixture ($x_1(v), x_2(v), \dots, x_N(v)$), of statistically independent hemodynamic source locations ($s_1(v), s_2(v), \dots, s_N(v)$) such that at a given voxel, it contains the weighted mixture of the sources, $a_{j1}s_1(v) + a_{j2}s_2(v) + \dots + a_{jN}s_N(v)$, each of which fluctuates according to its weighted hemodynamic time course, for all j . The weights were multiplied by each source's hemodynamic time course. The ideal observed fMRI signal is given by, $x_j(v) = a_{j1}s_1(v) + a_{j2}s_2(v) + \dots + a_{jN}s_N(v)$. If $x = [x_1(v), x_2(v), \dots, x_N(v)]^T$, $s = [s_1(v), s_2(v), \dots, s_N(v)]^T$ and A the mixing matrix with a_{ij} elements. This can be written in vector-matrix notation as $x = As$ where x represents the ideal samples of the source signals in the brain at location v . We assume that the number of discrete time points acquired with the scanner is very large compared to actual sources in the brain. The sampled fMRI signal is denoted by $y(v) = y_1(v), y_2(v), \dots, y_N(v)$ where the fMRI signal is discretely sampled in space. The fMRI data $y(v)$ was pre-whitened to remove any correlations in the data and reduced via Principal Component Analysis (PCA) by removing non-significant components and retaining only the principal components which contain the major proportion of variance. The principal components were then concatenated across subjects to form group data. The INFOMAX ICA algorithm [55] was then applied to the group data to get the independent components. Individual subject components were computed using the back reconstruction step and the components were scaled to Z-scores to remove the arbitrary units of spatial maps and time courses during back reconstruction step. Finally, the mean, standard deviation and t-maps were

calculated for the group data. The above operations were done using GIFT toolbox [56] [57]. 20 components were generated as in [58] and stored for further analysis.

5.2.7 Group temporal ICA of EEG data (tICA)

The EEG signal was assumed to be a linear mixture ($x_1(t), x_2(t), \dots, x_N(t)$), of statistically independent non-Gaussian source time series ($s_1(t), s_2(t), \dots, s_N(t)$) such that at a given time point, it contains the weighted mixture of the sources ($a_{j1}s_1(t) + a_{j2}s_2(t) + \dots + a_{jN}s_N(t)$), for all j . The weights were multiplied by each source's fixed topography. The ideal observed EEG signal is given by, $x_j(t) = a_{j1}s_1(t) + a_{j2}s_2(t) + \dots + a_{jN}s_N(t)$. If $x = [x_1(t), x_2(t), \dots, x_N(t)]^T$, $s = [s_1(t), s_2(t), \dots, s_N(t)]^T$ and A the mixing matrix with a_{ij} elements, then we can write in vector-matrix notation as $x = As$. x represents the ideal samples of the source signals in the brain at time t . Let us denote the pre-processed EEG signal as $y(j) = [y_1(j), y_2(j), \dots, y_K(j)]^T$ $j=1,2,3,\dots,K$. The preprocessed data $y(j)$ was pre-whitened to remove any correlations in the data and reduced via PCA by removing non-significant components and retaining only the principal components which contain the major proportion of variance. The principal components were then concatenated across subjects to form a group data. The ICA was then applied to the group data to obtain the independent source time-series/components. The above operations were done using EEGIFT toolbox and 20 components were generated as in [59] and stored for further analysis.

5.2.8 Parallel Independent Component Analysis (pICA)

Parallel Independent Component Analysis (pICA) is a second level analysis procedure which combines spatially independent sources obtained from fMRI and temporally independent sources obtained from EEG such that the correlation between the fMRI and EEG mixing matrices is maximized. When ICA is separately applied to EEG and fMRI we assume the acquired signals to be, $X_{EEG} = A_{EEG} S_{EEG}$ and $X_{FMRI} = A_{FMRI} S_{FMRI}$ respectively, where A_{EEG} and A_{FMRI} are the mixing matrices for EEG and fMRI respectively and S_E and S_F are statistically independent non-Gaussian Source time series and spatial maps respectively. In order to determine the unmixed components U_{EEG} and U_{FMRI} , we have to find W_{EEG} and W_{FMRI} such that it approximates inverse of A_{EEG} and A_{FMRI}

$$U_{EEG} = W_{EEG} X_{EEG} = W_{EEG} A_{EEG} S_{EEG}$$

$$U_{FMRI} = W_{FMRI} X_{FMRI} = W_{FMRI} A_{FMRI} S_{FMRI}$$

Using the parallel ICA we maximize the independence using the INFOMAX algorithm [55] which employs gradient ascent for the two modalities and determines the relationship between them. The pICA toolbox [60] was used to find the parallel components as shown in Figure 32.

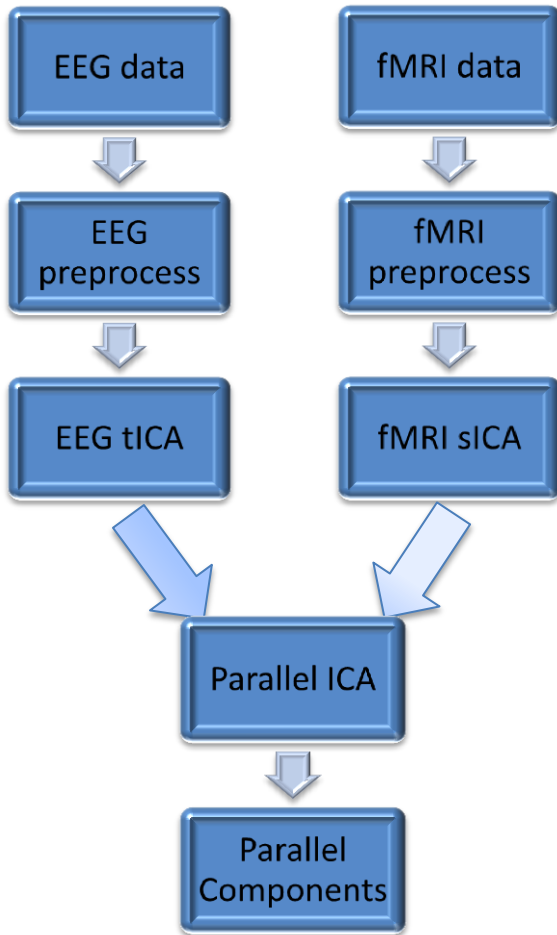


Figure 32: Schematic for Parallel ICA

The inputs to the parallel ICA algorithm are fMRI (Components-by-voxels) and EEG (Components-by-time points) components which are ordered such that first fMRI component corresponds to the first EEG component and so on. In this study, we obtained 20 fMRI and EEG components from first-level ICA analysis. However, we do not know *a priori*, the correspondence between the first-level EEG and fMRI components. Therefore, we cannot input them into the pICA algorithm.

In order to determine the correspondence between the first-level EEG and fMRI components, we made the assumption that if we applied pICA to the matched components then we should get the highest correlation between the mixing matrices of EEG and fMRI. Since we had 20 components from GIFT and 20 components from EEGIFT, so could potentially match the first-level EEG and fMRI components in 400 ways. Since here were interested only with the ICA component corresponding to the DMN, there are 20 ways that the DMN fMRI component can be matched to the 20 first-level EEG components. So, we ran parallel ICA 20 times to see which combination of EEG component with the fMRI-DMN component gave the highest correlation between the mixing matrices. For all 20 iterations, the order of the fMRI components remained the same with the first component being DMN but the orders of EEG components were changed, with the first EEG component being changed from component 1 to component 20 for each iteration, as shown in Figure 33.

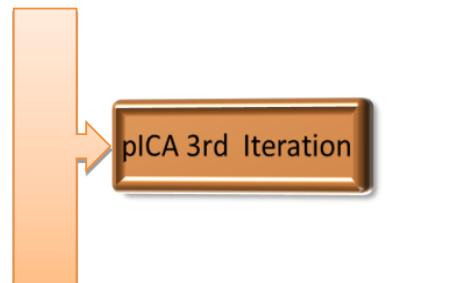
fMRI comp	EEG comp
DMN	EEG 1
fMRI 2	EEG 2
fMRI 3	EEG 3
fMRI 4	EEG 4
...	...
...	...
fMRI 20	EEG 20



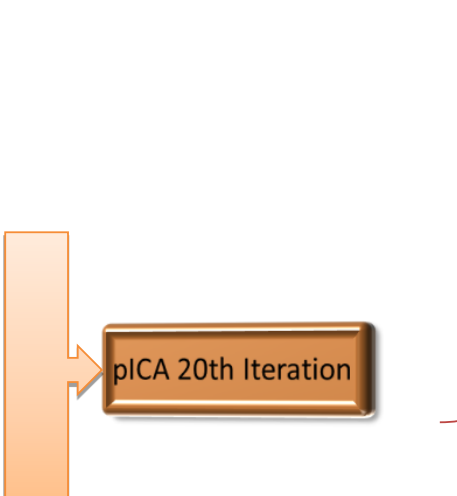
fMRI comp	EEG comp
DMN	EEG 2
fMRI 2	EEG 2
fMRI 3	EEG 3
fMRI 4	EEG 4
...	...
...	...
fMRI 20	EEG 20



fMRI comp	EEG comp
DMN	EEG 3
fMRI 2	EEG 2
fMRI 3	EEG 3
fMRI 4	EEG 4
...	...
...	...
fMRI 20	EEG 20



fMRI comp	EEG comp
DMN	EEG 20
fMRI 2	EEG 2
fMRI 3	EEG 3
fMRI 4	EEG 4
...	...
...	...
fMRI 20	EEG 20



Choose the pICA iteration that has the **highest correlation between the mixing matrices of EEG and fMRI** for the DMN component.

Figure 33: Schematic illustrating parallel ICA iterations for determining matched EEG and fMRI components for the default mode network

5.3 Results

5.3.1 Eyes Closed Condition

As shown in Figure 34, one pICA fMRI component showed the default mode network (DMN) for both EPI and MB-EPI data.

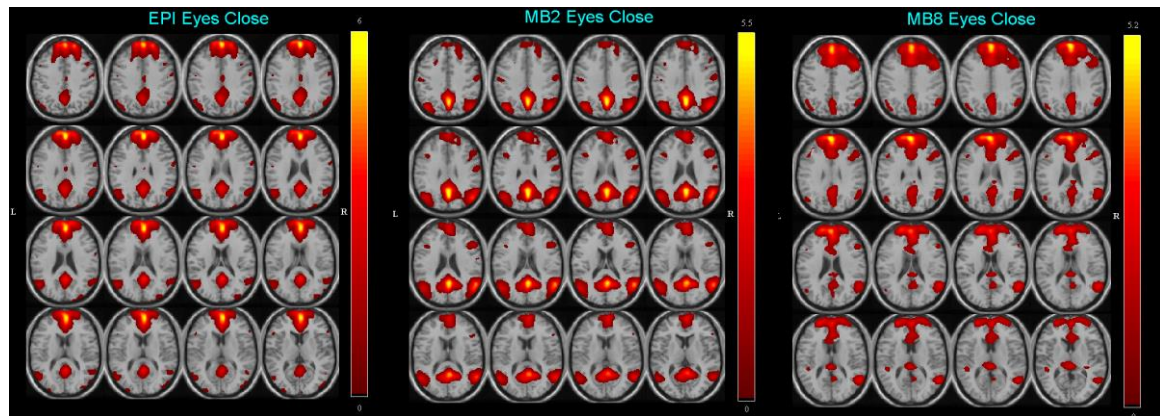


Figure 34: fMRI pICA component corresponding to DMN for EPI, MB2 and MB8 sequences (EC Condition)

Table 3 shows the correlation between EEG and fMRI mixing matrices for regular EPI, MB2 and MB8 data for EC condition. The power of the corresponding EEG pICA component was greater in lower frequency bands for regular EPI data and in high frequency bands for MB2 and MB8 data (Figure 35)

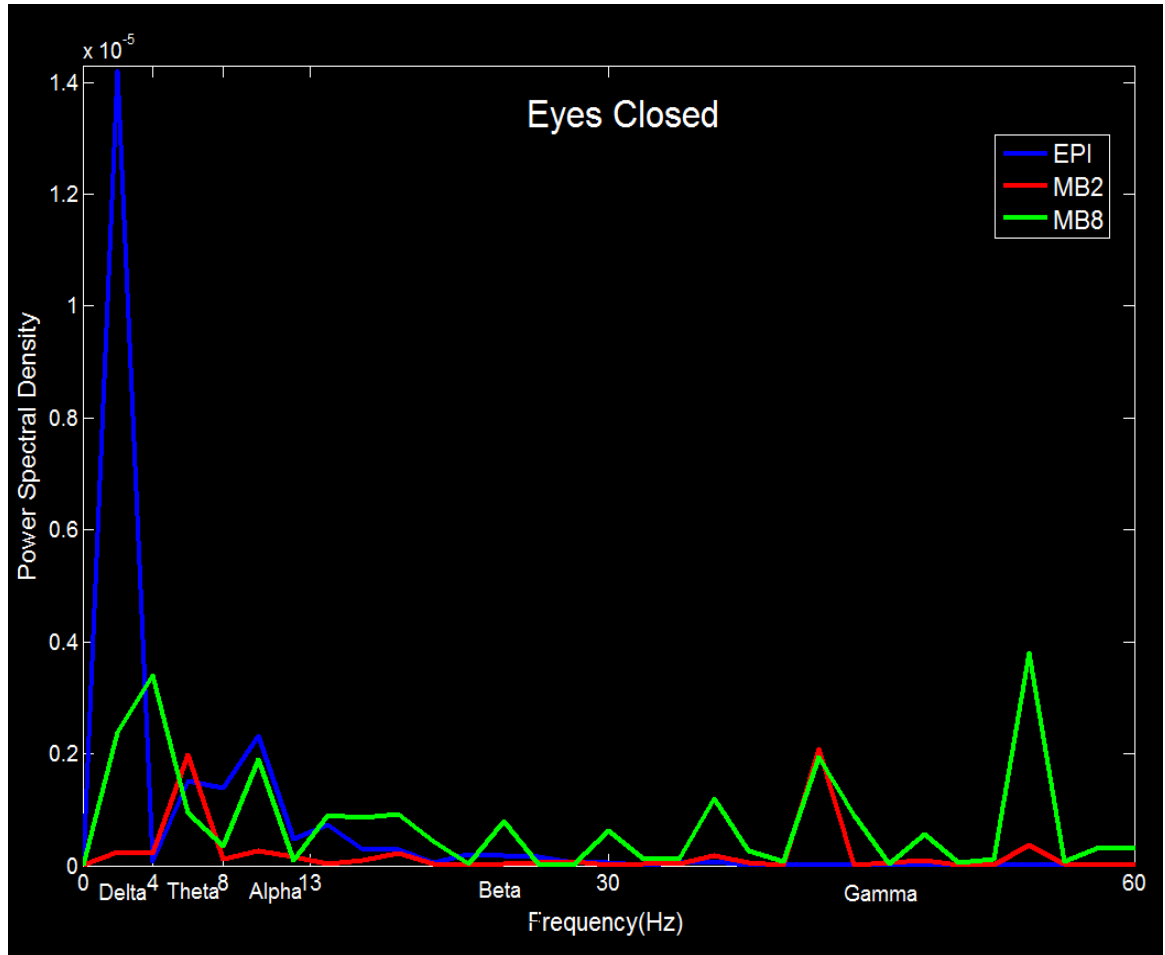


Figure 35: Power in different frequency bands of EEG pICA component of DMN for EPI, MB2 and MB8 data (EC Condition)

5.3.2 Eyes Open Condition

As shown in Figure 36, one pICA fMRI component showed the DMN for both regular EPI and MB-EPI data.

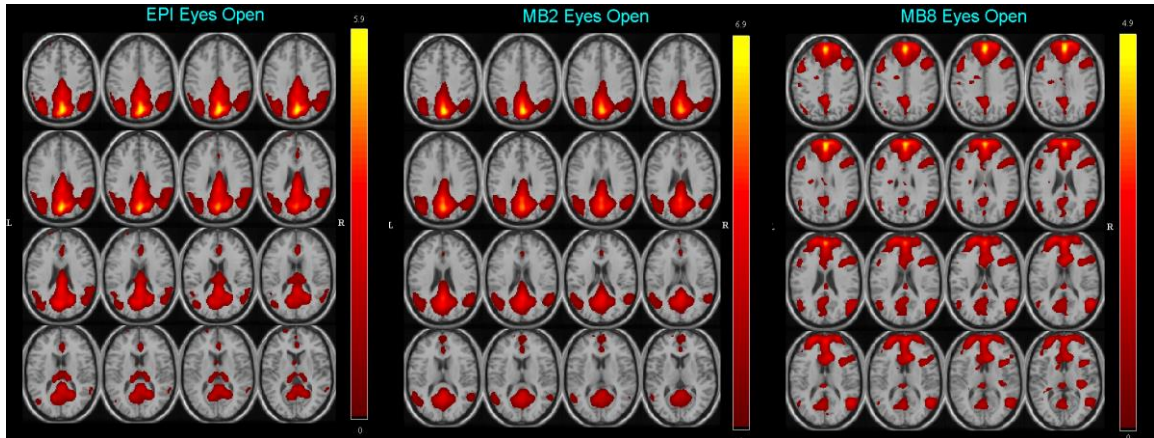


Figure 36: fMRI pICA component corresponding to DMN for EPI, MB2 and MB8 data (EO Condition)

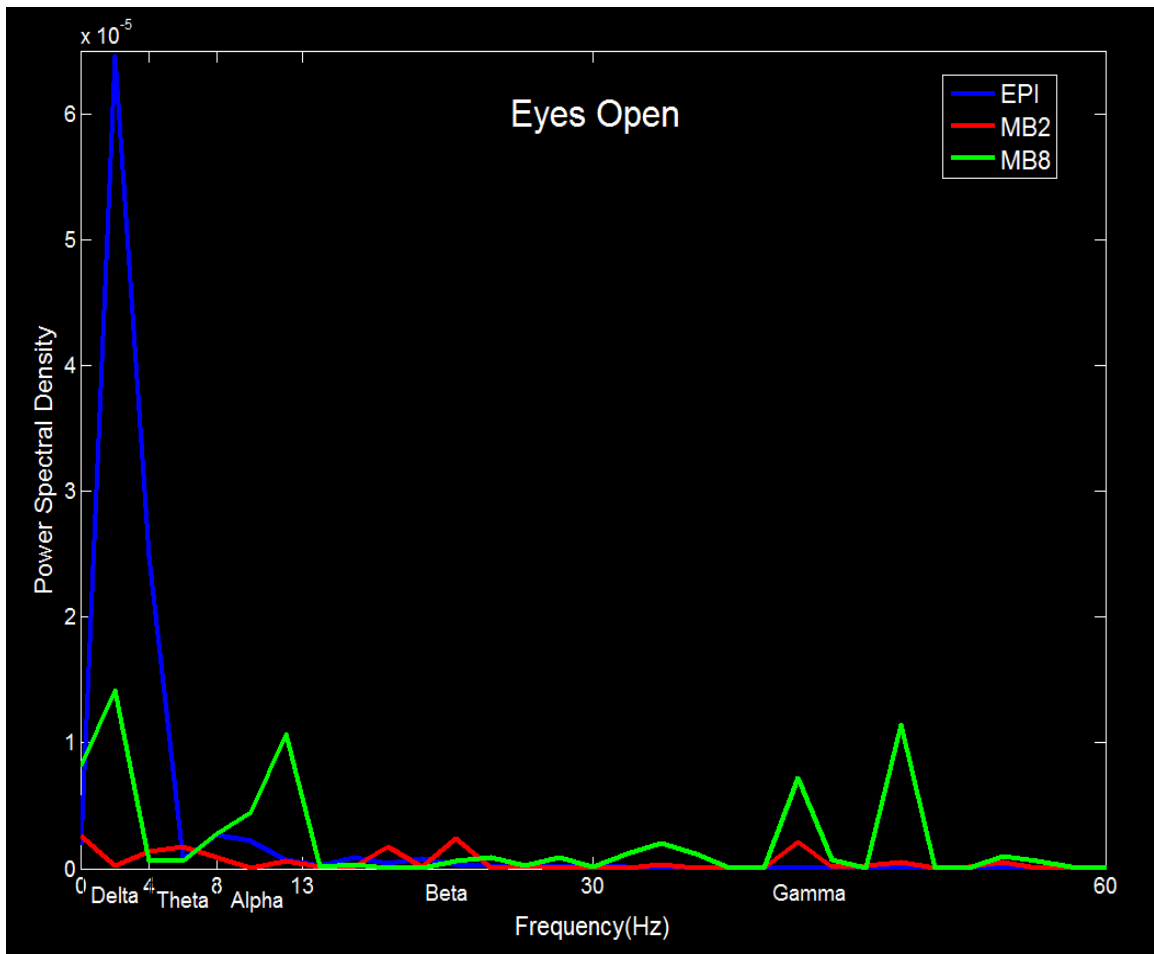


Figure 37: Power in different frequency bands of EEG pICA component of DMN for EPI, MB2 and MB8 data (EO Condition)

Table 1 shows the correlation between EEG and fMRI mixing matrices for EPI, MB2 and MB8 data for the EO condition. The power of the corresponding EEG pICA component was greater in lower frequency bands for regular EPI data and in high frequency bands for MB2 and MB8 data (Figure 37)

Table 3: Correlation and it's corresponding p-value between EEG and fMRI mixing matrices for regular EPI, MB2 and MB8 data

Condition \ Sequence	Regular EPI (TR=1000ms)	MB2 (TR=600ms)	MB8 (TR=200ms)
Eyes Closed	R=0.68178 p-value=0.0009	R=0.82247 p-value=8.563×10 ⁻⁶	R=0.70961 p-value=0.0005
Eyes Open	R=0.89832 p-value=7.588×10 ⁻⁸	R=0.6795 p-value=0.001	R=0.80971 p-value=1.522×10 ⁻⁵

5.4 Discussion

The parallel ICA method for combining fMRI and EEG has the ability to discover the connection between brain maps and EEG time courses. These results demonstrate that:

- (i) electrical correlates of DMN consist of both low and high frequency fluctuations,
- (ii) faster fMRI sampling is required to reveal DMN's high frequency electrical correlates,
- (iii) faster sampling also improves the correspondence between EEG and fMRI,
- (iv) the association of DMN with fast electrical dynamics proves that its neural origin is relevant to typically occurring fast mental processes and
- (iv) high frequency electrical correlates

of DMN may support the notion that resting state fluctuations reveal scale-free fractal properties. Below, we expand on these themes.

Over past several years, researchers have tried to show the link between the EEG frequency bands and the BOLD-fMRI RSNs and some have claimed that the EEG power envelope at specific frequency bands correlates with RSNs [24] [25] [26] [27] [28]. Others have argued and showed that EEG is made up of a wide frequency spectrum [29] [30], and thus the correlation between neuronal electrical activity only at specific frequencies to the BOLD RSNs cannot be true. This notion was supported by Mantini et al who demonstrated electrical correlates of different EEG spectral bands with the fMRI RSNs [32] thus proving that fMRI RSNs have unique correlation patterns across frequency bands. Since these studies have convolved power time courses and/or their envelopes of the bands of interest with a hemodynamic response function and subsequently downsampled it, they have ignored the high frequency dynamics of the signal. Therefore, they cannot really investigate whether high frequency electrical correlates of DMN exist or not. A recent study used empirical mode decomposition to show that resting state fMRI fluctuations are in fact broad band processes though their energy is concentrated in low frequencies [61]. Another recent study on fMRI RSNs investigated relatively higher frequency signal fluctuations (>0.25 Hz) using data acquired with a low TR of 354 ms using temporal ICA and showed that RSNs including DMN exist relatively higher frequencies than previously thought [62]. Unlike our study, these two recent studies did not look at electrical correlates of DMN, but they do suggest that even by just looking at fMRI data alone, one can come to the conclusion that fluctuations with a frequency higher than 0.1 Hz are not to be ignored. In our study, since

we did not downsample the EEG or consider its power envelope, our results with fMRI data acquired with faster sampling indicate that both low and high frequency electrical correlates exist for the DMN. In addition, the correlation between EEG and fMRI mixing matrices generally improved with faster sampling. These results demonstrate that faster sampling is required to find high frequency electrical correlates of DMN (and RSNs in general). Therefore, resting state fMRI studies must use as small TR as possible and should avoid low pass filtering.

Previous studies indicate that many sensory neuronal processes occur during 75-200 ms post stimulus [63] [64], while neuronal processes involving cognition happen during the 100-600 ms interval [65] [66]. This shows that neuronal dynamics occurs at a sub-second time scale. On the other hand, typical studies involving BOLD RSNs perform band pass filtering of fMRI time series in the frequency range of 0.01 Hz-0.1 Hz. This indicates that the period of the fastest variation in the signal is 10 s. This is at odds with the typical fast neuronal dynamics; however, given the sensitivity of BOLD RSNs, especially the DMN, to brain pathology [67] [68] [69] [70] [71] [72], there is reason to believe that the DMN has a neural basis. This apparent contradiction can be reconciled by our findings that with faster sampling and pICA, high frequency electrical correlates of DMN can be revealed in the beta (13-30) and gamma bands (30-60 Hz). Note that unlike previous studies [32] [33] [34] which showed that the downsampled versions of the power envelopes of these high frequency bands, which are in effect lower frequency fluctuations, correlated with fMRI time series fluctuations in the DMN, we have demonstrated, without any downsampling or using power envelopes, that the electrical

correlates of the DMN exist in high frequencies. This may also support the notion that fluctuations of brain activity at rest are scale-free as discussed below.

Studies have shown that EEG microstates are potential electrophysiological correlates of fMRI RSNs [33] [34]. Microstates are scalp topological configurations which remain quasi-stable for 80-100 ms. Previous studies [33] [34] showed that microstate time series (a quantized signal obtained by the dynamic state transitions between microstates) when convolved with a hemodynamic response function and downsampled to the fMRI resolution, correlated with BOLD time series derived from RSNs. While Britz et al [34] did not find a microstate time series corresponding to the DMN, Musso et al [33] and Yuan et al [73] did. Even though these studies used convolved and downsampled versions of microstate time series, they speculated that since microstates themselves represent fast neuronal dynamics, the RSNs such as the DMN may have electrical correlates in high frequencies. Consequently, they postulated that brain dynamics at rest may be scale-free such that their correlational structure will be visible at any time scale. Subsequently, it was shown that EEG microstates were indeed scale-free [74]. The above evidence, taken together with our results on both low and high frequency electrical correlates of DMN, support the notion that resting state BOLD fluctuations may have scale-free fractal properties

Some studies have already shown that the EO condition evoked higher functional connectivity of the default mode network (DMN) than the eyes-closed condition. The DMN is not only associated with day dreaming, mind wandering etc. but also associated with monitoring the functions of sensory input, and hence when the eyes are closed these activities seem to be less activated than when the eyes are open [2] [4] [75] [67] [76]

[77]. We found the correlation between the mixing coefficient of EEG and fMRI DMN to be higher in EPI and MB8 acquisition for EO Condition.

5.5 Conclusion

Using an integrated framework involving simultaneous EEG/fMRI acquisition, fast fMRI sampling (TR=600ms and TR=200ms) using multiband EPI, and EEG/fMRI fusion using parallel independent component analysis, we have tested the hypothesis that resting state fluctuations may exist not only in the low frequency, but also high frequency. This makes resting fluctuations obtained from fMRI more meaningful to typically occurring fast neuronal processes. The salient feature of our approach is that we did not down sample of EEG to fMRI temporal resolution, which allowed us to make inferences about fast electrical dynamics related to the default mode network.

5.6 Bibliography

- [1] B. Biswal, F. Yetkin, V. Haughton and J. Hyde, "Functional connectivity in the motor cortex of resting human brain using echo-planar MRI," *Magn. Reson. Med.*, vol. 34, p. 537–541, 1995.
- [2] M. Fox and M. Raichle, "Spontaneous fluctuations in brain activity observed with functional magnetic resonance imaging," *Nat. Rev. Neurosci.*, vol. 8, p. 700–711, 2007.
- [3] M. D. Greicius, B. Krasnow, A. L. Reiss and V. Menon, "Functional connectivity in the resting brain: A network analysis of the default mode hypothesis," *Proceedings of the National Academy of Sciences of the United States of America*, vol. 100, pp. 253-258, 2003.
- [4] D. Gusnard, M. Raichle and M. Raichle, "Searching for a baseline: Functional imaging and the resting human brain," *Nat Rev Neurosci*, vol. 2, p. 685–694, 2001.
- [5] C. Beckmann, M. DeLuca, J. Devlin and S. Smith, "Investigations into resting-state connectivity using independent component analysis," *Philos Trans R Soc Lond B Biol Sci*, vol. 360, pp. 1001-1013, 2005.

- [6] J. Damoiseaux, S. Rombouts, F. Barkhof, P. Scheltens and C. Stam, "Consistent resting-state networks across healthy subjects," *Proc Natl Acad Sci U S A*, vol. 103, pp. 13848-13853, 2006.
- [7] M. Van den Heuvel, R. Mandl and P. H. Hulshoff, "Normalized group clustering of resting-state fMRI data," *PLoS ONE*, vol. 3, no. 4, 2008.
- [8] M. Van den Heuvel, R. Mandl, J. Luigjes and P. H. Hulshoff, "Microstructural Organization of the Cingulum Tract and the level of Default Mode Functional Connectivity," *The Journal of Neuroscience*, vol. 28, no. 43, pp. 10844-10851, 2008.
- [9] D. Cordes, V. Haughton, K. Arfanakis, G. Wendt and P. Turski, "Mapping functionally related regions of brain with functional connectivity," *AJNR Am J Neuroradiol*, vol. 21, no. 9, pp. 1636-1644, 2000.
- [10] M. E. Raichle and M. A. Mintun, "BRAIN WORK AND BRAIN IMAGING," *Annual Review of Neuroscience*, vol. 29, pp. 449-476, 2006.
- [11] A. Fornito and E. Bullmore, "What can spontaneous fluctuations of the blood oxygenation-level-dependent signal tell us about psychiatric disorders?," *Curr. Opin. Psychiatry*, vol. 23, no. 3, pp. 239-249, 2010.
- [12] D. Auer , "Spontaneous low-frequency blood oxygenation level-dependent fluctuations and functional connectivity analysis of the 'resting' brain," *Magn Reson Imaging*, vol. 26, no. 7, 2008.
- [13] T. Lund, "fcMRI--mapping functional connectivity or correlating cardiac-induced noise?," *Magn Reson Med.*, vol. 46, no. 3, pp. 628-629, 2001.
- [14] J. Maldjian, "Functional connectivity MR imaging: fact or artifact?," *AJNR Am J Neuroradiol.*, vol. 22, no. 2, pp. 239-240, 2001.
- [15] N. Logothetis, "What we can do and what we cannot do with fMRI," *Nature*, vol. 453, no. 7197, pp. 869-878, 2008.
- [16] A. Arieli, A. Sterkin, A. Grinvald and A. Aertsen, "Dynamics of ongoing activity: explanation of the large variability in evoked cortical responses," *Science*, vol. 27, no. 273, p. 1868-1871, 1996.
- [17] M. Tsodyks, T. Kenet, A. Grinvald and A. Arieli, "Linking spontaneous activity of single cortical neurons and the underlying functional architecture," *Science*, vol. 3, no. 286, pp. 1943-1946, 1999.
- [18] A. Salek-Haddadi, K. Friston, L. Lemieux and D. Fish, "Studying spontaneous EEG activity with fMRI," *Brain Research*, vol. 43, no. 1, pp. 110-133, 2003.
- [19] H. Laufs, "Endogenous brain oscillations and related networks detected by surface," *Hum. Brain Mapp.*, vol. 29, no. 7, pp. 762-769, 2008.
- [20] S. Debener, M. Ullsperger, M. Siegel and A. Engel, "Single-trial EEGfMRI reveals the dynamics of cognitive function," *Trends Cogn. Sci.*, vol. 10, no. 12, pp. 558-563, 2006.
- [21] J. Hopfinger, W. Khoe and A. Song, "Combining electrophysiology with structural and functional neuroimaging: ERPs, PET, MRI, and fMRI," in *Event Related Potentials. A Methods Handbook*, Cambridge, The MIT Press, 2005, pp. 345-380.
- [22] B. Horwitz and D. Poeppel, "How can EEG/MEG and fMRI/PET data be combined ?," *Hum. Brain Mapp.*, vol. 17, no. 1, pp. 1-3, 2002.

- [23] S. Makeig, T. Jung and T. Sejnowski, "Having your voxels and timing them too?," in *Exploratory Analysis and Data Modeling in Functional Neuroimaging* edited by F. Sommer and A. Wichert, Cambridge, The MIT Press, 2002, pp. 195-207.
- [24] R. Goldman, J. Stern, J. Engel Jr. and M. Cohen, "Simultaneous EEG and fMRI of the alpha rhythm," *Neuroreport*, vol. 13, no. 18, p. 2487–2492, 2002.
- [25] H. Laufs, K. Krakow, P. Sterzer, E. Eger, A. Beyerle, A. Salek-Haddadi and A. Kleinschmidt, "Electroencephalographic signatures of attentional and cognitive default modes in spontaneous brain activity fluctuations at rest," *Proc. Natl. Acad. Sci.*, vol. 100, no. 19, p. 11053–11058, 2003.
- [26] M. Moosmann, P. Ritter, I. Krastel, A. Brink, S. Thees, F. Blankenburg, B. Taskin, H. Obrig and A. Villringer, "Correlates of alpha rhythm in functional magnetic resonance imaging and near infrared spectroscopy," *Neuroimage*, vol. 20, no. 1, pp. 145-158, 2003.
- [27] J. De Munck, S. Gonçalves, L. Huijboom, J. Kuijer, P. Pouwels, R. Heethaar and F. Lopes da Silva, "The hemodynamic response of the alpha rhythm: an EEG/fMRI study," *NeuroImage*, vol. 35, no. 3, pp. 1142-1151, 2007.
- [28] S. Sadaghiani, R. Scheeringa, K. Lehongre, B. Morillon, A. Giraud and A. Kleinschmidt, "Intrinsic connectivity networks, alpha oscillations, and tonic alertness: a simultaneous electroencephalography/functional magnetic resonance imaging study," *J. Neuroscience*, vol. 30, no. 30, p. 10243–10250, 2010.
- [29] G. Buzsaki and A. Draguhn, "Neuronal oscillations in cortical networks," *Science*, vol. 304, no. 5679, pp. 1926-1929, 2004.
- [30] F. Varela, J. Lachaux, E. Rodriguez and J. Martinerie, "The brainweb: phase synchronization and large-scale integration," *Nat. Rev. Neurosci*, vol. 2, no. 4, pp. 229-239, 2001.
- [31] H. Laufs, J. Holt, R. Elfont, M. Krams, J. Paul, K. Krakow and A. Kleinschmidt, "Where the BOLD signal goes when a EEG leaves," *Neuroimage*, vol. 31, no. 4, pp. 1408-1418, 2006.
- [32] D. Mantini, M. Perrucci, C. Del Gratta, G. Romani and M. Corbetta, "Electrophysiological signatures of resting state networks in the human brain," *Proc. Natl. Acad. Sci. U. S. A*, vol. 104, no. 32, p. 13170–13175, 2007.
- [33] J. Britz, D. Van De Ville and C. Michel, "BOLD correlates of EEG topography reveal rapid resting-state network dynamics," *Neuroimage*, vol. 52, no. 4, p. 1162–1170, 2010.
- [34] F. Musso, J. Brinkmeyer, A. Mobsacher, T. Warbrick and G. Winterer, "Spontaneous brain activity and EEG microstates. A novel EEG/fMRI analysis approach to explore resting-state networks," *Neuroimage2010*, vol. 52, no. 4, pp. 1149-1161, 2010.
- [35] J. Damoiseaux, C. Beckmann, E. Arigita, F. Barkhof, P. Scheltens, C. Stam, S. Smith and S. Rombouts, "Reduced resting-state brain activity in the ‘‘default network’’ in normal aging," *Cereb Cortex*, vol. 18, no. 8, pp. 1856-1864, 2008.
- [36] D. Feinberg, S. Moeller, S. Smith, E. Auerbach, S. Ramanna, M. Gunther, M. Glasser, K. Miller, K. Ugurbil and E. Yacoub, "Multiplexed echo planar imaging for

- sub-second whole brain fMRI and fast diffusion imaging," *PLoS One*, vol. 5, no. 12, 2010.
- [37] V. D. Calhoun, T. Adali, G. D. Pearlson and J. J. Pekar, "A method for making group inferences from functional MRI data using independent component analysis," *Hum. Brain Mapping*, vol. 14, no. 3, pp. 140-151, 2001.
 - [38] R. A. Thuraisingham, Y. Tran, P. Boord and A. Craig, "Analysis of eyes open, eye closed EEG signals using second-order difference plot," *Medical & Biological Engineering & Computing*, vol. 45, no. 12, pp. 1243-1249, 2007.
 - [39] R. J. Barry, A. R. Clarke, S. J. Johnstone and C. R. Brown, "EEG differences in children between eyes-closed and eyes-open resting conditions," *Clinical Neurophysiology*, vol. 120, no. 10, pp. 1806-1811, 2009.
 - [40] M. Fox, A. Snyder, J. Vincent, M. Corbetta, D. C. Van Essen and M. Raichle, "The human brain is intrinsically organized into dynamic, anticorrelated functional networks," *PNAS*, vol. 102, no. 27, pp. 9673-9678, 2005.
 - [41] P. Fransson, "Spontaneous low-frequency BOLD signal fluctuations: An fMRI investigation of the resting-state default mode of brain function hypothesis," *Human Brain Mapping*, vol. 26, no. 1, pp. 15-29, 2005.
 - [42] K. Kollndorfer, F. P. S. Fischmeister, G. Kasprian, D. Prayer and V. Schöpf, "A systematic investigation of the invariance of resting-state network patterns: is resting-state fMRI ready for pre-surgical planning?," *Frontiers in Human Neuroscience*, vol. 7, 2013.
 - [43] E. Marx, A. Deutschländer, T. Stephan, M. Dieterich, M. Wiesmann and T. Brandt, "Eyes open and eyes closed as rest conditions: impact on brain activation patterns," *Neuroimage*, vol. 21, no. 4, pp. 1818-1824, 2004.
 - [44] C. Yan, D. Liu, Y. He, Q. Zou, C. Zhu, X. Zuo, X. Long and Y. Zang, "Spontaneous Brain Activity in the Default Mode Network Is Sensitive to Different Resting-State Conditions with Limited Cognitive Load," *PLOS ONE*, vol. 4, no. 5, 2009.
 - [45] M. Bianciardi, M. Fukunaga, P. v. Gelderen, S. G. Horovitz, J. A. d. Zwart and J. H. Duyn, "Modulation of spontaneous fMRI activity in human visual cortex by behavioral state," *Neuroimage*, vol. 45, no. 1, pp. 160-168, 2009.
 - [46] L. Wu, T. Eichele and V. D. Calhoun, "Reactivity of hemodynamic responses and functional connectivity to different states of alpha synchrony: A concurrent EEG-fMRI study," *Neuroimage*, vol. 52, no. 4, pp. 1252-1260, 2010.
 - [47] K. Van Dijk, T. Hedden, A. Venkataraman, K. Evans, S. Lazar and R. Buckner, "Intrinsic functional connectivity as a tool for human connectomics: theory, properties, and optimization.,," *J Neurophysiol.*, vol. 103, no. 1, pp. 297-321, 2009.
 - [48] K. Friston, A. Holmes, K. Worsley, J. Poline, C. Frith and J. Frackowiak, "Statistical parametric maps in functional imaging: A general linear approach," *Human Brain Mapping*, vol. 2, no. 4, pp. 189-210, 1995.
 - [49] Y. Chao-Gan and Z. Yu-Feng, "DPARSF: A MATLAB Toolbox for "Pipeline" Data Analysis of Resting-State fMRI," *Front Syst Neurosci*, vol. 4, no. 13, 2010.
 - [50] X.-W. Song, Z.-Y. Dong, X.-Y. Long, S.-F. Li, X.-N. Zuo, C.-Z. Zhu, Y. He, C.-G. Yan and Y.-F. Zang, "REST: A Toolkit for Resting-State Functional Magnetic

- Resonance Imaging Data Processing," *PLoS ONE*, vol. 6, no. 9, 2011.
- [51] P. Allen, O. Josephs and R. Turner, "A method for removing imaging artifact from continuous EEG recorded during functional MRI," *Neuroimage*, vol. 12, no. 2, pp. 230-239, 2000.
 - [52] P. Allen, G. Polizzi, K. Krakow, D. Fish and L. Lemieux, "Identification of EEG events in the MR scanner: the problem of pulse artifact and a method for its subtraction," *NeuroImage*, vol. 8, pp. 229-239, 1998.
 - [53] A. Delorme and S. Makeig, "EEGLAB: an open source toolbox for analysis of single-trial EEG dynamics including independent component analysis," *J Neurosci Methods.*, vol. 134, no. 1, pp. 9-21, 2004.
 - [54] T. Lee, M. Girolami and T. Sejnowski, "Independent component analysis using an extended infomax algorithm for mixed subgaussian and supergaussian sources," *Neural Comput.*, vol. 11, no. 2, pp. 417-441, 1999.
 - [55] A. Bell and T. Sejnowski, "An information-maximization approach to blind separation and blind deconvolution," *Neural Comput.*, vol. 7, no. 6, pp. 1129-1159, 1995.
 - [56] V. Calhoun, T. Adali, G. Pearson and J. Pekar, "A method for making group inferences from functional MRI data using independent component analysis," *Hum Brain Mapp*, vol. 14, no. 3, pp. 140-151, 2001.
 - [57] V. Calhoun, K. Kiehl and G. Pearson, "Modulation of temporally coherent brain networks estimated using ICA at rest and during cognitive tasks," *Hum Brain Mapp*, vol. 29, no. 7, pp. 828-838, 2008.
 - [58] C. Rosazza, L. Minati, F. Ghielmetti, M. Mandelli and M. Bruzzone, "Functional Connectivity during Resting-State Functional MR Imaging: Study of the Correspondence between Independent Component Analysis and Region-of-Interest-Based Methods," *AJNR Am J Neuroradiol.*, vol. 33, no. 1, pp. 180-187, 2012.
 - [59] T. Eichele, S. Rachakonda, B. Brakedal, R. Eikeland and V. Calhoun, "EEGIFT: group independent component analysis for event-related EEG data," *Comput. Intell. Neurosci.*, vol. 2011, 2011.
 - [60] V. D. Calhoun, "Fusion ICA Toolbox (FIT)," [Online]. Available: <http://mialab.mrn.org/software/fit/>.
 - [61] R. Niazy, J. Xie, K. Miller, C. Beckmann and S. Smith, "Spectral characteristics of resting state networks," *Prog Brain Res.*, vol. 193, pp. 259-276, 2011.
 - [62] R. Boubela, K. Kalcher, W. Huf, C. Kronnerwetter, P. Filzmoser and E. Moser, "Beyond Noise: Using Temporal ICA to Extract Meaningful Information from High-Frequency fMRI Signal Fluctuations during Rest," *Front Hum Neurosci.*, vol. 7, no. 168, 2013.
 - [63] F. Di Russo, A. Martínez, M. Sereno, S. Pitzalis and S. Hillyard, "Cortical sources of the early components of the visual evoked potential," *Hum Brain Mapp.*, vol. 15, no. 2, pp. 95-111, 2002.
 - [64] B. Sadeh, A. Zhdanov, I. Podlipsky, T. Hendler and G. Yovel, "The validity of the face-selective ERP N170 component during simultaneous recording with functional

- MRI," *Neuroimage*, vol. 42, no. 2, pp. 778-786, 2008.
- [65] M. Kutas, G. McCarthy and E. Donchin, "Augmenting mental chronometry: the P300 as a measure of stimulus evaluation time," *Science*, vol. 197, no. 4305, pp. 792-795, 1977.
- [66] A. Gouvea, C. Phillips, N. Kazanina and D. Poeppel, "The linguistic processes underlying the P600," *Language and Cognitive Processes*, vol. 25, no. 2, pp. 140-188, 2010.
- [67] R. Buckner, J. Andrews-Hanna and D. Schacter, "The brain's default network: Anatomy, function, and relevance to disease," *Ann N Y Acad Sci*, vol. 1124, pp. 1-38, 2008.
- [68] Y. Zhou, M. Milham, Y. Lui, L. Miles, J. Reaume, D. Sodickson, R. Grossman and Y. Ge, "Default-mode network disruption in mild traumatic brain injury," *Radiology*, vol. 265, no. 3, pp. 882-892, 2012.
- [69] G. Mingoia, W. G, L. K, R. Maitra, S. Smesny, M. Dietzek, H. Burmeister, J. Reichenbach, R. Schlösser, C. Gaser, H. Sauer and I. Nenadic, "Default mode network activity in schizophrenia studied at resting state using probabilistic ICA," *Schizophr Res.*, vol. 138, no. 2-3, pp. 143-149, 2012.
- [70] V. Bonnelle, R. Leech, K. Kinnunen, T. Ham, C. Beckmann, X. De Boissezon, R. Greenwood and D. Sharp, "Default mode network connectivity predicts sustained attention deficits after traumatic brain injury," *J Neurosci.*, vol. 31, no. 38, pp. 13442-13451, 2011.
- [71] K. Mevel, B. Grassiot, G. Chételat, G. Defer, B. Desgranges and F. Eustache, "The default mode network: cognitive role and pathological disturbances," *Rev Neurol (Paris)*, vol. 166, no. 11, pp. 859-872, 2010.
- [72] J. Shin, V. Kepe, G. Small, M. Phelps and J. Barrio, "Multimodal Imaging of Alzheimer Pathophysiology in the Brain's Default Mode Network," *Int J Alzheimers Dis.*, vol. 2011, no. 2011, 2011.
- [73] H. Yuan, V. Zotev, R. Phillips, W. Drevets and J. Bodurka, "Spatiotemporal dynamics of the brain at rest--exploring EEG microstates as electrophysiological signatures of BOLD resting state networks," *Neuroimage*, vol. 60, no. 4, pp. 2062-2072, 2012.
- [74] D. Van de Ville, J. Britz and C. Michel, "EEG microstate sequences in healthy humans at rest reveal scale-free dynamics," *Proc Natl Acad Sci U S A.*, vol. 107, no. 42, pp. 18179-18184, 2010.
- [75] M. Mason, M. Norton, J. Van Horn, D. Wegner, S. Grafton and C. Macrae, "Wandering minds: The default network and stimulus-independent thought," *Science*, pp. 393-395, 2007.
- [76] S. J. Gilbert, I. Dumontheil, J. S. Simons, C. D. Frith and P. W. Burgess, "Comment on "Wandering minds: the default network and stimulus-independent thought"," *Science*, vol. 317, no. 43, 2007.
- [77] B. Hahn, T. J. Ross and E. A. Stein, "Cingulate activation increases dynamically with response speed under stimulus unpredictability," *Cerebral cortex*, vol. 17, no. 7, pp. 1664-1671, 2007.

